

Copyright  
by  
Elizabeth Wingfield Oldag  
2013

The Dissertation Committee for Elizabeth Wingfield Oldag  
certifies that this is the approved version of the following dissertation:

**Two-Particle Correlations in Angular and Momentum  
Space in Heavy Ion Collisions at STAR**

Committee:

---

Gerald Hoffmann, Supervisor

---

Robert Ray

---

Christina Markert

---

Karol Lang

---

Philip Cannata

**Two-Particle Correlations in Angular and Momentum  
Space in Heavy Ion Collisions at STAR**

by

**Elizabeth Wingfield Oldag, B.S.**

**DISSERTATION**

Presented to the Faculty of the Graduate School of

The University of Texas at Austin

in Partial Fulfillment

of the Requirements

for the Degree of

**DOCTOR OF PHILOSOPHY**

The University of Texas at Austin

May 2013

To my parents, my mentors, and my husband

## Acknowledgments

I would like to take this opportunity to express my appreciation for all those who have supported, encouraged, and inspired me. I am especially thankful to my husband, Drew. Thank you so much for supporting me every step of the way. I am unable to put into words how happy I am to be sharing my life with you.

I am also grateful to have parents who encouraged me to pursue my goals and, through example, showed me that anything is possible with enough will and determination. This work is due in part to the support from: my father and stepmother, Bill and Vickie; my mother and stepfather, Kris and Joel; and my sister Amy. I also want to thank my husband's family for being steadfast cheerleaders of mine.

My growth as a scientist is due to the wonderful mentoring and guidance I received from Lanny Ray. Thank you for sharing your passion for science with me (the good and the bad) and leading an analysis program of which I am honored to be apart. I also thank Jerry Hoffmann for welcoming me into the group and being an enthusiastic supervisor. I am lucky to have worked with great colleagues such as Christina Markert, Jo Schambach, Alan Davila, Masa Wada and Prabhat Bhattarai. I also thank Alex Jentsch and Martin Codrington for proofreading this dissertation.

The support I received outside of UT Austin also deserves recognition. I thank the STAR collaboration and Brookhaven National Lab for making the experiment and therefore this analysis possible. I also thank Tom Trainor, Duncan Prindle, and Gene Van Buren for their mentorship and support.

Elizabeth Oldag

# **Two-Particle Correlations in Angular and Momentum Space in Heavy Ion Collisions at STAR**

Elizabeth Wingfield Oldag, Ph.D.  
The University of Texas at Austin, 2013

Supervisor: Gerald Hoffmann

For over a decade studies of the strong interaction in extremely dense nuclear environments have been done at the Relativistic Heavy Ion Collider (RHIC) at Brookhaven National Laboratory. It is hypothesized that colliding two beams of Au nuclei at relativistic speeds creates an environment of hot dense nuclear matter where the quarks and gluons inside the nucleus, which are normally confined within the protons and neutrons, become deconfined into a soup called the quark-gluon plasma. Since direct observation of this short-lived phase is impossible, many sophisticated analysis techniques attempt to study the early interactions via the final state particles. What has emerged from analyses of the data are two, contradictory paradigms for understanding the results. On the one hand the colliding quarks and gluons are thought to strongly interact and reach thermal equilibrium. The other view is that primary parton-parton scattering leads directly to jet fragmentation with little effect from re-scattering. It is in principle possible to distinguish and perhaps

falsify one or both of these models of relativistic heavy ion collisions via the analysis of two-particle correlations among all charged particles produced in  $\sqrt{s_{NN}} = 200$  GeV Au+Au collisions at the STAR experiment at RHIC. This dissertation presents studies of two-particle correlations, whose derivation can be traced back to Pearsons correlation coefficient, in transverse momentum and angular space. In momentum space a broad peak is observed extending from 0.5-4.0 GeV/ $c$  which, as a function of nuclear overlap, remains at a fixed position while monotonically increasing in amplitude. Comparisons to theoretical models suggests this peak is from jet fragmentation. In a complementary study the momentum distribution of correlations in  $(\eta, \phi)$  space is investigated. The momentum distribution of correlated pairs that contribute to the peak near the origin, commonly associated with jet fragmentation, is peaked around 1.5 GeV/ $c$  and does not soften with increased centrality. These measurements present important aspects of the available six dimensional correlation space and provide definitive tests for theoretical models. Preliminary findings do not appear to support the hypothesis of a strongly interacting QGP where back-to-back jets are expected to be significantly suppressed.



# Table of Contents

<b>Acknowledgments</b>	<b>v</b>
<b>Abstract</b>	<b>vii</b>
<b>Contents</b>	<b>ix</b>
<b>List of Tables</b>	<b>xii</b>
<b>List of Figures</b>	<b>xiii</b>
<b>Chapter 1. Introduction</b>	<b>1</b>
1.1 The Strong Force and QCD . . . . .	1
1.2 Analysis Technique . . . . .	4
1.3 Outline . . . . .	7
<b>Chapter 2. Experiment Details</b>	<b>8</b>
2.1 Brookhaven . . . . .	8
2.2 RHIC . . . . .	9
2.3 RHIC Detectors . . . . .	12
2.4 STAR . . . . .	14
2.4.1 TPC . . . . .	14
2.4.2 Other Detector Subsystems . . . . .	18
<b>Chapter 3. Analysis Details</b>	<b>21</b>
3.1 Variables . . . . .	21
3.2 Event Selection . . . . .	24
3.2.1 Trigger . . . . .	24
3.2.2 Vertex Cut . . . . .	28
3.2.3 Pileup . . . . .	28

3.2.4	Centrality . . . . .	34
3.3	Track Selection . . . . .	37
3.3.1	Pair Cuts . . . . .	41
3.4	Two-particle correlation measure . . . . .	42
3.4.0.1	Difference Variables . . . . .	46
3.4.1	Event Classes . . . . .	47
3.4.2	Reference Choice . . . . .	50
3.4.3	Normalization . . . . .	56
3.4.3.1	Pair . . . . .	56
3.4.3.2	Event . . . . .	57
3.4.3.3	Event with Bias Correction . . . . .	58
<b>Chapter 4.</b>	<b>Review of Correlations</b>	<b>60</b>
4.1	Fluctuations . . . . .	61
4.2	Proton-proton Correlations . . . . .	64
4.2.1	Proton-proton Fit Model . . . . .	68
4.3	Jets . . . . .	69
4.3.1	Minijets . . . . .	74
4.4	Heavy Ion Correlations . . . . .	74
4.4.1	Quadrupole . . . . .	77
4.4.2	The $\eta_\Delta$ Elongated 2D Gaussian . . . . .	80
4.4.2.1	Sextupole . . . . .	82
<b>Chapter 5.</b>	<b>Transverse momentum correlations</b>	<b>83</b>
5.1	Charge Independent Results . . . . .	83
5.2	Charge and Angle Differentiations . . . . .	86
5.3	Fitting . . . . .	89
5.3.1	Inclusive Fit Models . . . . .	90
5.3.2	Cut Window Method . . . . .	92
5.3.3	2D Levy Model . . . . .	95
5.4	Model Comparisons . . . . .	100
5.4.1	HIJING . . . . .	101
5.4.2	AMPT . . . . .	103

5.4.3	NexSpheRIO . . . . .	106
5.5	Errors and Reference Distributions Choices . . . . .	108
5.5.1	Systematic Errors . . . . .	109
5.5.2	Reference Distribution . . . . .	113
5.5.3	Electron Contamination Simulation . . . . .	115
5.6	Discussion . . . . .	119
<b>Chapter 6.</b>	<b>The Momentum Dependence of Angular Correlations</b>	<b>122</b>
6.1	Analysis Setup . . . . .	122
6.2	Weighting . . . . .	123
6.3	Fitting Procedure . . . . .	126
6.3.1	2D Exponential . . . . .	128
6.3.2	Quadrupole . . . . .	129
6.3.3	Negative Like-sign Dip . . . . .	130
6.3.4	Same-side Peak Gaussian(s) . . . . .	132
6.3.5	Higher Order Fourier Components . . . . .	132
6.4	Results . . . . .	133
6.4.1	Dipole . . . . .	134
6.4.2	Quadrupole . . . . .	135
6.4.3	1D Gaussian . . . . .	136
6.4.4	2D Exponential . . . . .	137
6.4.5	2D Gaussian(s) . . . . .	137
6.5	Discussion . . . . .	142
6.5.1	Comparison to a Similar Analysis . . . . .	144
6.5.2	Future Work . . . . .	148
<b>Chapter 7.</b>	<b>Conclusion</b>	<b>149</b>
	<b>Bibliography</b>	<b>154</b>
	<b>Vita</b>	<b>160</b>

# List of Tables

3.1	Centrality definitions as a function of $N_{ch}$ for 2004 200 GeV Au+Au collisions with $p_t > 0.15$ GeV/ $c$ , $ \eta  < 1$ , and $\phi < 2\pi$ . The centrality measure $\nu$ is defined in Sec. 3.4.2 . . . . .	38
-----	--------------------------------------------------------------------------------------------------------------------------------------------------------------------------------------------------------------------	----

# List of Figures

1.1	A diagram containing the properties of particles in the standard model (Figure Credit: Wikipedia “Standard Model”) . . . . .	2
2.1	Diagram of the accelerator facilities at Brookhaven National Laboratory which provide Au+Au collisions . . . . .	10
2.2	Heavy-ion collisions at RHIC recorded by STAR and the integrated luminosity (blue line) [1]. . . . .	13
2.3	A cutaway view of the STAR detector to view inner detectors active in 2004 [2]. . . . .	15
2.4	A diagram of the STAR TPC detector. . . . .	16
2.5	Ionization energy loss (dE/dx) as a function of transverse momentum ( $p_t$ ) for 200 GeV Au+Au collisions. Figure provided by Masayuki Wada. . . . .	18
2.6	A scatter plot of track information, $1/\beta$ vs momentum (p) for 200 GeV Au+Au collisions. Figure provided by Masayuki Wada	20
3.1	Coordinate system drawn over an outline of the TPC volume .	22
3.2	Fast trigger detectors in STAR. . . . .	25
3.3	The distribution of events with respect to summed signal amplitudes from the CTB and ZDC [3]. . . . .	27
3.4	Cartoon of pre-pileup in two frames of observation. The event is triggered from the pileup collision (left panel). The collision occurs some time before the triggered event (right panel). The tracks from particles that cross the central membrane are split in the right panel into two different colors (blue and yellow) that correspond to one track in the left panel. . . . .	31
3.5	Histograms of the first and last position of global tracks in an event that contains pre-pileup [4]. . . . .	32
3.6	Cartoon of a collision in three scenarios. The event is triggered from the collision (top left). The collision occurs some time after a triggered event (top right). The reconstructed positions of tracks (bottom). . . . .	33

3.7	Histograms of the first and last position of global tracks in an event that contains pileup tracks from after the triggered collision [4] . . . . .	34
3.8	Plots of the multiplicity distribution of events from Au+Au 200 GeV 2004 collisions on various scales. . . . .	36
3.9	Distribution of tracks as a function of $p_t$ (left) and $dE/dx$ versus momentum (right) of 2004 200 GeV Au+Au collisions. . . . .	40
3.10	Distributions of particles in a 1D (left) and 2D (middle) space with bins a and b explicitly marked. The right panel labels the sum ( $\Sigma$ ) and difference ( $\Delta$ ) axes [5]. . . . .	43
3.11	Two-particles correlations from 130 GeV central Au+Au collisions on $(\eta_1, \eta_2)$ (upper) and $(\phi_1, \phi_2)$ (bottom) and for like-sign (left) and unlike-sign (right) pairs [6]. . . . .	47
3.12	Projecting data onto the $\eta_\Delta$ axis is equivalent to a rotation of the coordinate system by $45^\circ$ (left panel). The new 1D distribution (right panel) is triangular due to the finite $\eta$ acceptance. . . .	48
3.13	The differential multiplicity divided by $\langle N_{part} \rangle / 2$ versus $\nu$ for identified pions, kaons, and total hadrons (left panel) and protons (right panel) for 200 GeV p+p collisions and 5 Au+Au centralities. The data are represented by solid points and lines. The dotted line labeled “ $S_{NN}$ ” indicates the soft component. The dashed-dotted line labeled “ $\nu H_{NN}$ ” extrapolates the N-N collision value with binary scaling (no enhancement in heavy ion collisions). The soft component and the hard component ( $\nu H_{AA}$ ) sum to the data [7]. . . . .	53
4.1	The hypothesized Quark Gluon Plasma phase diagram from QCD predictions [8]. The white solid lines show the phase boundaries and the white circle indicates the critical points. The nuclear overlap of current Au+Au collisions are marked with an orange star. . . . .	62
4.2	The mean- $p_t$ non-statistical fluctuation measure $\Delta\sigma_{p_t}^2$ (left) and two-particle correlations (right) of 0-15% central HIJING events with quenching off [9]. . . . .	64
4.3	200 GeV Proton-proton collisions at STAR in momentum [10] and angular [3] space. . . . .	65
4.4	The left two panels contain soft pairs defined as $(y_t < 2)$ ( $p_t = 0.5$ GeV/ $c$ ) for both particles in a pair. The right two panels contain hard pairs ( $y_t > 2$ ). The first and third panels are for like-sign pairs and the second and fourth panels are for unlike-sign pairs [10].	66

4.5	Feynman diagrams of two-body processes. The u, t, and s-channel correspond to the Mandelstam variables which describe the four-momentum of the exchanged particle. . . . .	71
4.6	Two-particle angular correlations for Au+Au collisions at $\sqrt{s_{NN}}=200$ and 62 GeV (upper and lower rows respectively). Centrality increases left-to-right from most-peripheral to most-central [11].	75
4.7	Fit parameters versus centrality reported in [11] for Au+Au collisions at $\sqrt{s_{NN}}=200$ GeV (solid symbols) and 62 GeV (open symbols). The 2D Gaussian amplitude and widths are shown in the upper panels. The amplitude of the dipole and quadrupole and shown in the bottom left and middle panel respectively. The bottom right panel shows the width aspect ratio, $\sigma_{\eta\Delta}/\sigma_{\phi\Delta}$ , of the 2D Gaussian. The error bars represent fitting errors. The dotted line labeled “GLS” indicates the prediction from Glauber linear superposition. The hatched regions indicate the systematic uncertainties. . . . .	77
4.8	The fit decomposition of 46-55% centrality data for 62 GeV Au+Au collisions [11]. The data, fit, and residual are shown in the upper left plots. The upper right plot shows the 2D Gaussian component. The lower panels show the dipole, quadrupole, 1D Gaussian, and the 2D exponential. . . . .	78
4.9	The first three panels show $v_2$ and jet measurements as a function of $p_t$ in centralities 30-40%, 5-10%, and 0-5% for Au+Au 200 GeV data [12]. The right panel shows the quadrupole spectrum as a function of $y_t$ with a fit $Q_o(y_t)$ . . . . .	80
5.1	2D CI correlations $\Delta\rho/\sqrt{\rho_{soft}}(y_{t1}, y_{t2})$ for Au+Au collisions at $\sqrt{s_{NN}}=200$ GeV. Centrality increases from left-to-right and top-to-bottom. . . . .	84
5.2	CI $(y_{t1}, y_{t2})$ correlations for 200 GeV Au+Au collisions in four combinations of reference distributions and normalization procedures, all with a common z-axis scale. Centrality increases from left-to-right. The three upper rows use $\rho_{mix}$ while the bottom row uses $\rho_{soft}$ . The normalization from top to bottom is “pair”, “event” and “event” with a finite bin width correction factor (last two rows). . . . .	85
5.3	Two-dimensional $(y_{t1}, y_{t2})$ correlations for Au+Au collisions at $\sqrt{s_{NN}} = 200$ GeV. Centrality increases from left-to-right. The two upper rows show away-side pairs and the two lower rows show same-side pairs. The first and third rows are like-sign pairs and the second and fourth row are unlike-sign pairs. . .	87

5.4	The dotted curves are the soft components for protons and pions. The dash-dot curves are the hard components for $\nu = 1$ and the solid curves are the hard components for $\nu = 6$ [7]. . .	89
5.5	Two-dimensional $(y_{t1}, y_{t2})$ same-side charge dependent correlations for Au+Au collisions at $\sqrt{s_{NN}} = 200$ GeV. Centrality increases from left-to-right and top-to-bottom. . . . .	90
5.6	The upper panels show the inclusive model fits and the lower panels show residuals for Au+Au CI $\Delta\rho/\sqrt{\rho_{soft}}$ data in three centralities. The centralities from left-to-right are 64-74%, 28-38%, and 0-5%. . . . .	92
5.7	Au+Au US AS $\Delta\rho/\sqrt{\rho_{soft}}$ data (upper), cut window model fits (middle), and residuals (lower). The centralities from left-to-right are 74-84%, 38-46%, and 0-5%. The cut window is approximately $ y_{t\Delta}  < 2.0$ and $4 < y_{t\Sigma} < 8$ . . . . .	93
5.8	Au+Au LS AS $\Delta\rho/\sqrt{\rho_{soft}}$ data (upper), cut window model fits (middle), and residuals (lower). The centralities from left-to-right are 74-84%, 38-46%, and 0-5%. The cut window is approximately $ y_{t\Delta}  < 2.0$ and $4 < y_{t\Sigma} < 8$ . . . . .	94
5.9	Au+Au US SS $\Delta\rho/\sqrt{\rho_{soft}}$ data (upper), cut window model fits (middle), and residuals (lower) . The centralities from left-to-right are 74-84%, 38-46%, and 0-5%. The cut window is approximately $ y_{t\Delta}  < 2.0$ and $y_{t\Sigma} < 8$ . . . . .	95
5.10	Au+Au LS SS $\Delta\rho/\sqrt{\rho_{soft}}$ data (upper), model fits (middle), and residuals (lower). The centralities from left-to-right are 74-84%, 38-46%, and 0-5%. The cut window is approximately $ y_{t\Delta}  < 2.0$ and $5.5 < y_{t\Sigma} < 8$ . . . . .	96
5.11	Fit parameters for $(y_t, y_t)$ correlation data versus centrality measure $\nu$ . The parameters in the upper row are the 2D Gaussian amplitude (left) and the $y_{t\Sigma}$ width (right). The lower row contains the $y_{t\Delta}$ width (left) and the center location along the diagonal ( $y_{t1} = y_{t2}$ ) (right). The error bars represent fitting errors derived from the statistical error of the data. . . . .	97
5.12	Data (left), Levy fit model (middle) and residual (right) for CI 200 GeV 28-38% central Au+Au collisions. . . . .	99
5.13	Data (left), 2D Levy fit plus Gaussian model (middle) and residual (right) for AS CI 200 GeV 28-38% central Au+Au collisions. . . . .	100



5.14	Fit parameters for AS CI $(y_{t1}, y_{t2})$ data versus centrality measure $\nu$ . The parameters in the upper panels corresponds to the 2D Levy component. The parameters in the lower panels correspond to the 2D Gaussian. The two most peripheral centralities had a reduced $(y_{t1}, y_{t2})$ range ( $y_{t\Sigma} < 4.0$ ). The error bars represent fitting errors derived from the statistical error of the data. . . . .	101
5.15	Two-particle correlations from HIJING for 75-85% central events. The first and third panel show results with jets on; the second and fourth are with jets off. . . . .	102
5.16	Two-parton correlations from AMPT for collisions in the 45-55% centrality bin. The upper row contain angular space correlations and the bottom row contain momentum space correlations. The partonic cross section values are (left to right) 0 mb, 1.5 mb, 3 mb, and 6 mb. . . . .	105
5.17	Correlations from NexSpheRIO events in angular (upper) and momentum (lower) space for Au+Au 200 GeV collisions in four centralities. The centralities, from left-to-right, are 60-80%, 40-60%, 20-30%, and 0-10%. . . . .	108
5.18	The statistical error on the final $\Delta\rho/\sqrt{\rho_{soft}}(y_{t1}, y_{t2})$ data for 38-46% central collisions. The z-axis scale on the left panel is equal to the data. The z-axis scale on the right panel is zoomed in for better visual access. . . . .	109
5.19	A distribution of $\rho_{soft}$ on $y_t$ for five different configurations on a linear (left) and log (right) scale. . . . .	115
5.20	The simulated momentum distribution of electrons from photon conversion. . . . .	116
5.21	$\Delta\rho/\sqrt{\rho_{soft}}$ for correlated electron pairs in the 18-28% centrality bin. . . . .	119
6.1	The locations of the 28 unique cut bins in $(y_{t1}, y_{t2})$ space for the present study. Both permutations of a pair were taken but only one half of the $(y_{t1}, y_{t2})$ space was filled due to an inherent symmetry. . . . .	123
6.2	Scatter plot of 500 Simplex fit results for centrality 5-9% in the range $y_{t1} = [3, 3.5]$ and $y_{t2} = [2, 2.5]$ (cut bin 15). Each fit was started at a random location in the 11-dimensional parameter space. Left Panel: $\chi^2$ versus 2D Gaussian amplitude. Right Panel: $\chi^2$ versus 2D exponential amplitude. . . . .	128
6.3	Scatter plot of the $\chi^2$ versus quadrupole amplitude for 10,000 Simplex fits with random starting locations for 10-18% central events in the range $y_{t1} = y_{t2} = [1.5, 2]$ (cut bin 7). . . . .	130

6.4	Charge independent (left) and like-sign (right) angular correlations in the range $y_{t1} = [2, 2.5]$ and $y_{t2} = [1, 1.5]$ (cut bin 2) and centrality fraction 9-18% . . . . .	131
6.5	CI angular correlations in the range $y_{t1} = y_{t2} = [3.5, 4.0]$ (cut bin 25) and centrality fraction 9-18%. . . . .	132
6.6	The amplitude of the dipole component on $(y_{t1}, y_{t2})$ in 11 centralities for Au+Au 200 GeV collisions. . . . .	135
6.7	The amplitude of the quadrupole component on $(y_{t1}, y_{t2})$ in 11 centralities for Au+Au 200 GeV collisions. . . . .	136
6.8	The volume of the 1D Gaussian on $\eta_\Delta$ on $(y_{t1}, y_{t2})$ in 4 centralities, increasing left-to-right, for Au+Au 200 GeV collisions. . . . .	137
6.9	The volume of the 2D exponential on $(y_{t1}, y_{t2})$ in 11 centralities for Au+Au 200 GeV collisions. . . . .	138
6.10	The volume of the 2D Gaussian(s) on $(y_{t1}, y_{t2})$ in 11 centralities for Au+Au 200 GeV collisions. . . . .	139
6.11	Upper panels: Projections of the momentum distribution of the 2D Gaussian(s) on the $y_{t\Sigma}$ axis for five centralities with a 1D fit in blue. Lower panels: The 1D Gaussian amplitude (left), width (center) and position (right) of the fit to the projections as a function of $\nu$ for 11 centralities. . . . .	140
6.12	Upper panels: Projections of the momentum distribution of the 2D Gaussian(s) on the $y_{t\Delta}$ axis for five centralities. Lower panels: The 1D Gaussian amplitude (left), width (center), and position (right) of the fit to the projections as a function of $\nu$ for 11 centralities. . . . .	141
6.13	The volume of the 2D Gaussian(s) on $(y_{t1}, y_{t2})$ in three $\eta_\Delta$ regions (rows) in five centralities (columns). The $\eta_\Delta$ regions from top to bottom are $ \eta_\Delta  < 2/3$ , $2/3 <  \eta_\Delta  < 4/3$ and $4/3 <  \eta_\Delta  < 2$ . . . . .	142
6.14	The analysis in Ref. [13] forms a marginal distribution equivalent to symmetric stripes in the present 2D $(y_{t1}, y_{t2})$ analysis. . . . .	145
6.15	The amplitude of the same-side Gaussian (right) and quadrupole (left) from Ref. [13] (upper) and the present analysis (lower) in six centralities of Au+Au 200 GeV data. The points in the upper (lower) panels represent the mean $y_t$ in each of the 9 (7) $y_t$ bins. Error bars in the upper panels are fit errors only. . . . .	147

# Chapter 1

## Introduction

Colliding two heavy ions at relativistic speeds is interesting to physicists because of the possibility of creating a unique phase of matter called the Quark Gluon Plasma (QGP). In a QGP the quarks and gluons, which are normally confined within the protons and neutrons by the strong force, are free to move over distances larger than the size of a hadron. Furthermore, a QGP created in the lab might be similar to the universe a few microseconds after the Big Bang or present day systems in the center of neutron stars.

### 1.1 The Strong Force and QCD

The strong force is one of four elementary forces of nature and it is responsible for binding quarks and gluons together to form particles such as the proton and neutron. Gluons, the carriers of the strong force, act on objects that carry a quantum number called color charge. Gluons are unique in the fact that they also carry a color charge unlike the analogous mediator for the electromagnetic force; the photon, which carries no electric charge. This adds many complications to Quantum Chromodynamics (QCD), the theory which describes strong interactions.

Three generations of matter (fermions)				
	I	II	III	
mass →	2.4 MeV/c <sup>2</sup>	1.27 GeV/c <sup>2</sup>	171.2 GeV/c <sup>2</sup>	0
charge →	$\frac{2}{3}$	$\frac{2}{3}$	$\frac{2}{3}$	0
spin →	$\frac{1}{2}$	$\frac{1}{2}$	$\frac{1}{2}$	1
name →	<b>u</b> up	<b>c</b> charm	<b>t</b> top	<b>γ</b> photon
Quarks	4.8 MeV/c <sup>2</sup>	104 MeV/c <sup>2</sup>	4.2 GeV/c <sup>2</sup>	0
	$-\frac{1}{3}$	$-\frac{1}{3}$	$-\frac{1}{3}$	0
	$\frac{1}{2}$	$\frac{1}{2}$	$\frac{1}{2}$	1
	<b>d</b> down	<b>s</b> strange	<b>b</b> bottom	<b>g</b> gluon
Leptons	<2.2 eV/c <sup>2</sup>	<0.17 MeV/c <sup>2</sup>	<15.5 MeV/c <sup>2</sup>	91.2 GeV/c <sup>2</sup>
	0	0	0	0
	$\frac{1}{2}$	$\frac{1}{2}$	$\frac{1}{2}$	1
	<b>ν<sub>e</sub></b> electron neutrino	<b>ν<sub>μ</sub></b> muon neutrino	<b>ν<sub>τ</sub></b> tau neutrino	<b>Z<sup>0</sup></b> Z boson
Leptons	0.511 MeV/c <sup>2</sup>	105.7 MeV/c <sup>2</sup>	1.777 GeV/c <sup>2</sup>	80.4 GeV/c <sup>2</sup>
	-1	-1	-1	±1
	$\frac{1}{2}$	$\frac{1}{2}$	$\frac{1}{2}$	1
	<b>e</b> electron	<b>μ</b> muon	<b>τ</b> tau	<b>W<sup>±</sup></b> W boson
				Gauge bosons

Figure 1.1: A diagram containing the properties of particles in the standard model (Figure Credit: Wikipedia “Standard Model”)

Of the fundamental particles which comprise the standard model, quarks and gluons are the only ones which carry color charge. The standard model was a significant development in the late 20th century and provides a complete description of all the fundamental particles as seen in Fig. 1.1.

The color charge states are referred to as either “red”, “blue”, “green” or the corresponding “anti-color”. A stable particle is color neutral meaning it contains either two valence quarks that are of a “color” and “anti-color” or three valence quarks which contain each of the three colors (analogous to “white”).

An important feature of the strong force is confinement. Confinement describes the increasing force of the strong interaction with increasing distance, contrary to the relationship in the electromagnetic force. Therefore, when a colored object is pulled from a color neutral particle the force increases between that object and the other colored objects until it becomes energetically favorable to produce a new quark-antiquark pair. The new quark or antiquark recombines with the escaping object to form another color neutral particle. Due to this process it is impossible to observe a single quark.

The strong force does not act over large distances because colored objects only exist within the boundaries of a color neutral particle. However, a small amount of strong force does act amongst color neutral objects, called the residual strong force, and is responsible for holding the protons and neutrons together in a nucleus.

Another important characteristic of the strong force was discovered in the early 1970s by physicists David Politzer, Frank Wilczek, and David Gross [14, 15]. They hypothesized that as the distance between the interacting quarks and gluons decreases the strong force will become asymptotically weaker and approach zero. This property is called asymptotic freedom and Politzer, Wilczek, and Gross received a Nobel Prize for this work in 2004.

The Relativistic Heavy Ion Collider was built to test the hypothesis that high energy densities and high temperatures would be produced in heavy ion collisions which, due to asymptotic freedom, may create a deconfined soup of quarks and gluons called a quark gluon plasma. This dissertation contains

analyses of Au+Au collision data with a center of mass energy of 200 GeV detected by the Solenoidal Tracker at RHIC (STAR) experiment.

## 1.2 Analysis Technique

Most consider the primary physics objective of RHIC is the search for signatures of a QGP in heavy ion collision data. This is an especially challenging task since direct observation of this short-lived phase is impossible. Sophisticated analysis techniques are required to study the early interactions via the final state particles.

The analysis method used in this dissertation is a two-particle correlation measure, whose derivation can be traced back to Pearson's correlation coefficient. This measure is formed from all pairs of particles in a collision averaged over millions of collisions and enhances otherwise small signals in the data. These signals are from physical processes that create a particular distribution in momentum and/or angular space.

Heavy ion collisions are classified by the amount of nuclear overlap of the colliding nucleons. There is likely no QGP formed in collisions with a small nuclear overlap due to the small amount of interacting nuclear material. These “peripheral” collisions should be similar to proton-proton collisions which have been studied for decades at other high energy colliders and provide a good point of reference. As the nuclear overlap of the ions increases so does the energy and density of the interacting medium. Therefore signatures of a QGP are expected in collisions with a large amount of nuclear overlap.

This dissertation presents new correlation measurements of particles in transverse momentum ( $p_t$ ) space, or the momentum perpendicular to the beam axis, as a function of nuclear overlap. The findings are that, in peripheral collisions, it is most likely to observe pairs of particles both with a momentum around 1.5 GeV/ $c$ . This correlation signal is manifested as a broad peak in the 2D ( $p_t, p_t$ ) space. As events are selected with increasing amounts of nuclear overlap this peak increases in amplitude but remains at the same approximate location. Comparisons to theoretical models suggests the main source of correlations is from jet fragmentation.

Jets are defined experimentally as back-to-back sprays of collimated particles. They are a well-studied phenomena in electron-positron and proton-proton collisions and are accurately described by perturbative QCD [16]. Observing the properties of individual jets in collisions with a large amount of nuclear overlap is more challenging compared to single nucleon-nucleon collisions because of larger backgrounds. Nonetheless, it is an important and active analysis topic. Some analyses attempt to reconstruct single jets by selecting particles with a relatively high  $p_t$ , known as the trigger particle, and then clustering particles around this track to form a group of collimated particles (see for example [17]). Other analyses attempt to statistically reconstruct jets by forming correlations of the high  $p_t$  trigger particle with lower  $p_t$  “associated” particles. The reconstructed jets are found to be highly modified in collisions with a large nuclear overlap as compared to proton-proton collisions [18]. While this modification, referred to as “jet quenching”, only

indicates partonic energy loss, it is also proposed to be a signal of the thermalization of jet fragments in a color dense medium [19].

In heavy ion collisions, the total momentum of reconstructed jets are typically on the order of 10s of GeV. However, jet processes, as described by hard transverse scattering in QCD, continue down to parton transverse momentum amplitudes of a few GeV/ $c$  with hadron fragments much less than 1 GeV/ $c$ . This complete “minimum bias” jet spectrum can be accentuated via correlations with no  $p_t$  limits or clustering algorithms. Surprisingly, the minimum bias jets are still highly correlated in events with a large nuclear overlap. This does not support a QGP hypothesis in which particles should be thermalized and any initial structure should be erased.

The rich source of information contained in two-particle correlations makes it an active analysis topic with many publications. The interpretation of some of the observed correlation structures is actively debated [11, 20]. Two theories are that the system reaches thermal equilibrium and develops strong collective flow or the system is dominated by primary parton-parton scattering leading directly to fragmentation with little subsequent re-scattering.

This dissertation presents complete descriptions of the available correlation space in which theoretical models can be tested. For example, the momentum distribution of pairs correlated in the angular structure associated with jets is observed to peak around an intermediate  $p_t$  of 1.5 GeV/ $c$ . This momentum distribution does not soften with an increase in nuclear overlap and therefore does not support the idea of an opaque, QGP-like system.



### 1.3 Outline

The seven chapters contained in this dissertation encompass the author's analysis of  $\sqrt{s_{NN}} = 200$  GeV Au+Au collisions at RHIC with the STAR detector. Following this introduction Chapter 2 reviews the history of Brookhaven National Laboratory and experimental details of the RHIC accelerator complex and the STAR detector.

Chapter 3 motivates and derives the two-particle correlation measure after defining the relevant kinematic variables. The selection criteria on the event and track level are also documented and explained. Chapter 5 reviews previous two-particle correlation analyses and its origin in fluctuation measurements. Results from proton-proton collisions are examined before introducing more recent results in heavy-ion collision systems.

New measurements of two-particle correlations in transverse momentum space are presented in Chapter 5. The data are distinguished by the charge combination and relative opening angle of the pairs of particles. Features of the data are also quantified with a fit model. The analysis of the momentum dependence of angular correlation features is presented in Chapter 6. Concluding remarks are found in Chapter 7.

# Chapter 2

## Experiment Details

The United States has supported cutting edge research in national laboratories since the early 20th century. There are currently 17 national laboratories funded by the Department of Energy, 10 of which are under the guidance of the Office of Science including Brookhaven National Laboratory. This chapter provides relevant information about the experimental facilities needed to collect the heavy ion collision data for the present analysis.

### 2.1 Brookhaven

Brookhaven National Laboratory was established in 1947 in Upton, Long Island, New York with the goal to study atomic physics. The first large experiment built was the Cosmotron accelerator [21]. The Cosmotron accelerated protons up to 3.3 GeV, the energy frontier at the time and provided the first external beam of accelerated protons for other on-line experiments. In 1960 the Alternating Gradient Synchrotron (AGS) was constructed and led to many important achievements in physics including the discovery of the charmed baryon in 1975. Seven Nobel prizes in total have been awarded to Brookhaven scientists, not only in physics but also chemistry. In fact, many

fields of science are studied on the Brookhaven campus including nanotechnology, biomedicine, and environmental sciences [21].

Currently the premier facility at Brookhaven is the Relativistic Heavy Ion Collider (RHIC), the world's largest accelerator devoted to nuclear physics. RHIC's history begins with a failed project in the 1970s named ISABELLE (Intersecting Storage Accelerator + BELLE). ISABELLE was to have two intersecting proton rings and the latest technology in accelerator physics through the use of superconducting magnets. In 1978, after the project was funded and fully supported by US President Carter, the tunnel excavation began. However, problems soon developed in the fabrication of the superconducting magnets which lead to the eventual abandonment of the ISABELLE project [22].

Subsequent construction projects in the field for the next ten years were started and abandoned including the Colliding Beam Accelerator (CBA) and the Superconducting Supercollider (SSC). After the cancellation of the SSC project, the idea was conceived to use the existing tunnel dug for ISABELLE to start a new physics program to search for the Quark Gluon Plasma (QGP). In 1990 the RHIC project was funded and after ten years of construction it began to operate in 2000.

## **2.2 RHIC**

RHIC is a multipurpose machine capable of accelerating several species of ions from protons ( $N=1$ ) to Uranium ( $N=92$ ). These ions are accelerated in two separate counter-rotating beams 3.8 km (2.4 miles) in circumference up to

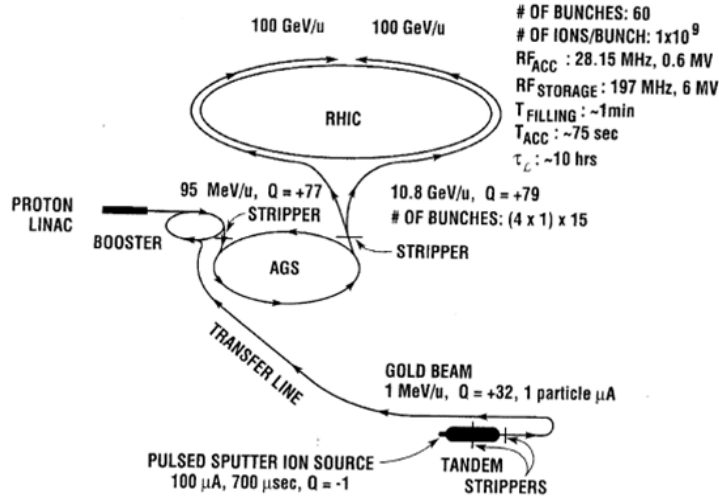


Figure 2.1: Diagram of the accelerator facilities at Brookhaven National Laboratory which provide Au+Au collisions

energies of 100 GeV/ $c$  for heavy ions and 250 GeV/ $c$  for protons [23]. RHIC is also the only accelerator capable of delivering high-energy polarized proton beams.

The process of creating heavy ion collisions will be described in detail through the life cycle of a gold (Au) ion accelerated to 100 GeV. Figure 2.1 illustrates the multi-stage process which begins at the ion source. Gold ions are made with a cesium sputter ion source operated in pulsed beam mode [24]. In pulse mode the source can produce a 500  $\mu s$  long pulse with a peak intensity of 290  $\mu A$  without causing damage to the accelerator. In 2010 the ion source was upgraded to the Electron Beam Ion Source (EBIS) which can deliver intensity on the order of mA [25].

After the cesium ion source creates a beam of negatively charged Au

ions, they are accelerated to +15 MeV from ground in the first section of the tandem Van de Graaf. The ions then pass through a thin carbon foil ( $2 \mu\text{g}/\text{cm}^2$ ) [26] which strips electrons from the ions until they are left in a +12 charge state. The positively charged ions are then accelerated back to ground potential in the second half of the Van de Graaf and exit with an energy of 1 MeV/nucleon. Upon exiting, the ions pass through another stripping foil and bending magnets select a beam of ions with a +32 charge state [23].

The ions then enter the Booster Synchrotron which bunches and accelerates the ions to 95 MeV/nucleon. More electrons are stripped as the bunches exit until the ions are charge +77 (helium-like). Next, the Alternating Gradient Synchrotron (AGS) accelerates the ions to 10.8 GeV/nucleon, the desired RHIC injection energy.

Finally, the four bunches which were made in the AGS enter the AGS-to-RHIC Beam Transfer line one at a time and are stripped of all remaining electrons. Each bunch contains  $10^9$  ions and is injected into one of the two counter-rotating beam lines via a steering magnet switch. This process is repeated until both beam lines are full which takes on the order of a minute [26].

The two counter-rotating beam lines are separated 90 cm horizontally and referred to as blue (clockwise) or yellow (counter-clock-wise). The ring shape of each beam-line is comprised of six arc segments 356 m long and six insertion sections 277 m long [23]. The insertion sections contain the crossing points centered in the RHIC detectors. Each arc has 11 segments that contain two dipoles, two quadrupoles, and two sextupoles. The dipoles provide

the magnetic force to move the beam particles in a circular path. One of the quadrupole magnets focuses the beam in the horizontal direction and subsequently defocuses it in the vertical direction. Therefore the second quadrupole magnet is rotated 90 degrees to focus the beam in the vertical direction while defocusing in the horizontal direction. The focusing power of the quadrupole magnets is dependent on the energy of the particles. Therefore any spread in the particle's energy results in a spread of the position. The focusing capabilities of the sextupole magnets are used to reduce this energy dependent spread.

At the time of this dissertation, RHIC has operated 11 physics runs since 2001 with 14 combinations of ion species and collision energy. The integrated luminosity as a function of time is shown in Fig. 2.2.

## 2.3 RHIC Detectors

Of the six intersection points located along the RHIC beam line four large-scale detectors have been constructed. Two of the detectors, PHOBOS and BRAHMS, have already been decommissioned after their physics goals were reached. PHOBOS was designed to analyze a large sample of heavy ion collisions but only detect a small portion of each event. Measurements of fluctuations in particle production were used to determine the possible temperature, size, and density of the dense heavy ion environment. In contrast, BRAHMS was designed to measure particles production over a large acceptance, a wide range of transverse momentum, and with good particle iden-

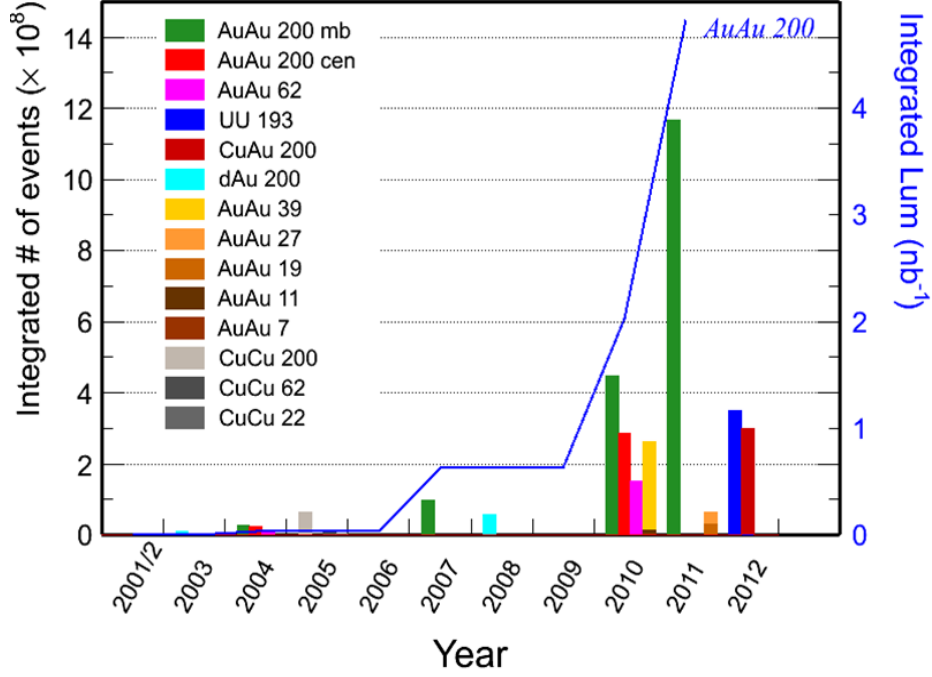


Figure 2.2: Heavy-ion collisions at RHIC recorded by STAR and the integrated luminosity (blue line) [1].

tification. BRAHMS measurements complemented the data taken by more precise, smaller acceptance detectors.

The two detectors still active are PHENIX and STAR. PHENIX (the Pioneering High Energy Nuclear Interaction eXperiment) has a large pseudo-rapidity coverage but with significant acceptance gaps [27]. It consists of three magnetic spectrometers, one main central spectrometer and two arms to the west and east [23]. PHENIX also has two muon arms to the north and south which help with tracking and identification of leptons. Overall PHENIX is optimized to study specific process by tracking and identifying

leptons, hadrons, and photons.

## 2.4 STAR

The data used in this dissertation were detected by the STAR (Solenoidal Tracker At RHIC) experiment. STAR is designed to measure basic properties of most of the produced particles over a relatively large acceptance. Like many other high energy detectors it is a system made up of many specialized components as seen in Fig. 2.3. A section will be devoted specifically to the Time Projection Chamber (TPC), which many consider to be the heart of STAR. Other detectors such as the Time Of Flight (ToF) and the Electromagnetic Calorimeter (EMC) will be briefly described in this section. Detectors used for triggering (selecting events to be recorded) such as the Central Trigger Barrel (CTB) and Zero Degree Calorimeter (ZDC) will be described in Sec. 3.2.1.

### 2.4.1 TPC

Most analyses in STAR rely heavily on the track position and momentum information provided by the Time Projection Chamber (TPC). For a period, STAR's TPC was the largest in the world with a 4 m diameter, 4.2 m length and full azimuthal coverage ( $2\pi$ ). Only in 2004 when the TPC in the ALICE experiment at the Large Hadron Collider was built was it surpassed in size. STAR's TPC can record charged particle momenta greater than 100 MeV/ $c$  and up to 30 GeV/ $c$  [28]. The tracking capabilities of the TPC are even more impressive in a dense environment where a single ion-ion collision



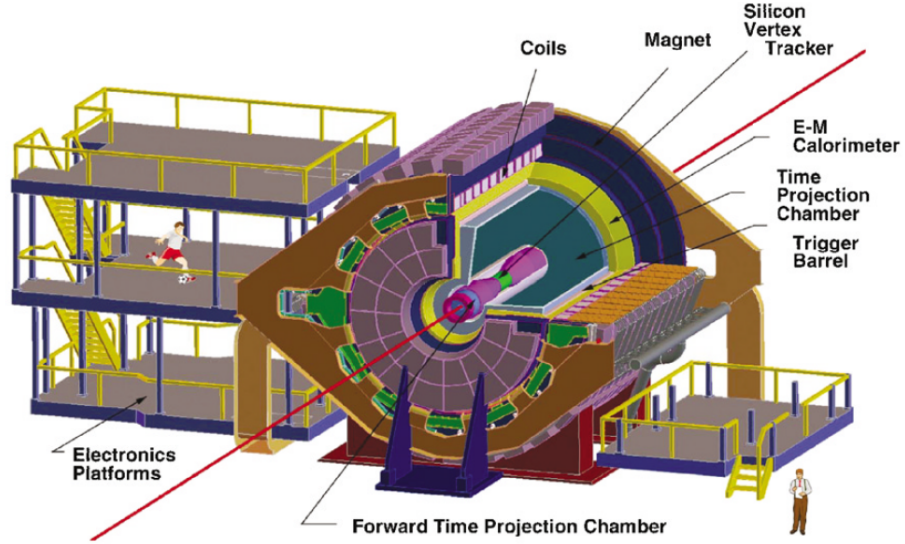


Figure 2.3: A cutaway view of the STAR detector to view inner detectors active in 2004 [2].

routinely contains over a thousand particles.

A charged particle traveling through the TPC leaves signals along its path via ionization of the TPC gas. The released electrons drift to the nearest end of the TPC via an electric field which is pointed in opposite directions in each half of the TPC. The 135 V/cm electric field is generated by the thin conductive central membrane, an inner and outer field cage and the end caps as seen in Fig. 2.4 [28]. The electrons then avalanche at the readout system in the endcaps, amplifying the signal 1000-3000 times.

The amount of time the electrons travel to the end caps and the drift velocity ( $5.45 \text{ cm}/\mu\text{s}$ ) provide a measurement of the particle position along the z-axis (beam direction). The position along the radial and azimuthal

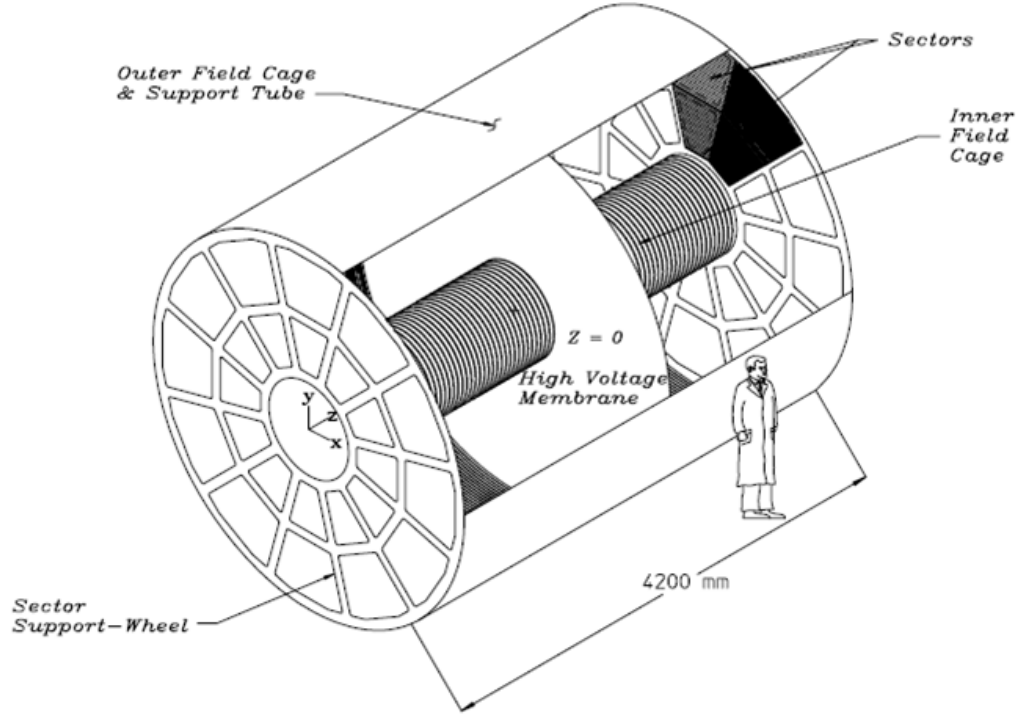


Figure 2.4: A diagram of the STAR TPC detector.

directions are determined by the highly segmented Multi-Wire Proportional Chambers (MWPC) readout system in the end caps. The MWPC measures a temporary image charge induced from positive ions that are produced in the electron avalanche. The MWPC at each end is divided into 12 sectors with 5692 pads each. The best tracking efficiency is for high momentum particles perpendicular to the beam line at 96% [28]. The inefficiency is due to the sector boundaries. Embedding analyses estimate the systematic error on the tracking efficiency to be 6% [28]. The momentum resolution for pions is about 2%.

The TPC is filled with a mixture of 10% methane and 90% argon gas at 2 mb above atmospheric pressure. This gas mixture has a fast drift velocity at a low electric field which reduces the sensitivity to fluctuations in temperature and pressure [28].

The TPC operates inside a 0.5 T magnetic field oriented along the length of the cylinder. The magnetic field is generated by a cylindrical solenoidal magnet that has a radius of approximately 230 cm, a length of 5.6 m and weighs more than 1100 tons [29]. The force generated by the magnetic field curves the trajectory of charged particles in the transverse plane via the Lorentz force and the amount of curvature gives a measure of the particle's momentum through the relation ( $\vec{p} = q\vec{B}r$ ). The magnetic field needs to be strong enough to bend the trajectories of high momentum particles but weak enough to allow the tight spiral of low momentum particles to reach the detector volume, which is located 50 cm from the beam pipe. The homogeneity of the magnetic field also effects the uncertainty in the reconstructed track positions. The distortion of the magnetic field in STAR is estimated to be  $\pm 0.0040$  T.

Particle identification is also possible because the amount of energy loss by a particle in the TPC via ionization ( $dE/dx$ ) is related to its velocity through the Bethe (also known as Bethe-Bloch) equation [30]. Fig. 2.5 shows the relationship between  $dE/dx$  and transverse momentum. The red curves represent predictions from Bethe-Bloch for various mass assumptions. Fits to these distributions can be used to identify particles with varying levels of accuracy that depend on the amount of overlap.

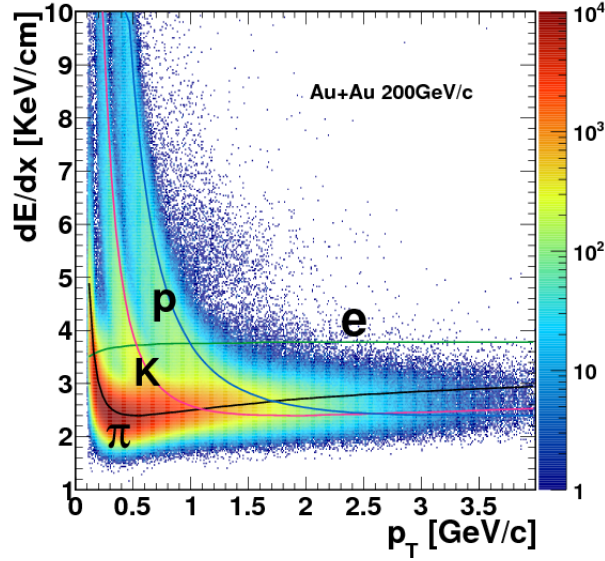


Figure 2.5: Ionization energy loss ( $dE/dx$ ) as a function of transverse momentum ( $p_t$ ) for 200 GeV Au+Au collisions. Figure provided by Masayuki Wada.

The acceptance of the TPC was also extended with a Forward TPC (FTPC) detector system located on each side close to the beam pipe.

#### 2.4.2 Other Detector Subsystems

STAR has the capability to measure deposited energy in the electromagnetic calorimeter (EMC) comprised of a full-barrel calorimeter (BEMC) and an endcap (EEMC) with a full azimuth acceptance. The EMC samples the deposited energy of photons and electrons created from the collision directly, as well as electromagnetically decaying hadrons [2]. The energy is measured via layers of lead and plastic scintillators. The size and cost constrained the specifications of the detector which has a total depth of about twenty radiation

lengths at the center [31].

In 2010 STAR was upgraded with a new particle identification detector system called the Time-Of-Flight (TOF). Since TOF was intended to replace the Central Trigger Barrel (described in Sec. 3.2.1) the physical specifications were designed to match exactly. The total system consists of 120 trays located just outside the TPC as seen in Fig. 2.3. The 60 detectors in each half cover  $2\pi$  in azimuth and span approximately 5 m in total length (two trays end-to-end).

The TOF system improves particle identification with a precise measurement of the velocity  $\beta$ , which combined with momentum information obtained with the TPC are directly related to the particle’s mass. A complete description of the TOF system and variables can be obtained from Ref. [32]. The velocity and mass relation is found in Eq. 2.1.

$$\frac{1}{\beta} = c \frac{t_{stop} - t_{start}}{\Delta d} \quad (2.1)$$

$$m = \frac{p}{\gamma\beta c} = \frac{p\sqrt{1-\beta^2}}{\beta c} = \frac{p}{c} \sqrt{\frac{1}{\beta} - 1}$$

The velocity requires two time measurements. The time of the initial collision  $t_{start}$  is measured with two new vertex position detectors known as upVPDs. The time at which the particle reaches the TOF trays is the final “stop” time  $t_{stop}$ . With a precise measurement of the distance to the TOF trays  $\Delta d$ , a measurement of the velocity is possible.

The essential components in each TOF tray are 32 Multi-gap Resistive Plate Chambers (MRPCs). An MRPC consists of five glass layers with uniform

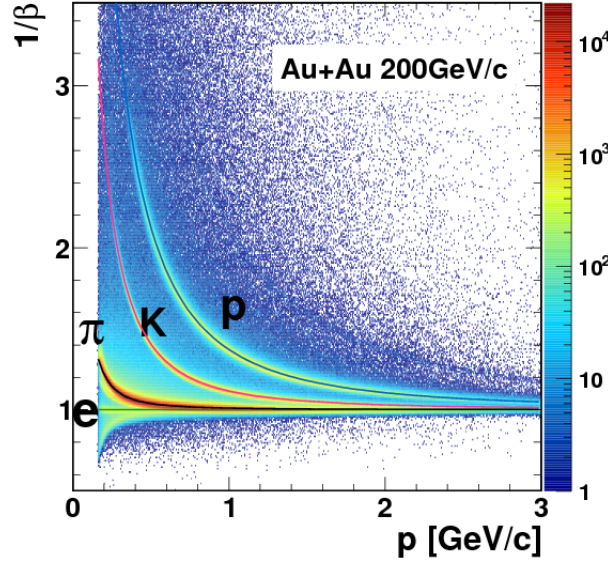


Figure 2.6: A scatter plot of track information,  $1/\beta$  vs momentum ( $p$ ) for 200 GeV Au+Au collisions. Figure provided by Masayuki Wada

gaps in which a mixture of 95% Freon and 5% iso-butane flow. As particles stream through the MRPC many small electron avalanches are created in each gap, which improves the timing resolution compared to one large avalanche. The electrons drift toward the top of the MRPC due to a strong electric field. The sum of the avalanches are read out by electronics connected to six channels per MRPC. The measured timing resolution of the TOF detector is 90 ps.

The fully installed TOF system has been very successful. The separation power of particle species is extended to higher momentum as seen in Fig. 2.6. Future work in this analysis will include correlations of identified particles which is made possible with the results from TOF.

# Chapter 3

## Analysis Details

The two-particle correlation results presented in this dissertation rely on a high level of data quality and precise measurement techniques. After introducing the kinematic variables relevant to the data, the event and track cuts used to reduce experimental artifacts or detector inefficiencies are described. Lastly the process to form a meaningful statistical measurement of correlations in heavy ion collisions is outlined.

### 3.1 Variables

Most analyses at STAR are based on information gathered by STAR's TPC, which detects the path of particles streaming through ionizing gas in a magnetic field. Since the TPC is cylindrically shaped, an obvious choice to describe the trajectory is cylindrical coordinates. Cylindrical coordinates contain a height  $z$  (beam direction), azimuthal angle  $\phi$ , and radial distance  $r$ . However, the position along the cylinder ( $z$ ) is dependent on the arbitrary interaction point and holds no physics meaning. A coordinate system with a well defined center makes more sense. Spherical coordinates satisfy this condition and are usually described with an azimuthal angle  $\phi$ , a radial distance

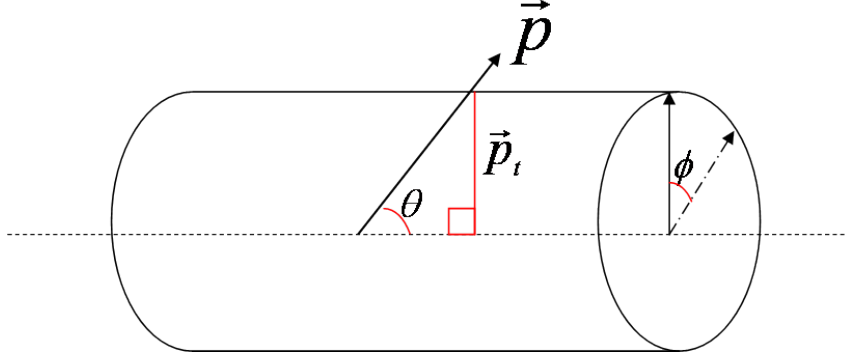


Figure 3.1: Coordinate system drawn over an outline of the TPC volume

$r$ , and a polar angle  $\theta$ .

Figure 3.1 presents these variables within the TPC acceptance. The radius is the component of the momentum vector in the  $x$  and  $y$  plane (perpendicular to the beam) and is known as transverse momentum  $p_t$ . The polar angle  $\theta$  measures the angle of the momentum vector with respect to the beam axis. However, the properties of the relativistic variable pseudo-rapidity  $\eta$ , which is a function of the polar angle  $\theta$ , are more advantageous. This is primarily because particle production is constant on the variable pseudo-rapidity, unlike  $\theta$ .

Pseudo-rapidity is derived from the variable rapidity  $y$  in the high-energy limit. Rapidity can be thought of as a measure of relativistic velocity. The benefit is that, unlike relativistic velocities, rapidity is additive, “the rapidity of the particle in one frame of reference is related to the rapidity in another Lorentz frame of reference by an additive constant” [33]. Therefore the difference in  $\eta$  values is independent of the Lorentz boost along the beam



axis. Rapidity is dimensionless and defined as,

$$y = \frac{1}{2} \ln \left( \frac{p_0 + p_z}{p_0 - p_z} \right), \quad (3.1)$$

where  $p_0$  is the energy of the particle and  $p_z$  is the z-axis component of the momentum vector  $\vec{p} = (p_x, p_y, p_z)$ .

Measuring the energy of a particle requires knowledge of the mass which is not easily obtained in most experiments. However, when the energy is much greater than the mass we can assume  $p_0 \rightarrow |\vec{p}|$ . With some algebra, rapidity  $y$  in the high energy limit becomes pseudo-rapidity  $\eta$ , and is defined in the second line of Eq. 3.2.

$$\begin{aligned} y \xrightarrow{E \gg m} &= \frac{1}{2} \ln \left( \frac{|\vec{p}| + |\vec{p}| \cos \theta}{|\vec{p}| - |\vec{p}| \cos \theta} \right) = \ln \left( \frac{1 + \cos \theta}{1 - \cos \theta} \right)^{1/2} \\ \eta &= -\ln[\tan(\theta/2)] \end{aligned} \quad (3.2)$$

In this dissertation the two-particle correlation data on transverse momentum ( $p_t = \sqrt{p_x^2 + p_y^2}$ ) will be presented instead as a function of transverse rapidity  $y_t$  because it improves visual access. This is because the transverse component of rapidity,  $y_t$ , is essentially the logarithmic measure of  $p_t$ . Transverse rapidity is defined as

$$y_t = \frac{1}{2} \ln \left( \frac{p_0 + p_t}{p_0 - p_t} \right) \rightarrow y_t = \ln \left( \frac{m_t + p_t}{m_0} \right), \quad (3.3)$$

where  $m_t = \sqrt{p_t^2 + m_0^2}$  is the transverse mass. Transverse rapidity has a well defined zero due to the  $m_t$  offset, unlike a purely  $\ln(p_t)$  measure. Since the present analysis is of unidentified particles, the mass  $m_0$  is arbitrary. The pion

mass is the default choice for  $m_0$  because the majority of particles are pions and the value is below the measured  $p_t$  range, thus  $y_t$  closely approximates  $\ln(p_t)$ .

## 3.2 Event Selection

Events are a collection of information recorded in a specific time window by the suite of detectors in response to a selection criteria. Event selection aims to identify information which corresponds to a genuine and desired physics event (e.g. a nucleon-nucleon collision). Event selection occurs throughout the data acquisition and analysis process from the earliest stages by the data acquisition system (DAQ) to the later stages by researchers with specific analysis goals.

### 3.2.1 Trigger

A trigger is a set of criteria used to accept or reject an event during data collection. They are an important part of the STAR experiment since the beam-beam interaction rate in 2004, for example, was 10 MHz while slow detectors such as the TPC can only process information at rates of 100 Hz [34]. Triggering allows the events with the most potential for meaningful physics to be flagged and recorded. The triggers are separated into levels based primarily on the speed of execution. The lowest level (L0) is executed with the fastest detectors and is able to reduce the event sample by many orders of magnitude. The next levels of triggers take more time to process so the data recording

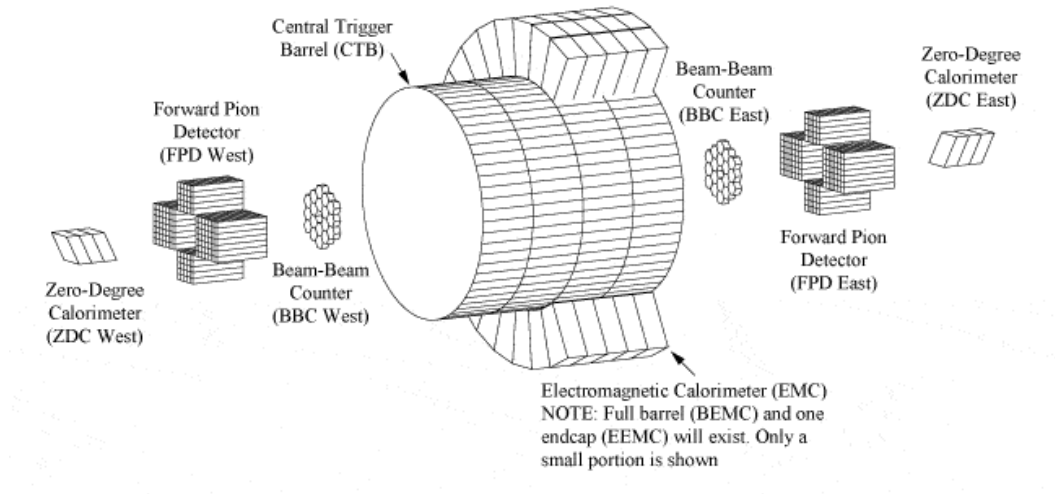


Figure 3.2: Fast trigger detectors in STAR.

begins immediately but the process is aborted if the event is rejected. The storage rate of events that pass all trigger levels is approximately 5 Hz [34].

The L0 trigger in 2004 used information recorded by the Central Trigger Barrel (CTB) and the Zero-Degree Calorimeters (ZDC) detectors [34]. The CTB was the next layer of detectors outside the TPC and consisted of 240 scintillator slats which covered a pseudo-rapidity range of  $|\eta| < 1$  and  $2\pi$  in azimuth. The CTB's main objective was to record the number of charged particles over a large solid angle. The CTB was fully decommissioned and replaced in 2010 by the Time-Of-Flight system.

The ZDC consists of two detectors on either end of the STAR detector close to the beam pipe as seen in Fig. 3.2. It detects neutrons through layers of

lead and scintillators with a timing resolution of about 100 ps. The detected “spectator” neutrons were freed during the heavy ion collisions and continued traveling down the beam pipe. The path of positively charged spectator protons are bent by the steering magnets while the neutrons continue unaffected towards the ZDC. The maximum number of freed neutrons are detected in collisions that partially overlap because the interactions are large enough to dislodge neutrons from the nucleus but not be completely destroyed. Conversely, the minimum number of neutrons are detected in collisions with a minimal or maximal nuclear overlap. In any case, a coincidence in signals from both of the ZDC detectors is used to identify an event. Furthermore, the small difference in timing of the signals detected in the two ZDCs provides a way to measure the location of the collision vertex.

The STAR collaboration labels triggers with a word briefly describing the motivation behind the selection criteria. Some of the most common trigger words are “minimum bias”, “central”, “UPC”, and “high tower”. A minimum bias trigger flags events that pass the least restrictive cuts in an effort to collect a comprehensive sample of heavy ion collisions. The data in this dissertation were labeled as minimum bias meaning the CTB sum was greater than 75 (in arbitrary units proportional to the number of charged particles) and the ZDC signal was greater than some threshold, typically about 40% of the single neutron peak in both the east and west detectors. The distribution of events with respect to these two quantities is shown in Fig. 3.3.

A central trigger is used to record collisions with a large nuclear overlap

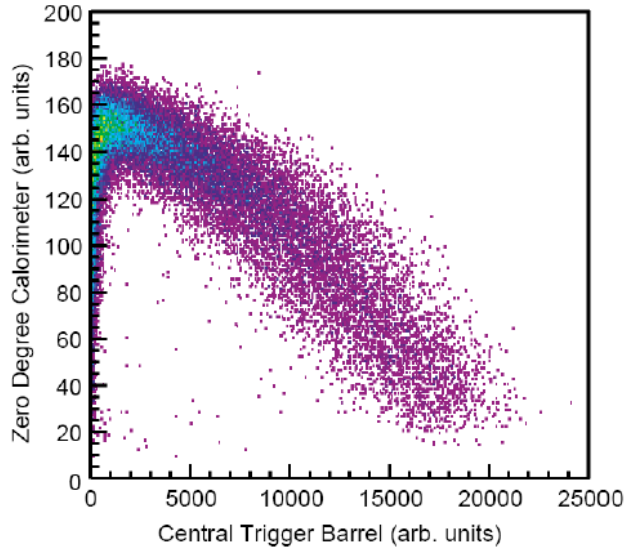


Figure 3.3: The distribution of events with respect to summed signal amplitudes from the CTB and ZDC [3].

(high multiplicity). This trigger includes the minimum bias requirements plus a higher threshold of multiplicity in the CTB and a lower number of spectator neutrons in the ZDC. The ultra peripheral collision (UPC) trigger selects collisions with a small nuclear overlap. The high tower trigger selects events with a large amount of energy deposited in the calorimeter and is most often used in jet physics analyses.

Other detectors used for triggering, but not for the minimum bias trigger in 2004, include the Beam-Beam Counter (BBC), the electromagnetic calorimeter (EMC), and the Forward Pion Detector (FPD). The BBC provides a measurement of the position of the interaction along the beam pipe using precise timing information from two detectors located on either side of

the TPC. The EMC can identify events with large amounts of energy deposited in its lead-scintillator sections. The FPD, which detects neutral pions, is used mostly during polarized proton running.

### 3.2.2 Vertex Cut

The two counter-rotating beams at RHIC are steered to intersect as close to the center of the STAR detector as possible. Collisions at the center of the detector are ideal because the solid angle covered by the detectors is maximized. Realistically, the beam-beam intersection volume can vary on the order of tens of centimeters from the geometric center of the detector. Events are selected with intersection points in specific ranges along the beam axis to control the amount of variation of the detector coverage. A reasonable z-vertex range for minimum bias analysis studies in 2004 data was chosen to be  $|z| < 25$  cm.

### 3.2.3 Pileup

For each triggered event the TPC records data for approximately  $40 \mu\text{s}$  to allow the ionized electrons enough time to reach the electronics on either end of the TPC. All tracks reconstructed during this time window are known as global tracks. The global tracks are then processed further to determine those associated with the primary collision vertex, known as “primary” tracks. The mistaken association of tracks from other collisions with the primary collision vertex is called pileup. In high luminosity conditions, where the density of ions

in a bunch is high, pileup is most often caused by multiple interactions within a single bunch crossing. However, in the experimental conditions for this data (average luminosity of  $5 \times 10^{26} \text{ cm}^{-2}\text{s}^{-1}$ ), the probability of having two or more interactions per beam crossing is very small. The term “pileup” will instead, due to the relatively slow readout time of the TPC, be used to describe the situation in which tracks from collisions that occurred before or after the triggered event, in a separate beam crossing, are mistakenly associated with the primary collision.

This type of pileup is a probable occurrence in STAR data because the TPC electronics take  $40 \mu\text{s}$  to record a triggered event while a bunch crossing occurs every  $120 \text{ ns}$  [2]. Therefore there is a distinct possibility that a particle’s track from another collision will be measured at the same time as a triggered event in the TPC. Most often these pileup tracks can be eliminated in the first level of event reconstruction because pileup tracks generally do not point to a reconstructed vertex or begin at a distance far away from the reconstructed vertex. However, cases in which pileup tracks are incorrectly grouped with the primary collision result in significant unwanted structure in correlation data.

It was estimated that 2004 Au+Au data contained approximately 0.5% pileup [11]. Even this small amount of pileup contamination has a noticeable effect on minimum bias correlation data, mostly due to a smaller  $\eta$  range of pileup tracks versus real tracks that have an  $\eta$  range of approximately 2 units. This mismatch in the  $\eta$  range of pileup events causes a characteristic “w” shape in angular correlations. This has necessitated the use of an additional

pileup filter over what is used in other analyses in order to eliminate the effects. Duncan Prindle at the University of Washington developed a pileup filter that eliminates almost all indications of pileup contamination in the two-particle correlation data [4]. It utilizes unique signatures of track distributions created from pre- and post-pileup events.

The ionized electrons produced from particles in a collision that occurred before the triggered event (pre-pileup) will travel through the TPC for a period of time before the readout clock begins. This mismatched timing creates a distinct signature from the particles that cross the central membrane, which produce ionized electrons that drift to both ends of the TPC. The tracks from particles that crossed the central membrane before the readout clock began will appear as if they began a distance  $d$  from the central membrane on both ends of the TPC as seen in Fig. 3.4. The distance the tracks are shifted from the central membrane is the product of the drift velocity in the TPC and the time between the pileup collision and the primary collision.

The tracks in the right panel of Fig. 3.4 that were split at the central membrane will have the same starting value on the z-axis ( $z_{\text{first}}$ ) in the TPC half not containing the pileup vertex and the same ending values ( $z_{\text{last}}$ ) in the TPC half containing the pileup vertex. The pileup filter utilizes this signature of a peak in the  $z_{\text{first}}$  and  $z_{\text{last}}$  positions roughly the same distance apart from the central membrane. An example of this signal is shown in Fig. 3.5. In addition, this pileup collision will have two reconstructed vertices that are separated the same distance between  $z_{\text{first}}$  and  $z_{\text{last}}$  ( $2d$ ).



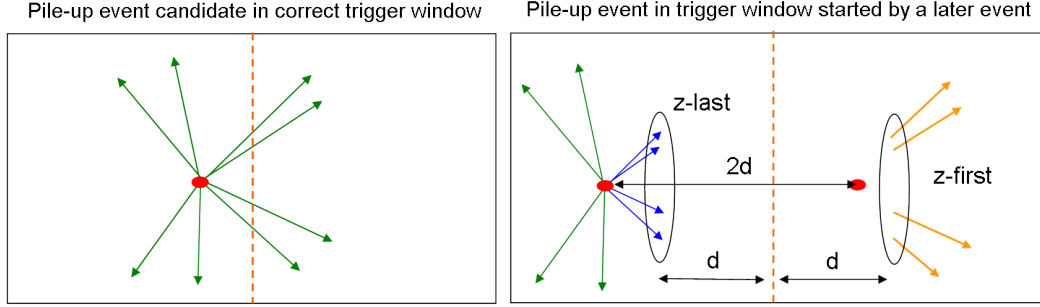


Figure 3.4: Cartoon of pre-pileup in two frames of observation. The event is triggered from the pileup collision (left panel). The collision occurs some time before the triggered event (right panel). The tracks from particles that cross the central membrane are split in the right panel into two different colors (blue and yellow) that correspond to one track in the left panel.

A collision that occurs some time after the triggered collision is also a source of pileup. In this scenario the TPC readout clock stops before all the ionized electrons from post-pileup particles reach the ends of the TPC. Therefore, the reconstructed paths of all the pileup particles abruptly stop some distance,  $d$ , from the ends of the TPC as seen in Fig. 3.6.

The signature of these events is a peak in the  $z_{\text{last}}$  values on both sides of the TPC. The peak position will correspond to the product of the drift velocity in the TPC and the time between the triggered and pileup collision. This peak will also be symmetric on both ends of the TPC as seen in Fig. 3.7.

The risk of pileup contamination in our primary event sample will occur when reconstructed pileup vertices are very close to the primary vertex from the event. There are four sources of information used to identify pileup vertices: the histograms of  $z_{\text{first}}$  and  $z_{\text{last}}$  as described above; and the dis-

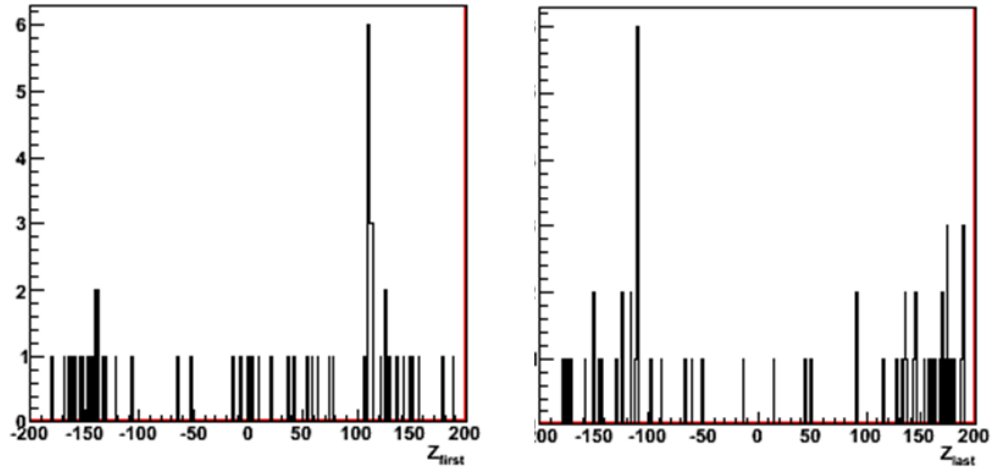


Figure 3.5: Histograms of the first and last position of global tracks in an event that contains pre-pileup [4].

tribution of all tracks in each side of the TPC. For triggered events, a vertex that is reconstructed from only tracks in one side of the TPC should match the vertex reconstructed from tracks in the other side, while for events with pre-pileup the two vertices should not match [35]. Comparing the pairs of vertices from both methods is also a good way to identify pileup events.

The filter developed by Duncan Prindle uses the pileup vertices determined from the histograms of  $z_{\text{first}}$  and  $z_{\text{last}}$ , which are directly related to the separation distance of the reconstructed pileup vertices ( $2d$ ), and compares it to the good primary vertex stored with the event. If the distance is too small then the reconstructed primary vertex probably contains tracks from the pileup collision. If it is large then it probably did not contaminate the pri-

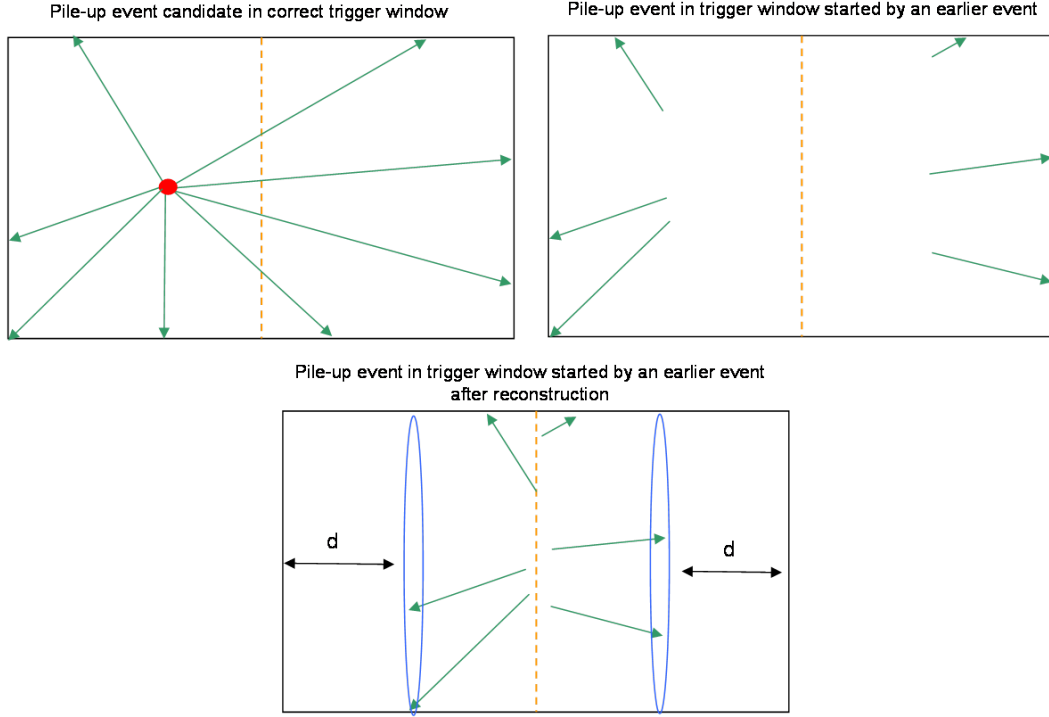


Figure 3.6: Cartoon of a collision in three scenarios. The event is triggered from the collision (top left). The collision occurs some time after a triggered event (top right). The reconstructed positions of tracks (bottom).

mary collision. For the present analysis, events were cut that had a separation distance less than 20 cm.

The efficiency of this pileup removal procedure  $f$  is estimated to be  $75 \pm 10\%$  [11]. Most of the inefficiency is caused by tracks that do not cross the central membrane which is an important feature in identifying pre-pileup. The correlation measure can be extrapolated to a fully pileup removed sample by solving the two equations in Eq. 3.4. The quantity  $\Delta\rho/\sqrt{\rho}$  is the correlation measure and will be described in more detail in this chapter.

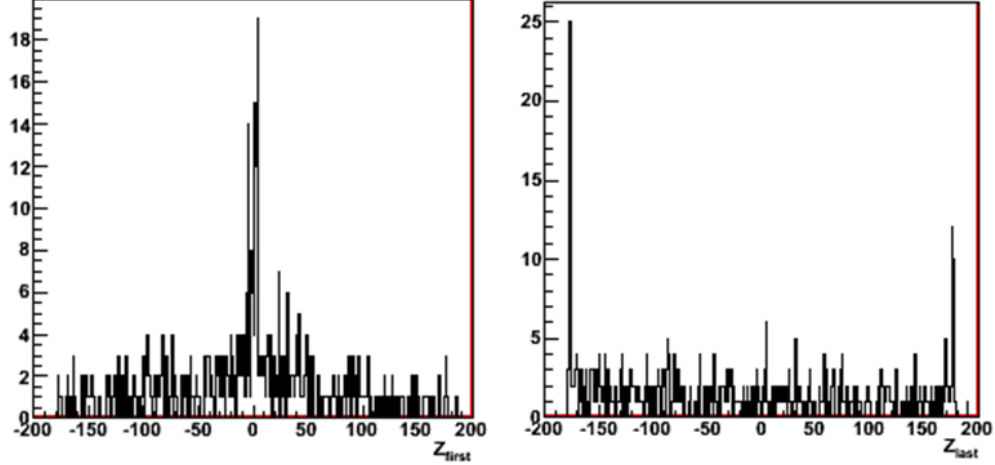


Figure 3.7: Histograms of the first and last position of global tracks in an event that contains pileup tracks from after the triggered collision [4]

$$\begin{aligned}
\frac{\Delta\rho}{\sqrt{\rho_{ref}}}(\text{no filter}) &= \frac{\Delta\rho}{\sqrt{\rho_{ref}}}(\text{no pileup}) + \frac{\Delta\rho}{\sqrt{\rho_{ref}}}(\text{pileup}) \\
\frac{\Delta\rho}{\sqrt{\rho_{ref}}}(\text{with filter}) &= \frac{\Delta\rho}{\sqrt{\rho_{ref}}}(\text{no pileup}) + (1 - f) \frac{\Delta\rho}{\sqrt{\rho_{ref}}}(\text{pileup}) \quad (3.4)
\end{aligned}$$

This extrapolation procedure required the complete data set to be analyzed twice, with and without the pileup filter.

### 3.2.4 Centrality

STAR was designed to study properties of nuclear matter at high energies and densities. The energy density of the colliding system is dependent on the volume of nuclear material interacting during the ion-ion collision. This volume, related to the amount of nuclear overlap, can not be predetermined

by the experiment nor observed directly. However, with model calculations it can be related to the number of charged particles produced  $N_{ch}$ , also known as the multiplicity. This classification of events with respect to multiplicity as a proxy for nuclear overlap is called centrality.

The centrality of events are indicated by percentages ranging from 0 to 100%. The percentage reflects the fraction of events in a  $N_{ch}$  range, where 0% indicates the most overlap or most central and 100% indicates the least overlap or most peripheral. In other words, the 0 – 5% centrality fraction consists of 5% of the total number of events with the the highest  $N_{ch}$ .

The first step in defining centrality fractions is to plot the frequency of events versus multiplicity which is shown in the left panel of Fig. 3.8 for 11 million Au+Au 200 GeV events taken in 2004. The multiplicity in this case is for all accepted tracks used in the analysis ( $p_t > 0.15$  GeV/c,  $|\eta| < 1$ ,  $\phi < 2\pi$ ).

Plotting the multiplicity distribution on a log-log scale revealed an apparent “power-law” trend [36] as seen in the third panel of Fig. 3.8. The slope is approximately  $n_{ch}^{-3/4}$  ( $\frac{d\sigma}{dn} \propto n^{-3/4}$ ). This observation motivated a transformation of variables that would create a distribution that is approximately constant as a function of  $n^{1/4}$ .

The  $n^{3/4}$  factor can be thought of as a Jacobian in the transformation

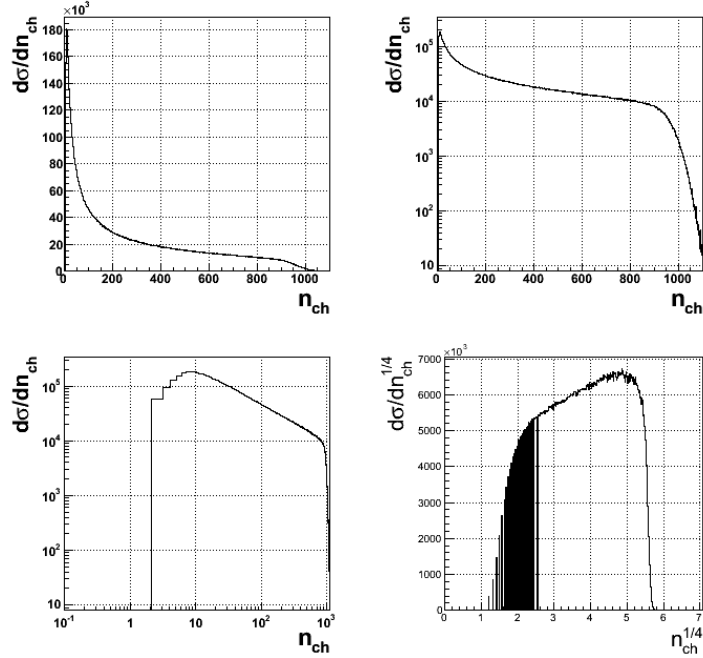


Figure 3.8: Plots of the multiplicity distribution of events from Au+Au 200 GeV 2004 collisions on various scales.

$$dn \rightarrow dn^{1/4}.$$

$$\begin{aligned}
\frac{d\sigma}{dn} n^{3/4} &\propto \text{constant} \\
n = (n^{1/4})^4 \rightarrow dn &= 4 (n^{1/4})^3 dn^{1/4} = 4n^{3/4} dn^{1/4} \\
n^{3/4} &= \frac{1}{4} \frac{dn}{dn^{1/4}} \\
\frac{d\sigma}{dn} n^{3/4} &= \frac{1}{4} \frac{d\sigma}{dn^{1/4}} = \text{constant} \tag{3.5}
\end{aligned}$$

Therefore plotting  $\frac{d\sigma}{dn^{1/4}}$  versus  $n^{1/4}$  should result in a distribution that is roughly square as seen in the lower right panel of Fig. 3.8. This shape facilitates the process of dividing the event distribution into bins of equal statistics. However, the left edge at low  $n^{1/4}$  is diminished by trigger and

vertex finding inefficiencies. A corrected value of the half-maximum location on the left edge can be calculated via a Monte Carlo Glauber model simulation of nucleus-nucleus collisions convoluted with the multiplicity distribution of single nucleon-nucleon (p+p) collisions [37]. Data from p+p collisions are more reliable because it suffers from less trigger inefficiencies and background contamination. A Monte Carlo Glauber simulation samples some parent distribution for a value of the impact parameter and the nucleons that overlap according to a Wood-Saxon distribution are allowed to interact. The result of the convolution is a value of the left edge half-maximum location on the x-axis of approximately one-half the mean  $N_{ch}$  for p+p collisions [36]. The distribution in the lower right panel is then shifted according to this value. The upper end point of the multiplicity distribution, located where the impact parameter is effectively zero, is also effected by trigger inefficiencies and is corrected via a parametrization of the shape of the distribution. More details on the process of correcting the centrality definitions can be found in Ref. [37].

The Glauber model along with the power-law procedure provided efficiency corrected centrality definitions. The final centrality definitions used in this analysis are presented in Table 3.1.

### 3.3 Track Selection

A reconstruction code creates particle “tracks” by connecting signals, or “hits”, in the TPC that are made when charged particles ionize the gas. Properties of the reconstructed tracks can be used to judge the probability

Raw Centrality (%)	Corrected Centrality (%)	Multiplicity $N_{ch}$	$\nu$
90 - 100	84 - 93	<b>2 - 14</b>	1.40
80 - 90	74 - 84	<b>15 - 34</b>	1.68
70 - 80	64 - 74	<b>35 - 67</b>	2.00
60 - 70	55 - 64	<b>68 - 116</b>	2.38
50 - 60	46 - 55	<b>117 - 151</b>	2.84
		152 - <b>186</b>	
40 - 50	38 - 46	<b>187 - 233</b>	3.33
		234 - <b>280</b>	
30 - 40	28 - 38	<b>281 - 340</b>	3.87
		341 - <b>401</b>	
20 - 30	18 - 28	<b>401 - 450</b>	4.46
		451 - 500	
		501 - <b>550</b>	
10 - 20	9 - 18	<b>551 - 613</b>	5.08
		614 - 675	
		676 - <b>738</b>	
5 - 10	5 - 9	<b>739 - 795</b>	5.54
		796 - <b>851</b>	
0.25 - 5	0 - 5	<b>852 - 901</b>	5.95
		902 - 951	
		952 - <b>1001</b>	

Table 3.1: Centrality definitions as a function of  $N_{ch}$  for 2004 200 GeV Au+Au collisions with  $p_t > 0.15$  GeV/ $c$ ,  $|\eta| < 1$ , and  $\phi < 2\pi$ . The centrality measure  $\nu$  is defined in Sec. 3.4.2

of it originating from the primary vertex or describing the particle's features accurately. The following section will outline the quality assurance cuts applied to reconstructed tracks in this analysis.

The curved path of charged particles in a magnetic field, to first order, is accurately described by a helical fit model [28]. The fit has an associated  $\chi^2$  per degree of freedom and this analysis required it to be less than 3. A



track could also be artificially split into two or more fragments during the reconstruction process. This typically occurs when the number of TPC hits used for a fit is less than 15. Therefore, the number of TPC hits used to fit a track was required to be between 15 and 50. Furthermore, the percentage of the number of fit points to the estimated maximum number of fit points must be greater than 52% and less than 110%. The estimate is made based on the position of the track in the TPC and also helps eliminate track fragments created during reconstruction.

A good event should only have tracks that originated very close to the primary vertex. In fact, the reconstructed vertex is found by extrapolating all the tracks in an event back to the origin and taking the average [28]. This distance of each track to the primary vertex is known as the distance of closest approach (DCA). Tracks from pileup, weak decays, and interactions of particles with detector material should generally have a large DCA. This contamination was reduced by requiring the DCA to be less than 3 cm. A tighter cut on this parameter was investigated in previous studies and judged to be unnecessary [3].

The curvature of the particle trajectory through the 0.5 T magnetic field is dependent on the charge and momentum. The lowest transverse momentum a track can have (i.e. the tightest curl) and still reach the TPC volume is approximately 0.15 GeV/ $c$  and thus becomes this analysis's lower  $p_t$  limit. Essentially no upper  $p_t$  limit is imposed because few tracks exceed our  $p_t$  maximum of 15.45 GeV/ $c$ . A plot of the momentum distribution of tracks

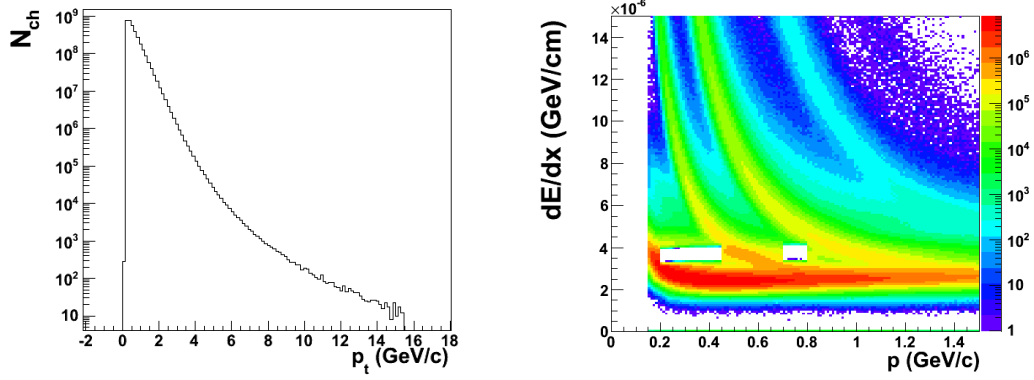


Figure 3.9: Distribution of tracks as a function of  $p_t$  (left) and  $dE/dx$  versus momentum (right) of 2004 200 GeV Au+Au collisions.

that passed all the quality cuts is in the left panel of Fig. 3.9. Tracks were also required to have a charge of  $\pm e$  and  $|\eta| < 1$ .

Many electrons detected in STAR did not originate from the original heavy ion collision but from interactions of photons with material in the detector which produce electron-positron pairs. For this analysis all electrons can be considered purely a source of background. The TPC's PID capabilities from the relationship between energy loss ( $dE/dx$ ) and momentum can be used to reduce the number of electrons. The momentum region with the clearest separation from other particle species in  $dE/dx$  is between  $0.2 < p < 0.45$  GeV/ $c$  and  $0.7 < p < 0.8$  GeV/ $c$ . A cut was made on all particles that fall within a  $1.5 \sigma$  band of the expected electron energy loss in these two momentum regions as evident in Fig. 3.9. This reduces the number of electrons to a level that can be handled easily in our correlation data.

### 3.3.1 Pair Cuts

The track reconstruction process is more difficult when the trajectories of two tracks are very close together or cross. It can result in unwanted merging or splitting of tracks. More information about the characteristics of track merging, splitting, and pairs cuts are found in Ref. [3].

Merging occurs when the separation distance is so small that two tracks are reconstructed as one. This is a consequence of the TPC's finite two hit resolution which is approximately 1 cm in the padrow direction and 3 cm in the drift direction [28]. Track merging reduces the total track count by one. This effect is important to address because the correlation measure that will be described in the next section involves forming a reference distribution with tracks from different events. Two tracks from different events will not risk merging together so the track count will not be potentially reduced. In order to form distributions that are equally biased, pairs of tracks from mixed events that would be too close together to reconstruct correctly if they had been produced in the same event are intentionally removed. Specifically, pairs of tracks that are separated by less than 5 cm at any of three points along the track in both the transverse (TPC drift direction) and the longitudinal direction (along the padrow direction) are cut, regardless if they originated from the same or different events.

When the paths of two tracks cross, the code might reconstruct as many as 4 different pieces. A similar method to track merging is applied here, however, the process of identifying potential splitting is more detailed. The

instances in which tracks might cross depends on the direction of the magnetic field, the charge of the particles and the relative difference in azimuthal angle. Any pair, whether from the same event or different events, that satisfies several conditions of potential track crossing and is separated by less than 5 cm at any checked point in the longitudinal direction is cut. The conditions for crossing are described in more detail in Ref. [3].

### 3.4 Two-particle correlation measure

The sheer number of particles produced in central heavy ion collisions makes it challenging to measure small physics signals. However, correlations have the ability to enhance these subtle structures in the dense particle background with no assumptions.

The correlation measure used in this analysis can be directly derived from Pearson's correlation coefficient. Pearson's correlation coefficient is defined as the covariance of variables  $x$  and  $y$  divided by the product of the standard deviations of  $x$  and  $y$ .

$$\text{Corr}(x,y) = \frac{\sigma_{xy}}{\sqrt{\sigma_x^2 \sigma_y^2}} \quad (3.6)$$

where  $\sigma_x^2 = \frac{1}{N} \sum_i^N (x_i - \bar{x})^2$  and  $\sigma_{xy} = \frac{1}{N} \sum_i^N (x_i - \bar{x})(y_i - \bar{y})$

In this form, the correlation amplitude can be any value between -1 (anti-correlated) and +1 (perfectly correlated) with 0 indicating no correlation.

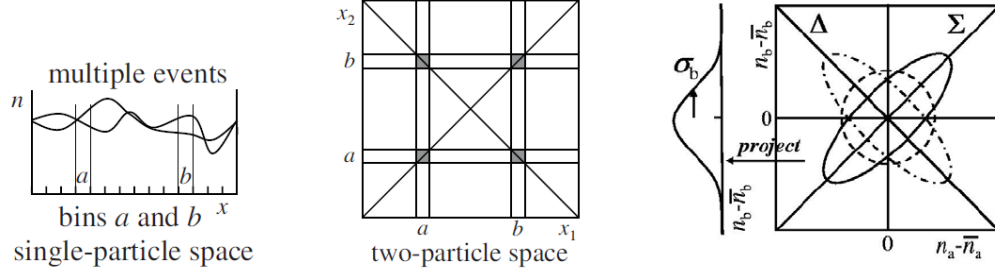


Figure 3.10: Distributions of particles in a 1D (left) and 2D (middle) space with bins  $a$  and  $b$  explicitly marked. The right panel labels the sum ( $\Sigma$ ) and difference ( $\Delta$ ) axes [5].

Traditionally, correlations are calculated between two separate distributions. However, this analysis measures the amount of correlation a distribution has with itself, known as an autocorrelation. A time-dependent autocorrelation is commonly used in signal processing.

The left panel of Fig. 3.10 illustrates an example 1D distribution from multiple events along the variable  $x$ . The second panel expands the distribution to two-dimensions  $(x_1, x_2)$ . The covariance of the contents of two bins  $(a, b)$  in this 2D distribution is defined as the following,

$$\begin{aligned}\sigma_{ab} &= \frac{1}{N} \sum_i^N \left( n_i(a) - \overline{n(a)} \right) \left( n_i(b) - \overline{n(b)} \right) \\ &= \overline{(n - \bar{n})_a (n - \bar{n})_b} = \overline{n_a n_b} - \bar{n}_a \bar{n}_b,\end{aligned}\tag{3.7}$$

where  $N$  is the total number of events,  $n_i(a)$  is the number of particles in bin  $a$  in event  $i$ , and  $n_i(b)$  is the number of particles in bin  $b$  in event  $i$ . This analysis fills two-particle distributions on  $(x_1, x_2)$  from all possible pairs of

particles where  $(x_1, x_2)$  is a subset of the six-dimensional coordinate space  $(p_{t1}, \phi_1, \eta_1, p_{t2}, \phi_2, \eta_2)$ .

The  $\overline{n_a n_b}$  term in Eq. 3.6 is the event-wise average of the number of particles in 2D bin (a,b). This is equivalent to forming all possible pairs of particles in the same event, known as sibling pairs. The second term of the covariance,  $\bar{n}_a \bar{n}_b$ , is the product of the statistical reference assuming  $n_a$  and  $n_b$  are uncorrelated. A good representation of an uncorrelated background is usually formed by pairing particles from similar but different events, known as mixed pairs.

The denominator of Pearson's correlation coefficient is the product of the variances  $(\sigma_a^2 \sigma_b^2)$ . In the present analysis the bin content  $n_a$  and  $n_b$  are measures of particle production and can be approximated with a Poisson distribution. The properties of a Poisson distribution are that each event is independent, has a known average and the variance  $(\sigma^2)$  is equal to the mean. The correlation can now be written as,

$$\text{Corr}(a,b) = \frac{\sigma_{ab}}{\sqrt{\sigma_a^2 \sigma_b^2}} \rightarrow \frac{\overline{n_a n_b} - \bar{n}_a \bar{n}_b}{\sqrt{\bar{n}_a \bar{n}_b}}. \quad (3.8)$$

The dependence on the size of the bins is removed by forming a density  $\rho$ , which is equal to the number of pairs  $n$  divided by the area of the bin  $\epsilon_{\text{area}}$ . Equation 3.7 becomes

$$\text{Corr}(a,b) = \frac{\rho_{sib} - \rho_{ref}}{\sqrt{\rho_{ref}}} = \frac{\Delta\rho}{\sqrt{\rho_{ref}}}, \quad (3.9)$$

where  $\rho_{sib} = \overline{n_a n_b} / \epsilon_{\text{area}}$  is the density of sibling pairs,  $\rho_{ref} = \bar{n}_a \bar{n}_b / \epsilon_{\text{area}}$  is the density of reference pairs and  $\Delta\rho = \rho_{sib} - \rho_{ref}$ .

Ideally the distribution of sibling pairs ( $\rho_{sib}$ ) contains only pairs correlated from physics. Unfortunately, the distribution also contains structure due to experimental artifacts such as acceptances and inefficiencies. However, the reference distribution formed from mixed pairs ( $\rho_{ref}$ ) also contains this structured background. Therefore it can be removed by forming the ratio  $r = \rho_{sib}/\rho_{ref}$ . To clearly state the intent to cancel experimental artifacts in the ratio  $r$ , the expression in Eq. 3.9 is rewritten as

$$\text{Corr}(a, b) = \sqrt{\rho_{ref}}(r - 1). \quad (3.10)$$

It is now essential that the “prefactor” ( $\sqrt{\rho_{ref}}$ ) be efficiency corrected. This requirement will be signified by a prime ( $\prime$ ) for the remainder of this dissertation. With this, the symbol which represents the correlation measure can now be defined as

$$\frac{\Delta\rho}{\sqrt{\rho_{ref}}} \equiv \sqrt{\rho'_{ref}}(r - 1). \quad (3.11)$$

This is a measure of the number of correlated pairs per particle. The “per-particle” correlation measure is appropriate for physics that is proportional to the final-state hadron multiplicity such as hadronization. A “per-pair”,  $\Delta\rho/\rho$ , measure can be appropriate for other analyses such as quantum correlations where the number of correlated pairs is proportional to the single-particle density squared.

### 3.4.0.1 Difference Variables

Due to properties of the data, the complete six-dimensional correlation space  $(p_{t1}, \eta_1, \phi_1, p_{t2}, \eta_2, \phi_2)$  can be reduced to 4 dimensions without any information loss. This reduction is justified by Fig. 3.11 which contains correlations on  $(\eta_1, \eta_2)$  and  $(\phi_1, \phi_2)$  for 130 GeV central Au+Au collisions. A two-dimensional distribution, as seen in the right panel of Fig. 3.10, has a sum ( $x_\Sigma = x_1 + x_2$ ) and difference ( $x_\Delta = x_1 - x_2$ ) axis along the diagonals. The distributions along the sum axes in Fig. 3.11 are observed to be approximately constant within statistics. This is because in angular space the orientation of the overlapping nuclei arbitrarily changes each event which in turn changes the absolute position of tracks in  $\eta$  and  $\phi$ . This type of distribution, where the mean and variances does not depend on its absolute location, is referred to as stationary. When stationarity applies the distribution can be projected onto the difference axis without any loss of information, and now four dimensions  $(\eta_1, \eta_2), (\phi_1, \phi_2)$  can be reduced to two ( $\eta_\Delta = \eta_1 - \eta_2, \phi_\Delta = \phi_1 - \phi_2$ ). In practice the pairs are binned directly on the difference variables.

The finite  $\eta$  acceptance, however, introduces a structure to the distribution of pairs along  $\eta_\Delta$  as seen in Fig. 3.12. This “triangular acceptance effect” cancels in the ratio of sibling to mixed pairs in angular space but not in momentum space. A correction factor,  $w_\Delta$ , is applied to each pair binned in momentum space. The factor, essentially the inverse of the acceptance triangle, is

$$w_\Delta = \frac{1}{1 - |\eta_\Delta| / \eta_{\Delta, max}}, \quad (3.12)$$



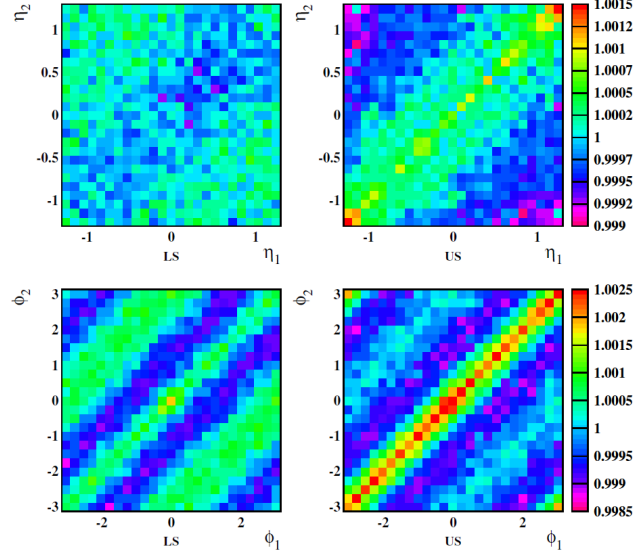


Figure 3.11: Two-particles correlations from 130 GeV central Au+Au collisions on  $(\eta_1, \eta_2)$  (upper) and  $(\phi_1, \phi_2)$  (bottom) and for like-sign (left) and unlike-sign (right) pairs [6].

where  $|\eta_\Delta| < \eta_{\Delta, max}$ .

### 3.4.1 Event Classes

Correlations measure relatively small differences in the distributions of sibling versus mixed pairs. In order to measure differences due to only physics, the mixed distribution needs to be constructed carefully with characteristics as similar as possible to the sibling distribution. This is accomplished through the formation of sub event classes.

The primary vertex position of the event along the z-axis, for example, changes the effective detector acceptance, primarily on  $\eta$ . An event with a primary vertex close to the edge of the TPC volume might contain fewer

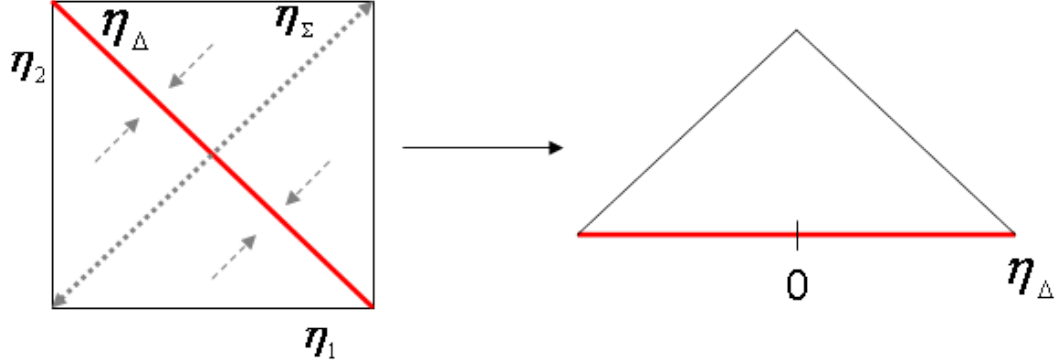


Figure 3.12: Projecting data onto the  $\eta_\Delta$  axis is equivalent to a rotation of the coordinate system by  $45^\circ$  (left panel). The new 1D distribution (right panel) is triangular due to the finite  $\eta$  acceptance.

tracks with large values of  $\eta_\Delta$ . However, if the vertex of the event used to make mixed pairs is also near the edge then the effects of the smaller acceptances will cancel.

Therefore, mixing events with large differences in the z-axis location of the vertices will have an effect on the correlation data at large values of  $\eta_\Delta$ . Reference [3] finds this effect is only noticeable in the three most central bins and can be removed by mixing events with a difference in the vertex positions that is less than 5 cm in the z-axis.

The difference in multiplicity between two events is also constrained in this analysis to ensure the sources of correlations are similar in both events. More importantly, this event ordering reduces the propagation of statistical errors from the single-particle distribution into the two-particle correlation space, otherwise significant “plaid” structures would appear [38]. The central-

ity fractions with a large range in multiplicity are sub-divided into multiplicity classes with  $\Delta N_{ch}$  less than approximately 50.

All the event classes are combined using a weighted average. The weight is the ratio of the number of sibling pairs in the event class integrated over the full  $2\pi\Delta\eta$  acceptance with respect to the total number of sibling pairs in all event classes.

$$\frac{\Delta\rho}{\sqrt{\rho_{ref}}} = \sqrt{\rho'_{ref}} \sum_{\Delta N_{ch}, \Delta z} \frac{N_{sib, \Delta N_{ch}, \Delta z}}{N_{sib, tot}} \times \frac{\Delta\rho}{\rho_{ref}}, \quad (3.13)$$

The pair density  $\rho_{ref}$  in the denominator of Eq. 3.13 needs to be formed from mixed pairs to cancel out experimental artifacts.

It is also essential to form  $\frac{\Delta\rho}{\rho}$  in each charge combination ( $++$ ,  $--$ ,  $+-$ ,  $-+$ ) separately, due to differences in the angular acceptance of positively and negatively charged particles corresponding to the magnetic field orientation. When forming a charge *independent* analysis all charge combinations are added together as written in Eq. 3.14. The  $\frac{1}{4}$  factor is an approximation of the ratio of the number of pairs in each charge combination to the total number of pairs and is used to transform the measure from a sum-of-ratios to a ratio-of-sums.

$$\left| \frac{\Delta\rho}{\sqrt{\rho_{ref}}} \right|_{CI} = \sqrt{\rho'_{ref, CI}} \times \frac{1}{4} \left( \frac{\Delta\rho}{\rho_{++}} + 2 * \frac{\Delta\rho}{\rho_{+-}} + \frac{\Delta\rho}{\rho_{--}} \right) \quad (3.14)$$

A like-sign (LS) correlation measure is formed by adding the  $++$  and  $--$  charge combinations together as seen in Eq. 3.15. An unlike-sign (US)

measure is formed from  $+-$  pairs. This analysis effectively counts both permutations of a pair so the  $+-$  distribution is equivalent to the  $-+$  distribution. Lastly, the difference in LS and US correlations can be measured in charge-dependent (CD) correlations.

$$\begin{aligned}
\left| \frac{\Delta\rho}{\sqrt{\rho_{ref}}} \right|_{LS} &= \sqrt{\frac{1}{2}\rho'_{ref,CI}} \times \frac{1}{2} \left( \frac{\Delta\rho}{\rho_{++}} + \frac{\Delta\rho}{\rho_{--}} \right) \\
\left| \frac{\Delta\rho}{\sqrt{\rho_{ref}}} \right|_{US} &= \sqrt{\frac{1}{2}\rho'_{ref,CI}} \times \frac{1}{2} \left( 2\frac{\Delta\rho}{\rho_{+-}} + \frac{\Delta\rho}{\rho_{--}} \right) \\
\left| \frac{\Delta\rho}{\sqrt{\rho_{ref}}} \right|_{CD} &= LS - US = \sqrt{\rho'_{ref,CI}} \times \frac{1}{4} \left( \frac{\Delta\rho}{\rho_{++}} - 2\frac{\Delta\rho}{\rho_{+-}} + \frac{\Delta\rho}{\rho_{--}} \right)
\end{aligned} \tag{3.15}$$

### 3.4.2 Reference Choice

The reference distribution,  $\rho_{ref}$ , should exclude the physics signal(s) of interest (e.g. jets, flows). Mixed pairs in an angular space create an accurate representation of  $\rho_{ref}$  because the physics signals are randomly distributed in the primary  $(\eta, \phi)$  space. Therefore mixed event pairs cannot produce statistically significant structures on  $(\eta_\Delta, \phi_\Delta)$  due to those processes.

However, because dynamical processes (e.g. jets) likely produce particles at similar transverse momentum in different collisions, mixed-event particle pairs on  $(p_{t1}, p_{t2})$  will have a similar structure as that from sibling pairs. Using  $\rho_{mix}$  as  $\rho_{ref}$  would result in a measurement of the *fluctuation* of the jet momentum distribution from an ensemble average.

Jet-related processes, the hypothesized signal of interest, is assumed to

follow binary scaling (linear superposition of nucleon-nucleon collisions). For momentum correlations, a  $\rho_{ref}$  is selected that is absent of such scaling and instead proportional to the number of nucleons interacting in the collisions ( $N_{part}$ ). The soft particle spectrum of the Kharzeev-Nardi two-component multiplicity production model [39] satisfies these conditions and is contained in the first term of Eq. 3.16. Equation 3.16 gives the differential multiplicity, where  $n_{pp}$  is the number of particles produced in a proton-proton collision per unit  $\eta$ .

$$\frac{dn}{d\eta} = (1-x)n_{pp}\frac{\langle N_{part} \rangle}{2} + xn_{pp}\langle N_{bin} \rangle = \frac{dn}{d\eta_{\text{soft}}} + \frac{dn}{d\eta_{\text{hard}}} \quad (3.16)$$

The fraction of the multiplicity due to “hard” processes is  $x$ , therefore, the fraction due to “soft” processes is  $(1-x)$ . The hard component is assumed to scale with the number of nucleon-nucleon collisions or binary collisions  $\langle N_{bin} \rangle$  and the soft component is assumed to scale with the number of nucleons interacting in the collision or participants  $\langle N_{part} \rangle$ .

The ratio of the number of participants to half the number of binary collisions,  $\frac{\langle N_{part} \rangle}{\langle N_{bin} \rangle/2}$ , is referred to as  $\nu$  and is also a measure of centrality. For example, in a single nucleon-nucleon collision  $\langle N_{bin} \rangle=1$  and  $\langle N_{part} \rangle=2$  while in a central Au+Au collision the number of binary collisions could exceed much more than half the number of participant nucleons. The variable  $\nu$  is essentially a measure of the path-length of an interacting nucleon as it propagates through the incident nucleus.

With the definition of  $\nu$ , Eq. 3.16 can be rewritten as,

$$\begin{aligned}\frac{2}{\langle N_{part} \rangle} \frac{dn}{d\eta} &= n_{pp} [(1-x) + x\nu] \\ &= n_{pp} [x(\nu - 1) + 1].\end{aligned}\tag{3.17}$$

The differential multiplicity divided by  $\langle N_{part} \rangle / 2$  is now linear as a function of  $\nu$  with a slope of  $x$ . This provides a method to measure the hard component fraction  $x$  from data. Figure 3.13 shows the linear dependence for pions and kaons (left panel) and protons (right panel). The relationship of these two variables for kaons and protons is approximately linear while the pions deviate from this expectation.

The  $p_t$  differential two-component model was reported in Ref. [40]. A generalized expression for this model is below and is similar to the first line of Eq. 3.17.

$$\frac{d^2 N_{ch}}{2\pi p_t dp_t d\eta} = \frac{n_{pp}}{2\pi \Delta\eta} \frac{N_{part}}{2} [(1-x)S_o(\nu, p_t) + x(\nu)\nu H_0(\nu, p_t)]\tag{3.18}$$

The shape of the soft component ( $S_0$ ) was determined from fits to p+p spectra in the  $y_t < 2$  region and found to be well described by a centrality independent Levy distribution [7]. The hard component ( $H_0$ ) is defined as the difference between the data and the Levy distribution and described with a Gaussian plus power-law tail on  $y_t$ .

In order to utilize the results for pions and protons reported in [7] the

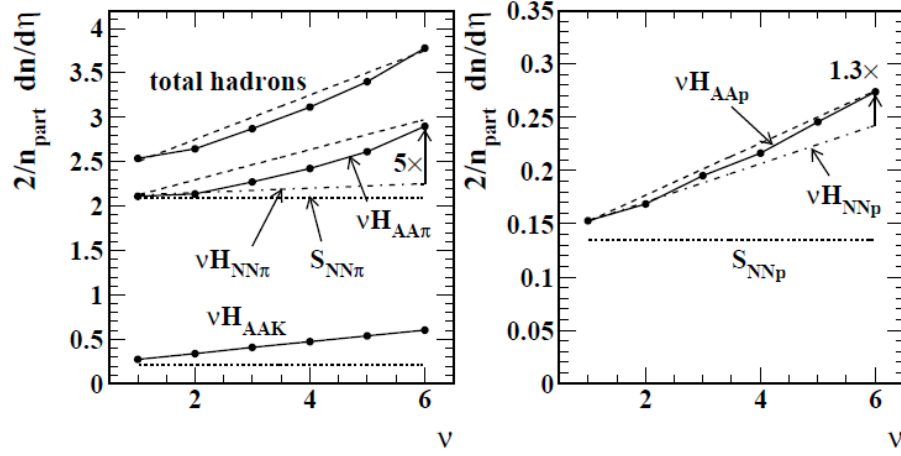


Figure 3.13: The differential multiplicity divided by  $\langle N_{part} \rangle / 2$  versus  $\nu$  for identified pions, kaons, and total hadrons (left panel) and protons (right panel) for 200 GeV p+p collisions and 5 Au+Au centralities. The data are represented by solid points and lines. The dotted line labeled “ $S_{NN}$ ” indicates the soft component. The dashed-dotted line labeled “ $\nu H_{NN}$ ” extrapolates the N-N collision value with binary scaling (no enhancement in heavy ion collisions). The soft component and the hard component ( $\nu H_{AA}$ ) sum to the data [7].

two-component model at a given value of  $\nu$  is given for identified particles

$$\begin{aligned}
 \frac{d^2 N_{ch}}{2\pi p_t dp_t d\eta}(\nu) &= \frac{n_{pp}}{2\pi\Delta\eta} \frac{N_{part}}{2} \{ f_\pi(\nu) [(1 - x_{\pi,\nu=1}) S_{o\pi}(\nu, p_t) + x_\pi(\nu) \nu H_{0\pi}(\nu, p_t)] \\
 &+ f_K(\nu) [(1 - x_{K,\nu=1}) S_{oK}(\nu, p_t) + x_K(\nu) \nu H_{0K}(\nu, p_t)] \\
 &+ f_p(\nu) [(1 - x_{p,\nu=1}) S_{op}(\nu, p_t) + x_p(\nu) \nu H_{0p}(\nu, p_t)] \}, \quad (3.19)
 \end{aligned}$$

where  $f(\nu)$  accounts for the relative yield of  $\pi$ , K, and p. The weights are normalized such that in the limit of  $\nu \rightarrow 0$ ,  $\sum_{\pi,K,p} f_k(\nu) = 1$ . The soft component is weighted with the factor  $(1 - x_{\nu=1})$  to ensure the correct normalization at centrality  $\nu = 1$  and to ensure that the possible increases in  $x(\nu)$  with centrality due to jet fragmentation evolution does not affect the soft component

amplitude.

The parameters for the pion and proton soft components were obtained from fits to efficiency corrected spectra in Ref. [7]. To form a reference for an inclusive analysis it was necessary to add the kaon component. The shape of the soft component  $S_{0,K}(p_t)$  was obtained from kaon spectra data from STAR [41] and PHENIX [42]. The particle densities were extrapolated to the  $\nu=0$  limit for each  $p_t$  value. The extrapolated data were then fit with a Levy distribution as in Eq. 3.20. The parameters of the Levy distribution were  $A=12.32$ ,  $T=0.1745$  GeV, and  $n=18.4$ .

Estimating the amplitudes of the kaon soft and hard components is more complicated due to the observed enhancement of kaon versus pion yields in heavy ion collisions [43]. The soft component used in the final results assumes all the enhancement in the kaons, unrelated to jets, is in the soft component. This requires an assumption that the jet-part of the kaon yield  $x_K(\nu)$  is equal to the jet-part of the pion yield  $x_\pi(\nu)$ .

The jet-part of the pion yield was estimated from the centrality dependence of charged pion spectra in 200 GeV Au+Au collisions [44] assuming a constant  $x$  and a unit normalized  $H_0$ . The value was estimated to be  $x_\pi(\nu = 1) = x_K(\nu = 1) = 0.114$ . For reference, this method differs from what is used in Ref. [7] where the hard component fraction  $x$  is given in the p+p limit and the ratio of the hard component in heavy ion collisions versus a single nucleon-nucleon collision ( $r_{AA} = H_{AA}/H_{NN}$ ) is responsible for the increase with  $\nu$ . Figure 3.13 demonstrates the large increase in the hard component



above binary scaling in heavy ion collisions. The value of  $x$  at  $\nu=1$  differs significantly from the linear slope of the data over the entire  $\nu$  range. The  $f(\nu)$  factor, which sets the relative fraction of kaons, is estimated from the ratio of kaon to pion yields and increases beyond  $N_{part}$  scaling due to strangeness enhancement.

The soft particle spectrum for pions, kaons, and protons used in this analysis can be concisely represented with a single Levy distribution

$$\frac{d^2 N_{ch,soft}}{dy_t d\eta} = 2\pi p_t m_{t,\pi} \frac{N_{part}}{2} \left[ \frac{A}{[1 + (m_{t,\pi} - m_{0,\pi}/(nT))^n]} \right], \quad (3.20)$$

where  $A=5.81$  c/GeV<sup>2</sup>,  $T = 0.169$  GeV, and  $n=13.8$ .

Mixed pairs are still required in momentum correlations for the cancellation of  $p_t$  dependent experimental acceptances. First, like in Eq. 3.13, a weighted average of the ratio  $\Delta\rho/\rho_{mix}$  is formed in each sub-event class. Then the denominator is effectively canceled with the factor  $\rho'_{tot}$ , an efficiency corrected charged particle distribution, and replaced with  $\rho'_{soft}$ , the efficiency corrected soft particle distribution. Lastly, the expression is multiplied by a  $\sqrt{\rho'_{soft}}$  prefactor which results in the final measure of the number of correlated pairs per soft particle.

$$\frac{\Delta\rho_{CI}}{\sqrt{\rho_{soft}}}(y_{t1}, y_{t2}) \equiv \sqrt{\rho'_{soft}} \frac{\rho'_{tot}}{\rho'_{soft}} \times \sum_{\Delta N_{ch}, \Delta z} \frac{N_{sib, \Delta N_{ch}, \Delta z}}{N_{sib, tot}} \times \frac{\Delta\rho}{\rho_{mix}} \quad (3.21)$$

The total number of reference pairs  $\rho'_{tot}$  was estimated from corrected spectra found in Ref. [41, 45]. First, the spectra was described by a Levy

distribution in the reported centralities. Then the parameters as a function of centrality were modeled with a power-law function. This provided a way to interpolate the values to the centralities used in this analysis.

### 3.4.3 Normalization

Normalization scales the number of mixed pairs relative to the number of sibling pairs. This is necessary because two events are, on average, mixed with each sibling event. There are several normalization choices that have corresponding advantages and disadvantages. Interestingly, all methods would yield the same results if the multiplicity bin width was equal to 1.

#### 3.4.3.1 Pair

Scaling the number of mixed pairs  $N_{mix}$  to the number of sibling pairs  $N_{sib}$  in the full  $2\pi\Delta\eta$  acceptance is known as total pair normalization. This rescaling is done precisely like in Eq. 3.22.

$$\frac{\Delta\rho}{\rho_{ref}} = \frac{\rho_{sib} - \frac{N_{sib}}{N_{mix}}\rho_{mix}}{\frac{N_{sib}}{N_{mix}}\rho_{mix}} \quad (3.22)$$

The average of  $\Delta\rho$  over the acceptance is then zero by construction. The constant offset in angular space with this normalization has no physical significance.

### 3.4.3.2 Event

Another method of normalization divides the number of mixed pairs by the total number of mixed events  $\epsilon_{mix}$ , where a mixed event is each occurrence that two events are mixed.

$$\frac{\Delta\rho}{\rho_{mix}} = \frac{\frac{1}{\epsilon_{sib}}\rho_{sib} - \frac{1}{2\epsilon_{mix}}\rho_{mix}}{\frac{1}{2\epsilon_{mix}}\rho_{mix}} \quad (3.23)$$

The factor of 2 in Eq. 3.23 is necessary to compensate for the fact that mixed events produce twice as many unique pairs as sibling events.

One advantage of using event normalization is that the momentum correlations can be related to measured values of non-statistical mean- $p_t$  fluctuations,  $\Delta\sigma_{p_t}^2$  [46].

$$\Delta\sigma_{p_t:n}^2 \equiv \sum_{j=1}^{\epsilon} n_j \left( \langle p_t \rangle_j - \hat{p}_t \right)^2 - \sigma_{\hat{p}_t}^2 \quad (3.24)$$

In Eq. 3.24  $n_j$  is the number of particles in event  $j$ ,  $\langle p_t \rangle_j$  is the mean transverse momentum for all accepted particles in event  $j$ ,  $\hat{p}_t$  is the inclusive mean  $p_t$  for all accepted particles in all events, and  $\sigma_{\hat{p}_t}^2$  is the inclusive  $p_t$  variance for all accepted particles in all events.

The fluctuation measure is related to the correlation measure through an integral in approximately the following way

$$\Delta\sigma_{p_t:n}^2 \cong (\bar{N} - 1) \hat{p}_t^2 \left\langle \frac{\Delta\rho}{\rho_{mix}} \right\rangle, \quad (3.25)$$

where the bracket represents a  $p_t$  weighed average.

However, correlation measurements also contain fluctuations due to the finite size of multiplicity event classes. This prevents making a direct comparison to mean- $p_t$  fluctuations.

### 3.4.3.3 Event with Bias Correction

The numerator,  $\Delta\rho$ , is designed to measure the total number of correlated pairs. However, with strictly event normalization,  $\Delta\rho$  may be non-vanishing even in the absence of correlations. This is due to the fact that for events in a finite multiplicity bin or for a fixed multiplicity ( $N$ ) the average number of sibling pairs  $\left(\overline{N(N-1)}\right)$  is not equal to the average number of mixed pairs  $\left(\overline{NN'}\right)$ . In  $(y_{t1}, y_{t2})$  correlation space this bias has a significant effect on the correlation structures.

To correct for this effect, a weighting factor  $\alpha$  is derived that will ensure  $\alpha\bar{\rho}_{sib}(y_{t1}, y_{t2}) = \bar{\rho}_{mix}(y_{t1}, y_{t2})$  in the absence of correlations. The event averaged sibling pair density  $\bar{\rho}_{sib}$  is guaranteed to be uncorrelated when it is equal to  $\overline{N(N-1)\hat{\rho}_{1,N}(y_{t1})\hat{\rho}_{1,N}(y_{t2})}$ , where  $\hat{\rho}_{1,N}(y_{t1})$  is the single particle density,  $\frac{1}{N}\frac{d^2N}{dy_t d\eta}$ . Similarly, the event averaged mixed pair density  $\bar{\rho}_{mix}$  is equal to  $\overline{N\hat{\rho}_{1,N}(y_{t1})N'\hat{\rho}_{1,N'}(y_{t2})}$ .

In the absence of correlations,  $\hat{\rho}_{sib}(y_{t1}, y_{t2}) = \hat{\rho}_{mix}(y_{t1}, y_{t2}) = \hat{\rho}_1(y_{t1})\hat{\rho}_1(y_{t2})$  but  $\Delta\rho \neq 0$  because  $N(N-1) \neq NN'$ . The weighting factor  $\alpha = \frac{\bar{\rho}_{mix}}{\bar{\rho}_{sib}}$  ensures  $\Delta\rho$  equals zero when there are no correlations and is defined as

$$\alpha(y_{t1}, y_{t2}) = \frac{\overline{N\rho_{1,N}(y_{t1})N'\rho_{1,N'}(y_{t2})}}{N(N-1)\hat{\rho}_{1,N}(y_{t1})\hat{\rho}_{1,N}(y_{t2})}, \quad (3.26)$$

where the overline indicates event averaging. The event average is calculated via  $\overline{X} = \sum_N f(N)X(N)/\sum_N f(N)$  where N sums over the multiplicity values in a bin and  $f(N)$  is the number of events with multiplicity N.

The bias correction factors  $\alpha$  were calculated for each multiplicity bin and implemented in the following manner,

$$\frac{\Delta\rho}{\rho_{mix}} = \frac{\alpha \frac{1}{\epsilon_{sib}}\rho_{sib} - \frac{1}{2\epsilon_{mix}}\rho_{mix}}{\frac{1}{2\epsilon_{mix}}\rho_{mix}}. \quad (3.27)$$

## Chapter 4

### Review of Correlations

The many diverse applications of correlations attest to its simple yet meaningful measure. The most common correlation measure, often referred to as Pearson’s correlation coefficient, is defined in Sec. 3.4. However, a close review of the publications during the late 19th century reveals that another scientist, Sir Francis Galton, created the idea of a correlation first [47].

Sir Francis Galton was a British biometrician and cousin of Charles Darwin, whose academic pursuits were wide-ranging and included the subjects of heredity and forensics [48]. An examination of the relationship between the length of the thigh bone with the length of other body parts or the height of the individual spurred the idea of correlation [47]. The first article he wrote mentioning the word correlation was titled “Co-relations and their measurements, chiefly from anthropometric data” and published in 1888 [47]. He later wrote a unique essay for the *North American Review* that detailed his discovery of this new statistical measure, correlation.

However, after a publication in 1895 by his student, Karl Pearson, the product-moment correlation would be from then on most commonly associated with Pearson, not Galton.

## 4.1 Fluctuations

Many aspects of the data obtained at RHIC were measured before focusing on the rich source of information contained in correlations. Critical fluctuations were one of the first proposed signatures of a phase transition to a quark gluon plasma [19]. Fluctuations are measured by the variance or width of a distribution.

A Gaussian is one of the most commonly used and observed distributions because of its ability, in certain limits, to describe unknown distributions. The central limit theorem states that the mean of a sample with large statistics from any random process will be distributed as a Gaussian. In fact, another one of Sir Francis Galton's accomplishments include the construction of the Quincunx computer which is a physical apparatus that illustrated the ideas of the central limit theorem. The computer was a tilted board with pegs evenly spaced so when a ball was dropped down the ball would randomly jump between the pegs and fall into boxes at the bottom. With a significantly large sample of balls the distribution of balls at the bottom would begin to form a Gaussian distribution.

The fluctuation measure that is relevant to the search for a new phase of matter is that which exceeds the expected fluctuations from purely statistical sources, which can occur even in mixed-event samples. Large variations in the *non*-statistical fluctuation measure with collision energy, projectile size, or centrality would indicate a critical point near the phase transition. The most recent hypothesized phase diagram of a theoretical quark gluon plasma is seen

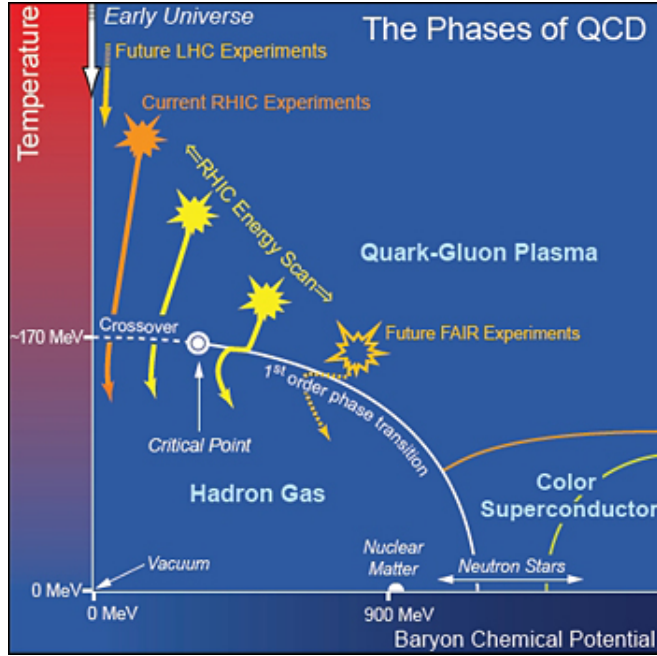


Figure 4.1: The hypothesized Quark Gluon Plasma phase diagram from QCD predictions [8]. The white solid lines show the phase boundaries and the white circle indicates the critical points. The nuclear overlap of current Au+Au collisions are marked with an orange star.

in Fig. 4.1 with the critical point indicated by a white circle.

If heavy ion collisions were fully equilibrated at a constant “temperature” no excess fluctuation would be expected. Therefore a measure of non-statistical fluctuation could indicate systems in at least two scenarios: the collision systems do not reach complete equilibrium or the systems do reach equilibrium but each event fluctuates in temperature.

In Ref. [46] the non-statistical  $\langle p_t \rangle$  fluctuation measure for Au+Au collisions at  $\sqrt{s_{NN}} = 130$  GeV was reported. An excess fluctuation in charge-



independent  $\langle p_t \rangle$  data was measured but no evidence of critical fluctuations to indicate a phase transition was found. This could indicate either the systems do not reach equilibrium or if in equilibrium, the  $\langle p_t \rangle$  fluctuates from event to event. In either case the absence of critical fluctuations implies the system was not observed near a phase transition.

More details about this excess fluctuation can be extracted through a study of the scale dependence ( $\delta x$ ). The scale dependence refers to the bin size for which fluctuations are calculated. The bin size can range from the entire TPC acceptance to a very small bin in  $(\eta, \phi)$ . The scale dependence of fluctuations in  $\langle p_t \rangle$  for Au+Au 200 GeV collisions is shown in the left panel of Fig. 4.2. There is an indication of structure to the fluctuation measurements but it is not readily interpretable. Fortunately, more information is available through a correlation measure which is related to a fluctuation simply through an integral.

Fluctuations are related to two-particle correlations by the Fredholm integral equation [9].

$$\Delta\sigma^2(\delta\eta, \delta\phi) \equiv 4 \sum_{i,j} \epsilon_\eta \epsilon_\phi K_{ij} \frac{\Delta\rho}{\sqrt{\rho_{ref}}} (i\epsilon_\eta, j\epsilon_\phi) \quad (4.1)$$

In Eq. 4.1  $(\delta\eta, \delta\phi)$  is the length (scale) of the fluctuation and  $(\epsilon_\eta, \epsilon_\phi)$  is the 2D bin-size of the measured correlations. Generally  $\epsilon_x \leq \delta x \leq \Delta x$  where  $\Delta x$  is the detector acceptance. The kernel  $K_{ij}$  is necessary for integration over the correlation bins which have indices  $i$  and  $j$ .

The level of detail gained in a correlation measure is evident in the

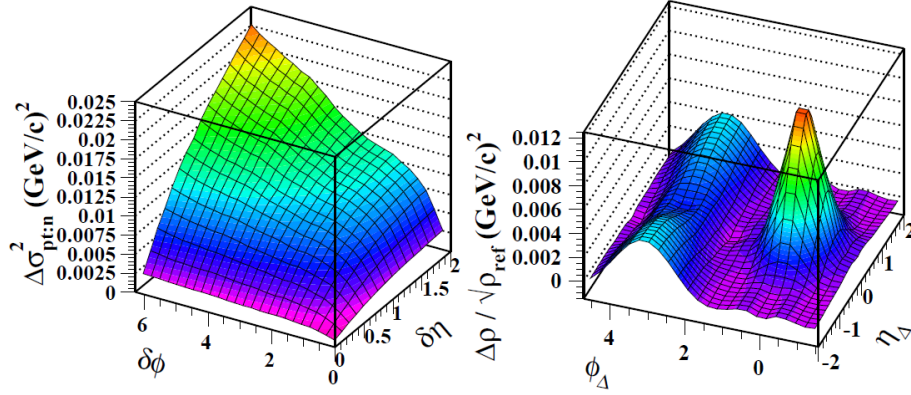


Figure 4.2: The mean- $p_t$  non-statistical fluctuation measure  $\Delta\sigma_{pt}^2$  (left) and two-particle correlations (right) of 0-15% central HIJING events with quenching off [9].

right panel of Fig. 4.2. The usefulness of fluctuations are now surpassed by the advantages of direct correlation measurements, which is the focus of this dissertation.

## 4.2 Proton-proton Correlations

In order to observe new physics, such as the formation of a quark gluon plasma, the correlation structures need to be carefully studied for differences with respect to a control system. This control or reference needs to be as similar as possible to a heavy ion collision but without the possibility of a quark gluon plasma. Proton-proton collisions are good candidates for this reference.

The first proton-proton collisions were made at the Intersecting Storage Rings (ISR) at CERN in 1971. Since then, other accelerators such as the

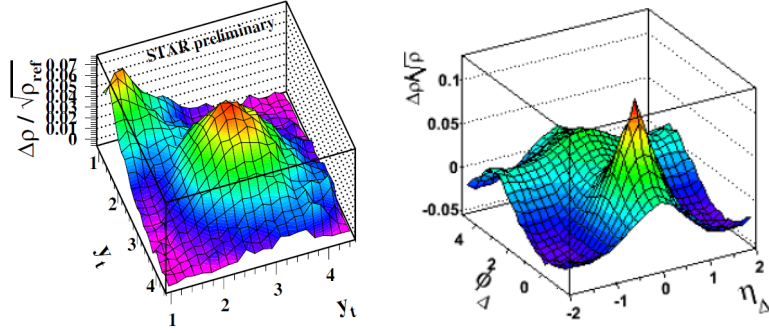


Figure 4.3: 200 GeV Proton-proton collisions at STAR in momentum [10] and angular [3] space.

SPS, Tevatron, RHIC, and the LHC have collided two counter-rotating beams of protons. The many years of published research and development of sophisticated event simulators provide a strong basis to understand and interpret correlation structures observed in proton-proton collisions.

PYTHIA is one of the most successful models of proton-proton collisions [49]. PYTHIA models the low-momentum (“soft”) processes via the hadronization of interacting color fields or “strings” [50]. Hard processes are modeled by pQCD jet fragmentation, which will be described in more detail in Sec. 4.3.

Two-particle correlations of 200 GeV proton-proton collisions at STAR are presented in Fig. 4.3. To aid in the description of the many sources of correlated particles in p+p collisions a naive  $y_t$  cut will be made to distinguish “soft” and “hard” pairs. This is naive because two-component (“soft” and “hard”) studies have shown that there is no simple separation point in momentum of the two components [7]. However, it suits our purely educational

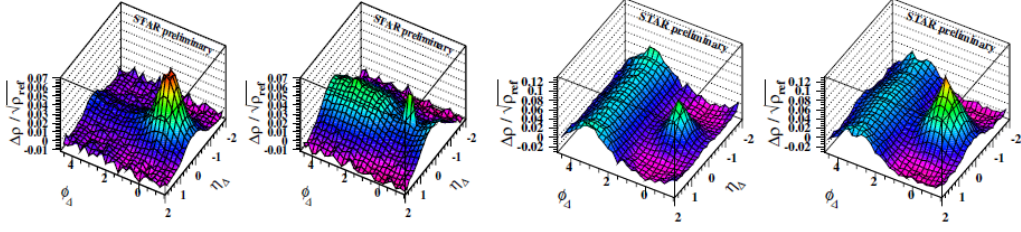


Figure 4.4: The left two panels contain soft pairs defined as  $(y_t < 2)$  ( $p_t = 0.5$  GeV/ $c$ ) for both particles in a pair. The right two panels contain hard pairs ( $y_t > 2$ ). The first and third panels are for like-sign pairs and the second and fourth panels are for unlike-sign pairs [10].

purposes. This  $y_t$  cut is motivated from the data shown in the left frame of Fig. 4.3. The broad peak around  $(y_{t1}, y_{t2}) = (3, 3)$  is separated with a  $y_t > 2$  ( $p_t = 0.5$  GeV/ $c$ ) cut for both particles in a pair and the structure around the lower momentum corner is separated by requiring the  $y_t$  of both particles to be less than 2. Fig. 4.4 contain angular correlation data in four combinations of soft, hard, like-sign, and unlike-sign pairs for 200 GeV proton-proton collisions.

The left panel in Fig. 4.4 are correlations of like-sign, soft pairs and the clearest signal from the Hanbury-Brown and Twiss (HBT) effect can be observed in this panel. HBT describes correlations due to quantum coherence from an incoherent, finite size source of identical bosons with a small difference in relative velocity [51]. Since HBT occurs only amongst identical particles we expect to see a signal in like-sign correlations. Also, the particles correlated from HBT are close together in angular space so the signal is seen around the origin,  $(\eta_\Delta, \phi_\Delta) = (0, 0)$ .

The unlike-sign, soft pair correlation data in the second panel show most clearly a broad ridge along the entire range of  $\phi_\Delta$  centered at  $\eta_\Delta = 0$ . The Lund string fragmentation model, used in PYTHIA, can predict this structure. The Lund model simulates the interactions between a separating quark anti-quark pair via a one-dimensional color flux tube known as a “string”. The potential energy increases as the string is stretched. When it becomes energetically favorable the string breaks and produces a new quark anti-quark pair. This process is repeated until only a stable hadron remains [49]. The correlated pairs are observed in both unlike- and like-sign pairs and are generally close together in  $\eta$ . While they also appear to be located at all values of  $\phi_\Delta$ , the correlation structure is more enhanced in the  $\phi_\Delta \approx \pi$  region of the US data as evident in the second panel of Fig. 4.4.

A narrow spike at the origin is also observed in the unlike-sign, soft pairs. The probable source of these correlated pairs is  $e^+e^-$  pair production from photon interactions with detector material. This process will be described in more detail in Sec. 5.5.3. The main characteristics of these correlated pairs are that they are opposite in charge, generally distributed in a lower momentum region, and close in angular space. This results in a narrow spike in the unlike-sign, soft data.

The prominent source of correlated particles in the two right panels of Fig. 4.4 (“hard” pairs) is jet fragmentation. Jets are defined experimentally as collimated sprays of particles from high momentum scattering. Following conservation of momentum, two back-to-back jets are usually observed and are

known as “dijets”. In correlation space, this creates pairs of particle produced in one of the jets with a small relative difference in both  $\eta$  and  $\phi$ . This “intrajet” correlation gives rise to the peak around the origin in the right panels of Fig. 4.4. The region of the 2D correlation space in which  $\phi_\Delta < \pi$  is referred to as the “same-side”. So a model independent way of referring to this observed correlation structure is the “same-side” peak.

Pairs are also formed with a particle from each side of the di-jet forming what is known as “interjet” correlations. These particles are generally separated by  $180^\circ$  which creates the signal around  $\phi_\Delta \approx \pi$ . The long ridge along  $\eta_\Delta$  is due to the fact that the center of mass of the parton-parton interactions is broadly distributed in  $\eta$ .

In summary, selecting pairs from the broad peak around  $(y_{t1}, y_{t2}) = (3, 3)$  shows evidence of jet correlations. Selecting pairs from the lower momentum corner ( $y_t$  of both particles less than 2) shows evidence of HBT, photon conversion, and soft string fragmentation.

#### 4.2.1 Proton-proton Fit Model

Correlation data from pairs with all charges and momentum values contain the superposition of the correlation structures described above. A two dimensional fit model allows the information about each individual structure to be isolated and quantified. The fit model required to fit proton-proton data consists of five components. A 2D exponential centered around  $(\eta_\Delta, \phi_\Delta) = (0, 0)$  describes the contributions from HBT and electron pairs. A 1D Gaussian

along  $\eta_\Delta = 0$  fits the longitudinal string fragmentation. A  $\cos(\phi_\Delta)$  (dipole) term is used to describe the ridge along  $\phi_\Delta \approx \pi$ . This term along with any future sinusoidal components are referred to with the terminology of a series expansions into multiple moments (dipole, quadrupole, sextupole, ...). A 2D Gaussian describes the same-side peak attributed to jets. Lastly there is a constant offset which is highly dependent on the procedures used to normalize the number of mixed pairs to the number of sibling pairs and has no physical significance.

### 4.3 Jets

Perturbative QCD (pQCD) is a successful theory describing jet production or high momentum transfer processes [16]. Past successes motivate the attempt to determine to what extent RHIC data can be described with pQCD. This section will provide details about jets in a pQCD description using the event generator HIJING and the book “An Introduction to Quantum Field Theory” by Peskin as a reference [52, 53].

HIJING is a Monte Carlo model for multiple jet production in p+p, p+A, and A+A collisions [53]. The derivation of the differential jet cross section reported in [53] will begin with a simpler expression of the total cross section of two-body to two-body processes as seen in Eq. 4.2. The hadron level scattering will be described as  $(A) + (B) \rightarrow (C) + (D)$  and the parton level

scattering will be described as  $(1) + (2) \rightarrow (3) + (4)$  in the following expression

$$\sigma_{jet}(A + B \rightarrow C + D) = \int_0^1 dx_1 \int_0^1 dx_2 \sum_{a,b} f_a(x_1) f_b(x_2) \sigma^{ab}(1 + 2 \rightarrow 3 + 4), \quad (4.2)$$

where  $\sigma^{ab}$  is the pQCD cross section for parton species a and b. Feynman  $x$  is the ratio of the longitudinal momentum carried by the parton to the total longitudinal momentum carried by the parent hadron. In the center of mass frame of the scattered partons  $\vec{p} = x_1 \vec{p}_A + x_2 \vec{p}_B$  where  $p$  is the four-momentum vector of the partons  $\vec{p} = (E, p_x, p_y, p_z)$ . The structure function,  $f(x)$ , is the parton's longitudinal momentum distribution also known as the parton distribution function. In HIJING, the Duke-Owens structure functions give the values of  $f(x)$  [54].

Next, the differential cross section is formed and the pQCD cross section is expressed as a function of the Mandelstam variable  $\hat{t}$ , which is related to the scattering angle in the center of mass frame. The differential cross section is

$$\frac{d^3\sigma_{jet}}{dx_1 dx_2 d\hat{t}}(A + B \rightarrow C + D) = \sum_{a,b} f_a(x_1) f_b(x_2) \frac{d\sigma}{d\hat{t}}(1 + 2 \rightarrow 3 + 4). \quad (4.3)$$

Cross sections of scatterings are often expressed in terms of the Lorentz-invariant Mandelstam variables,  $u$ ,  $t$ , and  $s$ . They help reduce the 4 four-momentum vectors for the two incoming and two outgoing particles into just three variables (plus the masses). These kinematic variables also correspond to the four-momentum of the exchanged particles in the three fundamental Feynman diagrams in Fig. 4.5.



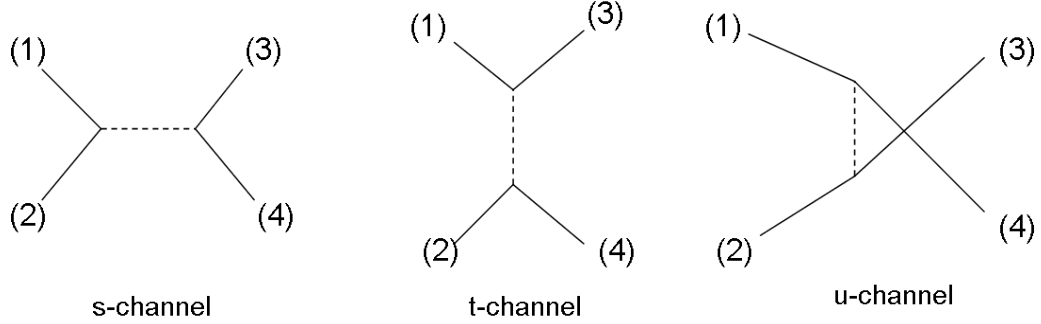


Figure 4.5: Feynman diagrams of two-body processes. The u, t, and s-channel correspond to the Mandelstam variables which describe the four-momentum of the exchanged particle.

The mathematical definitions of the Mandelstam variables are found in Eq. 4.4 where  $s$  is the total center of mass energy and  $t$  and  $u$  are the four-momentum transfer in the corresponding exchange channel.

$$\begin{aligned}
 \hat{s} &= (p_1 + p_2)^2 \\
 \hat{t} &= (p_1 - p_3)^2 \\
 \hat{u} &= (p_1 - p_4)^2 \\
 s + t + u &= m_1^2 + m_2^2 + m_3^2 + m_4^2
 \end{aligned}
 \tag{4.4}$$

The left hand side of Eq. 4.3 needs to be re-expressed with observable variables. The Feynman  $x$  and  $\hat{t}$  can be related to the rapidities and  $p_t$  of the partons. The variable transformation is done through the Jacobian,  $\delta(x_1, x_2, \hat{t})/\delta(y_1, y_2, p_t) = 2p_t\hat{s}/s$ .

$$\frac{d^3\sigma_{jet}}{dy_1 dy_2 dp_t} (A + B \rightarrow C + D) = \sum_{a,b} f_a(x_1) f_b(x_2) \frac{2p_t \hat{s}}{s} \frac{d\sigma^{ab}}{d\hat{t}} (1 + 2 \rightarrow 3 + 4) \quad (4.5)$$

The equation is further manipulated with the relation  $\hat{s} = x_1 x_2 s$  and  $dp_t^2 = p_t dp_t d\phi$ . The azimuthal acceptance is assumed to be  $2\pi$ . The final expression is in Eq. 4.6. The constant K is approximately 2 to correct the lowest order pQCD rates for next to leading order effects.

$$\frac{d\sigma_{jet}}{dp_t^2 dy_1 dy_2} = K \sum_{a,b} x_1 f_a(x_a, dp_T^2) x_2 f_b(x_2, dp_T^2) \frac{d\sigma^{ab}(\hat{s}, \hat{t}, \hat{u})}{d\hat{t}} \quad (4.6)$$

HIJING uses Eq. 4.6 for the jet cross sections. This cross section is for only two-body to two-body processes leading to final states consisting of two jets with equal and opposite transverse momentum. The transverse momentum scales are on the order of  $p_t > 2 \text{ GeV}/c$ .

The  $x_1$  and  $x_2$  variables in the right hand side of Eq. 4.6 still need to be expressed as the rapidities of the scattered partons. Through algebraic manipulation the Feynman  $x$  can be shown to be related to the rapidities in the following way,

$$\begin{aligned} x_1 &= \frac{2p_t}{\sqrt{s}} (e^{y_3} + e^{y_4}) \\ x_2 &= \frac{2p_t}{\sqrt{s}} (e^{-y_3} + e^{-y_4}) . \end{aligned} \quad (4.7)$$

The pQCD cross sections,  $\sigma^{ab}$ , found in Eq. 4.6 can be derived from the following general expression of a cross section as a function of the solid angle  $\Omega$ ,

$$\left(\frac{d\sigma}{d\Omega}\right)_{CM} = \frac{1}{2E_A 2E_B |v_A - v_B|} \frac{|\vec{p}_1|}{(2\pi)^2 4E_{CM}} |M(p_A, p_B \rightarrow p_1, p_2)|^2, \quad (4.8)$$

where  $E_A = \sqrt{p_A^2 + m_A^2}$  is the energy of the scattering particle A (similarly for  $E_B$ ),  $|v_A - v_B|$  is the relative velocity of the particles,  $E_{CM}$  is the total initial energy, and  $|p_1|$  is the absolute value of the momentum of either of the final particles ( $p_2 = -p_1$ ).

The matrix element  $|M|^2$  for scattering processes can be determined from the Feynman rules for tree-level diagrams. The cross section of  $q_i \bar{q}_i \rightarrow q_j \bar{q}_j$ , for example, is

$$\frac{d\sigma}{d\hat{t}} = \frac{4\pi\alpha^2}{9\hat{s}^2} \left( \frac{\hat{t}^2 + \hat{u}^2}{\hat{s}^2} \right). \quad (4.9)$$

The Mandelstam variables are also related to the rapidities of the scattered partons.

$$\begin{aligned} s &= \frac{E^2 - (p_t^2 + p_z^2)}{x_1 x_2} \\ t &= -p_t^2 [1 + e^{(y_4 - y_3)}] \\ u &= -p_t^2 [1 + e^{(y_3 - y_4)}] \end{aligned} \quad (4.10)$$

In summary, this section has derived the expression for the jet differential cross section used by HIJING (Eq. 4.6). The components of this cross

section have also been given as functions of observed variables ( $y, p_t$ ).

### 4.3.1 Minijets

Applying pQCD theory to lower momentum jets was first attempted at the UA1 experiment at the proton-antiproton collider SPS at CERN. These jets with a very low  $p_t$  threshold are referred to as minimum-bias jets or “mini-jets”. The abstract of Ref. [55] states “a theoretical cutoff of  $p_t^{min} \approx 3$  GeV seems to describe the observed total minijet cross section with  $E_{t,jet} \geq 5$  GeV.” The  $p_t^{min}$  is the parton minimum transverse momentum and  $E_t^{jet}$  is the total energy of the jet. This paper also purports that jets at this low  $p_t$  range should be dominated by gluons.

The remarkable result that pQCD can describe jet cross sections over many orders of magnitude is very significant to the formation of analysis techniques of heavy ion data. Conventional heavy ion analyses assume the contribution of jet physics to be small at low momentum due to the strongly coupled medium. This assumption prevents a significant effort in the heavy ion community to use pQCD before abandoning it in favor of other explanations.

## 4.4 Heavy Ion Correlations

After a thorough study of proton-proton data the investigation can continue into the new territory of heavy ion collisions. Reference [11] presents minimum bias angular correlation results for Au+Au 62 and 200 GeV collisions at STAR in eleven centralities. This paper undergoes the same analysis

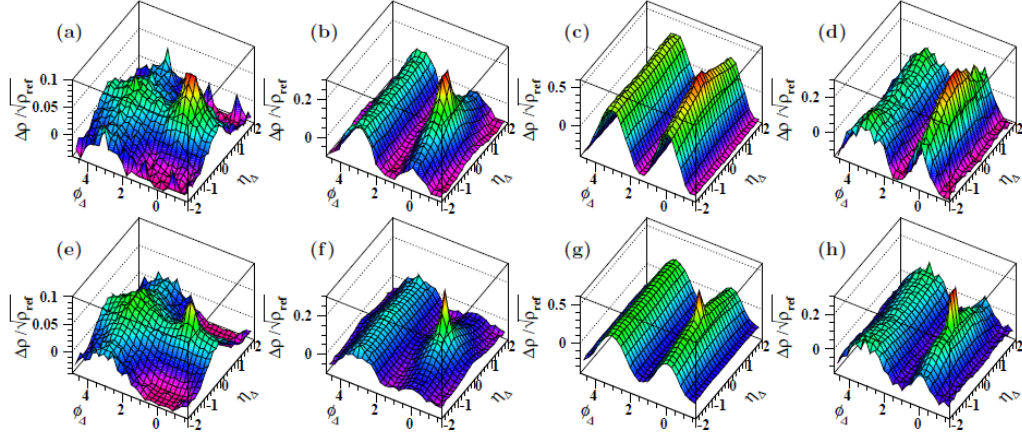


Figure 4.6: Two-particle angular correlations for Au+Au collisions at  $\sqrt{s_{NN}}=200$  and 62 GeV (upper and lower rows respectively). Centrality increases left-to-right from most-peripheral to most-central [11].

techniques described in Chapter 3. The most peripheral Au+Au centrality looks very similar to proton-proton collisions, as expected, but with increasing centrality the correlation landscape begins to change noticeably as seen in Fig. 4.6.

In fact, the five components of the 2D fit model in Sec. 4.2.1 are no longer sufficient to completely describe the data. A new structure is observed in the residual which can be modeled with a quadrupole ( $\cos(2\phi_\Delta)$ ) term.

The fit function in the paper is then defined as

$$\begin{aligned}
F = & A_1 \exp \left\{ -\frac{1}{2} \left[ \left( \frac{\phi_\Delta}{\sigma_{\phi_\Delta}} \right)^2 + \left( \frac{\eta_\Delta}{\sigma_{\eta_\Delta}} \right)^2 \right] \right\} \\
& + A_D \cos(\phi_\Delta - \pi) \\
& + A_Q \cos(2\phi_\Delta) + A_0 \exp \left\{ -\frac{1}{2} \left( \frac{\eta_\Delta}{\sigma_0} \right)^2 \right\} \\
& + A_2 \exp \left\{ - \left[ \left( \frac{\phi_\Delta}{w_{\phi_\Delta}} \right)^2 + \left( \frac{\eta_\Delta}{w_{\eta_\Delta}} \right)^2 \right]^{1/2} \right\} + A_3. \quad (4.11)
\end{aligned}$$

The complete fit results are shown in Fig. 4.7 and an example fit decomposition is shown in Fig. 4.8. In the four most-peripheral centralities a steady increase in the amplitude and widths of the 2D Gaussian is observed. It increases at the same rate expected for a superposition of individual nucleon-nucleon collisions known as binary scaling. Generating events with HIJING (“jet quenching” option off) reproduces these trends as well. Interestingly, at the 46-55% centrality there is a dramatic increase in the fit parameters, which was referred to as the “sharp transition” in Ref. [11]. The maximum amplitude of the quadrupole is observed in the mid-central bins while the minimum amplitude is 0 at the most peripheral and the most central.

The results from Ref. [11] are unique since they are obtained with a theory-independent fit model over the  $p_t$  integrated 2D  $(\eta_\Delta, \phi_\Delta)$  space. A strong increase in the amplitude of the same-side peak and away-side ( $\phi_\Delta \approx \pi$ ) dipole do not support an opaque, strongly interacting medium if the minijet hypothesis is valid [11].

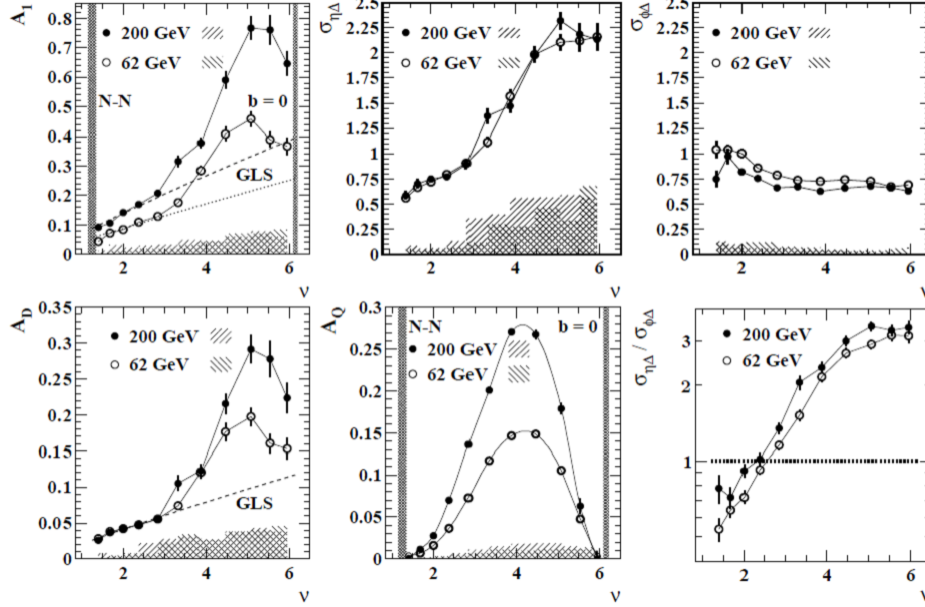


Figure 4.7: Fit parameters versus centrality reported in [11] for Au+Au collisions at  $\sqrt{s_{NN}} = 200$  GeV (solid symbols) and 62 GeV (open symbols). The 2D Gaussian amplitude and widths are shown in the upper panels. The amplitude of the dipole and quadrupole and shown in the bottom left and middle panel respectively. The bottom right panel shows the width aspect ratio,  $\sigma_{\eta/\Delta} / \sigma_{\phi/\Delta}$ , of the 2D Gaussian. The error bars represent fitting errors. The dotted line labeled “GLS” indicates the prediction from Glauber linear superposition. The hatched regions indicate the systematic uncertainties.

#### 4.4.1 Quadrupole

The quadrupole structure observed in the correlation data is conventionally assumed to be a result of an anisotropy in the single-particle density on azimuth. Much attention in the heavy ion community has been focused on theoretical predictions and measurements of this observed anisotropy.

The azimuthal anisotropy is interpreted by most in the heavy ion field

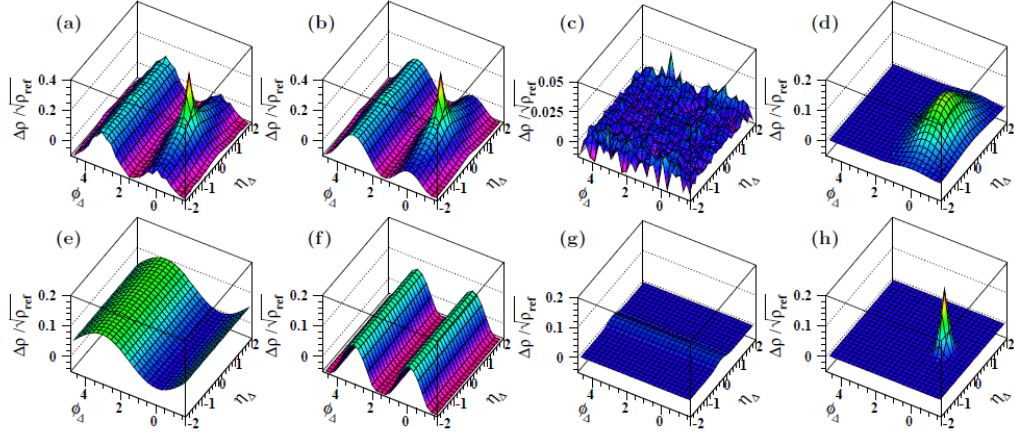


Figure 4.8: The fit decomposition of 46-55% centrality data for 62 GeV Au+Au collisions [11]. The data, fit, and residual are shown in the upper left plots. The upper right plot shows the 2D Gaussian component. The lower panels show the dipole, quadrupole, 1D Gaussian, and the 2D exponential.

as a signature of a strongly interacting system. According to the conventional hydrodynamic interpretation, the nuclear overlap of a non-central collision creates a spatial anisotropy (almond shape) which, with a pressure gradient built up by a strongly interacting medium, evolves into a momentum anisotropy of the final state particles. The particles flow preferentially in the direction of the reaction plane defined by the beam axis and the impact parameter, where the pressure gradient is the largest. With this collective behavior description the azimuthal anisotropy is often referred to as elliptic flow. Measurements of elliptic flow were first reported at RHIC energies in 2001 for 22k Au+Au collisions at 130 GeV in Ref. [12].

According to hydrodynamic models, elliptic flow measurements provide insights to the early stage of the system evolution. This is because the pres-



sure driven gradient quickly self quenches as the elliptical shape approaches a spherical shape. Thus the anisotropy was created in the early stage of the system.

Reference [12] reports that the anisotropy is 6% for peripheral collisions and decreases for more central collisions. This measurement, on a 1D projection of the data on  $\phi$ , was made by correlating each particle with the event plane  $\Psi$  and averaging over all events ( $\langle \cos[2(\phi - \Psi_2)] \rangle$ ). The event plane is used as an estimation of the reaction plane, which cannot be measured. This “event plane” method is statistically equivalent to the two-particle correlation analysis discussed in this dissertation. In the hydrodynamic picture, “non-flow” effects, such as jets, were thought to be small enough to fit within the error bars based on HIJING studies.

The analysis technique in Ref. [12] is standard in the field but many of its limitations can be easily removed with a 2D two-particle correlation analysis technique. First, a 2D correlation measurement does not need to estimate an event plane which is prone to biases and errors. Also, contamination of correlations from jets or “non-flow” are easily removed by taking into account the  $\eta_\Delta$  dependence.

The low level of non-flow contamination claimed in 1D analyses was challenged by the 2D two-particle correlation study in Ref. [13]. The 2D two-particle correlation measurements of the quadrupole component,  $v_2\{2D\}(p_t)$ , are reported to be systematically lower than the values previously reported by “event-plane” methods,  $v_2\{EP\}(p_t)$ , as seen in Fig. 4.9. This is argued to

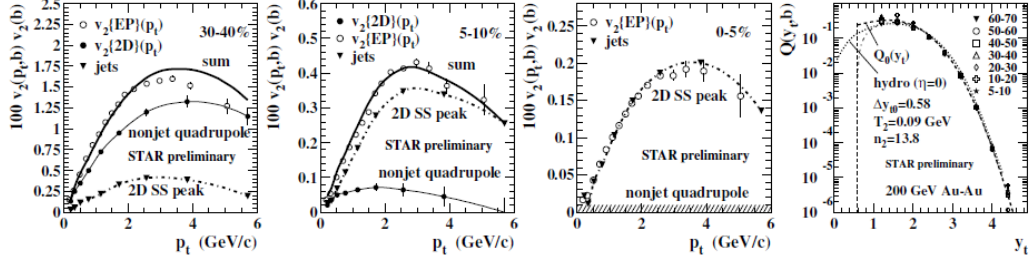


Figure 4.9: The first three panels show  $v_2$  and jet measurements as a function of  $p_t$  in centralities 30-40%, 5-10%, and 0-5% for Au+Au 200 GeV data [12]. The right panel shows the quadrupole spectrum as a function of  $y_t$  with a fit  $Q_o(y_t)$ .

be because the 2D fit utilizes the  $\eta_\Delta$  dependence of the jet component (2D Gaussian) to completely separate jet correlations and the azimuthal anisotropy.

Two implications of the analysis in Ref. [13] disagree with a hydrodynamical picture. First, the most central collisions show no  $v_2\{2D\}(p_t)$  amplitude. This contradicts the idea that even the most central collisions should have a non-zero  $v_2$  due to small fluctuations of nuclear overlap from a perfectly centered collision. Also, the  $v_2$  data in [13] are described with a “fixed transverse boost and universal Levy form nearly independent with centrality” which does not agree with a hydrodynamic flow interpretation.

#### 4.4.2 The $\eta_\Delta$ Elongated 2D Gaussian

Features of the same-side peak also dramatically change with an increase in centrality. In proton-proton collisions the same-side peak can be attributed to minijets and is accurately modeled with a 2D Gaussian. However, beginning in the 46-55% Au+Au centrality fraction the width ( $\sigma_{\eta_\Delta}$ ) of

the Gaussian dramatically increases and extends past the TPC acceptance.

Is this broadening a signature of new physics such as flow in heavy ion collisions, a modification to jet fragmentation in the dense heavy ion environment or some other novel QCD phenomenon?

Reference [20] analyzes the properties of this new broadening, known as the “ridge”, in central Au+Au collisions. The analysis labels the  $0.7 < |\eta_\Delta| < 1.4$  regions as the “ridge” and the  $|\eta_\Delta| < 0.7$  region as the “jet”. A momentum cut on the pairs is imposed which requires a trigger particle to have a  $p_t$  between 3 and 4 GeV/ $c$  and all associated particles to have a  $p_t$  greater than 2 GeV/ $c$ . The properties of the correlations are studied after subtracting an assumed value for “elliptic flow” ( $v_2$ ).

The jet region around the origin is observed to be similar to the jet peak in proton-proton data while the jet+ridge component differs. It was concluded that the ridge had properties consistent with a medium. However, the ridge yield increases up to the highest  $p_t$  value (9 GeV/ $c$ ) which suggests “the ridge is associated with jet production” [20].

A counterpoint to the conclusions of this analysis is that the properties of the “ridge” measured in [20] contain a significant contribution from the underlying event. All of the particles in the ridge region ( $0.7 < |\eta_\Delta| < 1.4$ ) are not necessarily contributing to the correlation structure. In Chapter 6 the momentum distribution of pairs correlated in only the elongated structure will be presented.

#### 4.4.2.1 Sextupole

A recent development revolutionized the field’s approach to measuring azimuthal anisotropy. Previously the belief was that collective flow generated only even-order moments of azimuthal anisotropy ( $v_2, v_4, \dots$ ). New hydrodynamical calculations showed that event-wise fluctuations in the density of the colliding nuclei could produce a  $v_3$  component to the particle correlations [56].

However, attributing the amplitude of  $v_3$  as a measurement of flow is an important topic of debate and highly dependent on the chosen fit model. In Ref. [11] it is determined that the only source of a  $v_3 = \langle \cos(3\phi) \rangle$  in central Au+Au data is the  $\eta$  elongation of the same-side peak. An important point to make is that there are many choices to describe the same-side peak: an asymmetric 2D Gaussian; a 2D Gaussian plus sextupole; a 2D Gaussian plus a 1D Gaussian on  $\phi_\Delta$ , constant along  $\eta_\Delta$ ; or a 2D peaked non-Gaussian function. All of these describe the same signal in the data. Assigning a physical interpretation based on the somewhat arbitrary choice of the statistical fit model is misleading.

In addition, the fact that sextupole measurements are conventionally made with 1D  $\phi$  projections makes them very sensitive to “non-flow” (i.e. jets). This often necessitates assumptions about non-flow such as the  $\eta_\Delta$  and  $p_t$  dependencies, which cast doubt on the physical interpretation of the measurements.

## Chapter 5

### Transverse momentum correlations

Two-dimensional (2D) transverse momentum correlations complete the measurements of the six dimensional correlation space  $(\eta_1, \phi_1, p_{t1}, \eta_2, \phi_2, p_{t2})$ . They provide another observable in which theoretical models can be compared. This chapter presents the latest measurements of minimum bias  $(y_t, y_t)$  correlations and comparisons to several theoretical models.

#### 5.1 Charge Independent Results

Figure 5.1 contains 200 GeV Au+Au charge independent (CI) correlations  $\Delta\rho/\sqrt{\rho_{soft}}(y_{t1}, y_{t2})$  in 11 centralities. These momentum correlations are for all charged particles with  $p_t > 0.15$  GeV/ $c$ ,  $|\eta| < 1$ , and full azimuth. The reference distribution  $\rho_{soft}$ , described in Sec. 3.4.2, is absent of binary scaling in order to emphasize our correlation signals of interest (e.g. jets). The number of mixed pairs is normalized using event normalization with a bin width bias correction factor, to retain a possible connection to a non-statistical mean- $p_t$  fluctuation measure described in Sec. 3.4.3.3.

The main feature in all centralities is a bump peaked near  $(y_{t1}, y_{t2}) = (3, 3)$  ( $p_t=1.4$  GeV/ $c$ ). The amplitude of the bump increases with central-

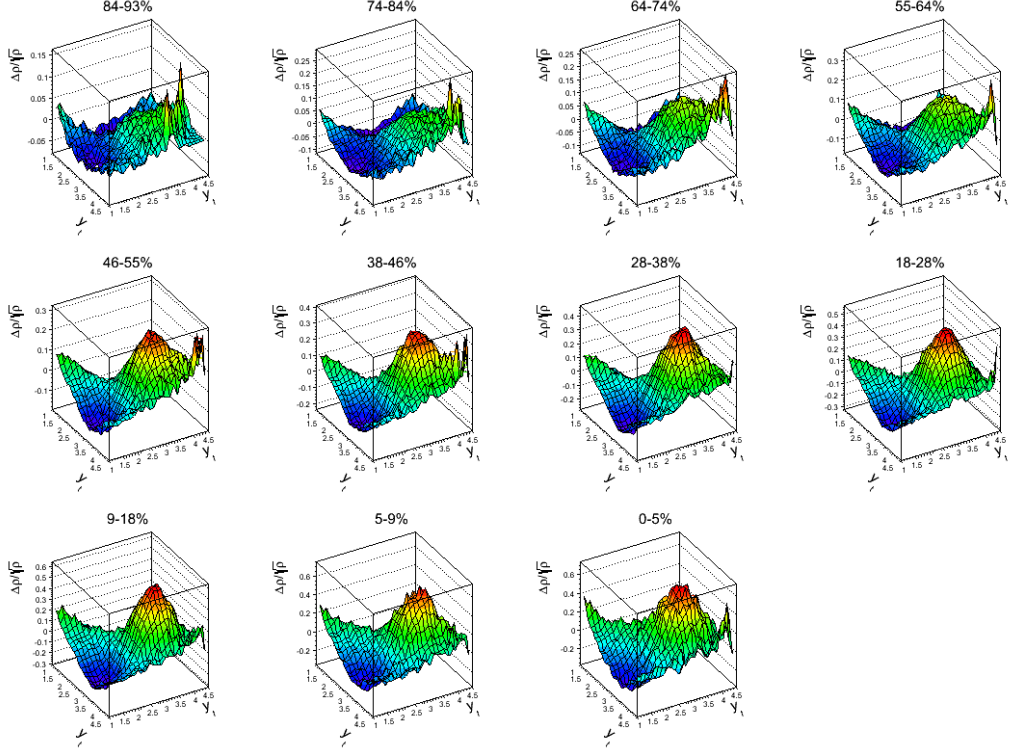


Figure 5.1: 2D CI correlations  $\Delta\rho/\sqrt{\rho_{soft}}(y_{t1}, y_{t2})$  for Au+Au collisions at  $\sqrt{s_{NN}}=200$  GeV. Centrality increases from left-to-right and top-to-bottom.

ity but remains in approximately the same location. This gradual evolution of structures with centrality differs from what is observed in angular space, where a sharp transition in the features of the correlations around the 46-55% centrality is observed [11].

The effects of different reference distributions and normalization procedures are presented in Fig. 5.2. Comparing the figures in the second row to the first demonstrates the large effect of an “event” normalization. With “event” normalization the number of sibling and mixed pairs are simply di-

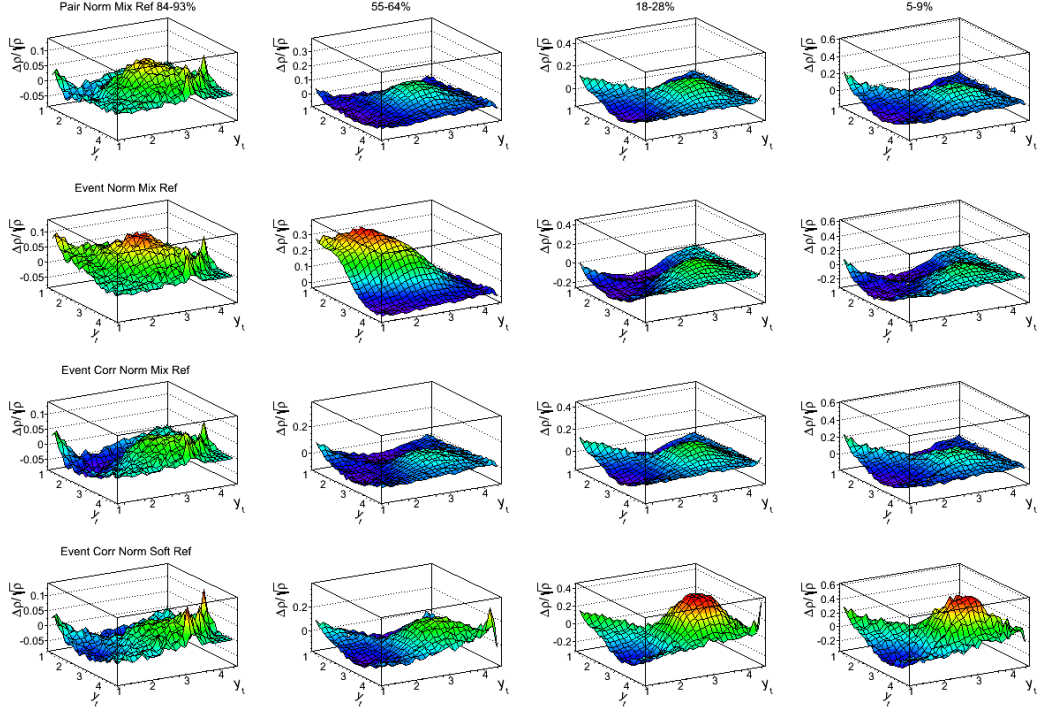


Figure 5.2: CI  $(y_{t1}, y_{t2})$  correlations for 200 GeV Au+Au collisions in four combinations of reference distributions and normalization procedures, all with a common z-axis scale. Centrality increases from left-to-right. The three upper rows use  $\rho_{mix}$  while the bottom row uses  $\rho_{soft}$ . The normalization from top to bottom is “pair”, “event” and “event” with a finite bin width correction factor (last two rows).

vided by the total number of events (sibling or mixed respectively). However, in the 55 – 64% centrality, for example, there is a large difference in the average number of sibling and mixed pairs purely due to the finite multiplicity bin width. This effect alone results in a non-zero value of  $\Delta\rho$ , even in the absence of correlations. The figures in the third row are corrected for this bias as detailed in Sec. 3.4.3.3 and now the 55 – 64% centrality bin has a structure

similar to the pair normalized data.

The data in the last row of Fig. 5.2 contain a soft reference distribution. The amplitude of the higher momentum peak increases as compared to a mixed reference. This is expected because the soft distribution is a subset of the “total” or mixed pair distribution. Therefore the denominator,  $\sqrt{\rho_{ref}}$ , is smaller and the ratio  $\Delta\rho/\sqrt{\rho_{ref}}$  becomes larger.

## 5.2 Charge and Angle Differentiations

Separating particle pairs by charge combination and/or relative opening angle is useful because some correlation sources are restricted to certain projections. Figure 5.3 contains momentum correlations in four combinations of away-side (AS), same-side (SS), unlike-sign (US), and like-sign (LS) pairs. Pairs with a relative azimuthal angle greater than  $\pi/2$  are classified as away-side and conversely pairs with a relative azimuthal angle less than  $\pi/2$  are classified as same-side.

The top two rows in Fig. 5.3 are correlations of AS LS and AS US pairs. Any evidence of back-to-back jet fragmentation is expected to be observed in these figures. A peak around  $(y_{t1}, y_{t2}) = (3, 3)$  ( $p_t=1.4$  GeV/ $c$ ) is observed, similar to the CI correlations. Interestingly, this peak persists in higher centralities, increases in amplitude, and remains in approximately the same location.

The SS LS figures in the third row of of Fig. 5.3 show clear signals from



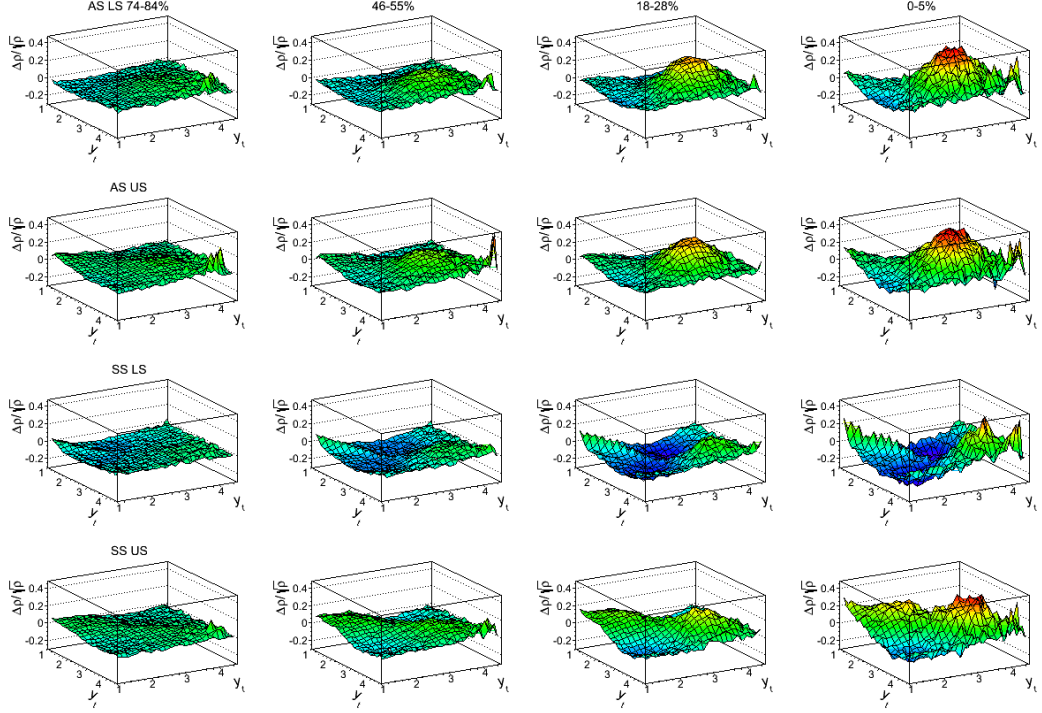


Figure 5.3: Two-dimensional  $(y_{t1}, y_{t2})$  correlations for Au+Au collisions at  $\sqrt{s_{NN}} = 200$  GeV. Centrality increases from left-to-right. The two upper rows show away-side pairs and the two lower rows show same-side pairs. The first and third rows are like-sign pairs and the second and fourth row are unlike-sign pairs.

HBT along the diagonal ( $y_{t1} = y_{t2}$ ), as expected [57]. A higher momentum peak is also observed but it is weaker than the AS correlation data. The smaller signal could be due to charge conservation effects if the primary source of jets is gluon scattering. To conserve charge, gluons fragment into pairs of positive and negative particles. Therefore a like-sign pair is only formed when there are at least four fragments, which is less probable than forming only two fragments.

Signals from intrajet correlations are expected in the SS US figures in the last row of Fig. 5.3. Surprisingly, two peaks are observed in this projection and the separation of the peaks increases with centrality. Reference [7] provides a possible explanation of this correlation feature. This paper fits identified pion and proton spectra with a two component model. The pion and proton hard and soft components are plotted in Fig. 5.4. The peaks of the pion and proton hard components are roughly at the same location ( $y_t = 2.66$ ) in peripheral collisions ( $\nu = 1$ ). Interestingly, in central collisions ( $\nu = 6$ ) the peak of the pion hard component decreases in  $y_t$  and the peak for protons increases slightly. Therefore the two peaks observed in SS US correlation data could correspond to the jet fragmentation distributions of pions and protons. This hypothesis will be tested with future studies of momentum correlations of identified particles.

Examining the difference between like-sign and unlike-sign pairs (CD = LS - US) is also informative. The charge dependent (CD) data are sensitive to local charge conservation and can present a different perspective of hadronization. Correlated pairs from minijets might exhibit a difference in LS and US pairs due to the distribution of charge during fragmentation. Conversely, pairs which contribute to the quadrupole structure and are hypothesized to be from collective flow of a thermalized medium are not expected to have a charge dependence. An analysis of CD angular correlations of  $\sqrt{s_{NN}}=130$  GeV Au+Au collisions found significant structure consistent with local charge conservation [58].

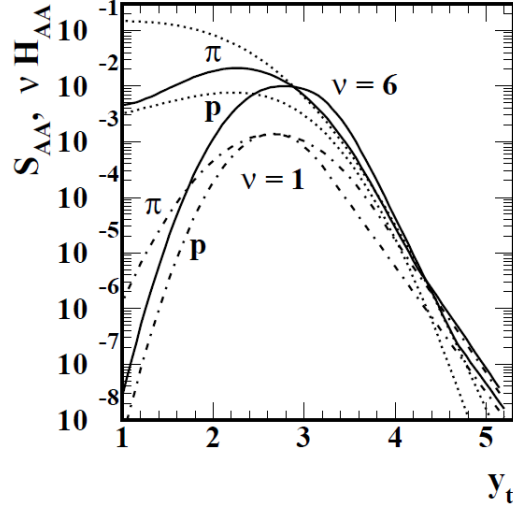


Figure 5.4: The dotted curves are the soft components for protons and pions. The dash-dot curves are the hard components for  $\nu = 1$  and the solid curves are the hard components for  $\nu = 6$  [7].

Figure 5.5 contains charge dependent  $(y_{t1}, y_{t2})$  correlations in 11 centralities for same-side pairs, in an attempt to emphasize jets. A large negative structure is observed which implies a larger unlike-sign correlation structure compared to like-sign. The shape of the correlation also does not change significantly with an increase in centrality, similar to CI correlations.

### 5.3 Fitting

The next goal is to quantify the features of the momentum correlation as a function of centrality with a 2D fitting model. The following subsections will guide the reader through each model attempted in this analysis. The advantages and disadvantages of each are presented and used to motivate the

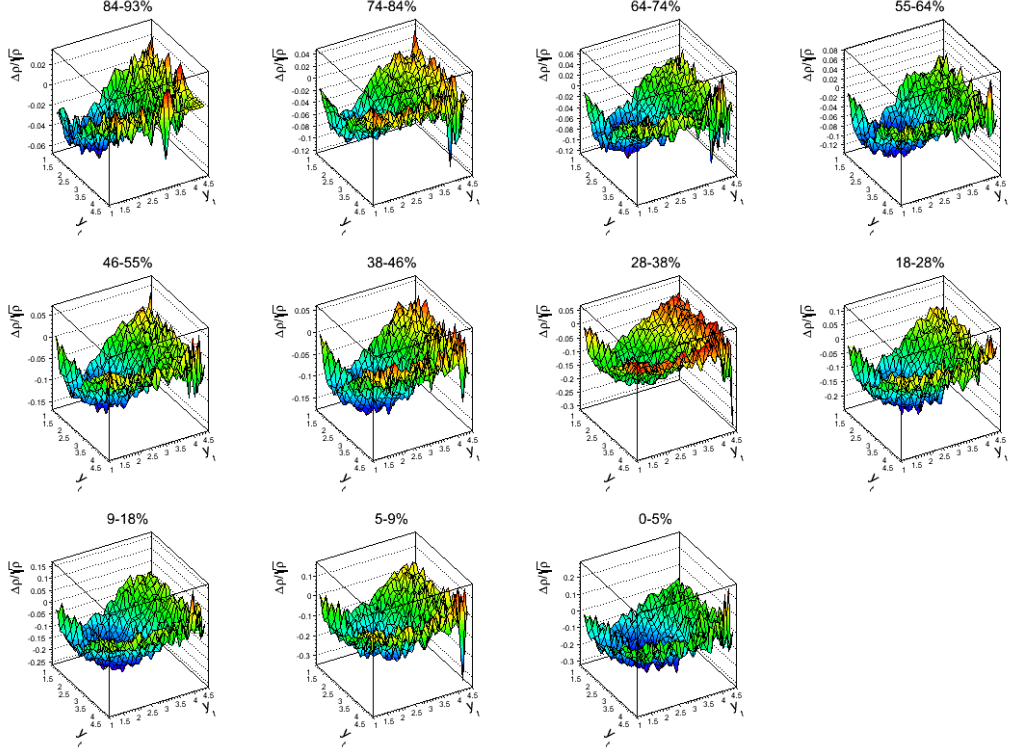


Figure 5.5: Two-dimensional  $(y_{t1}, y_{t2})$  same-side charge dependent correlations for Au+Au collisions at  $\sqrt{s_{NN}} = 200$  GeV. Centrality increases from left-to-right and top-to-bottom.

final fit model choice.

### 5.3.1 Inclusive Fit Models

A two-component analysis of single particle  $y_t$  spectra in Ref. [7] inspired the first fit model. The analysis fit 1D  $p_t$  spectra data with a Levy (soft component) and a Gaussian plus power-law tail (hard component). If the peak observed in 2D correlation data is related to the hard component then a 2D Gaussian plus a power-law tail might model the data well.

The 2D model in Eq. 5.1 consists of a 2D Gaussian with a smoothly matched power-law tail which would “wrap-around” only part of the 2D Gaussian and not appear at lower  $y_t$ . The model contains 6 parameters: the 2D Gaussian amplitude  $A$ , widths  $\sigma_\Sigma$ ,  $\sigma_\Delta$  and position  $y_0$ ; the power-law exponent  $\alpha$ ; and the smoothing factor  $\bar{\delta}$ . Later a 2D exponential was added to the fit to describe the lower momentum structure. The log-derivative between the 2D Gaussian and power-law was matched at  $\alpha/2$  according to the following expression,

$$\begin{aligned} \text{for } y'_t &\leq \alpha/2, F = Ae^{-y'^2_t} \\ \text{and for } y'_t &> \alpha/2, F = AF_\delta(e^{\alpha^2/4}e^{-\alpha y'_t} - e^{-y'^2_t}) + Ae^{-y'^2_t}, \end{aligned} \quad (5.1)$$

where

$$\begin{aligned} y'^2_t &\equiv \frac{y_{t\Delta}^2}{2\sigma_\Delta^2} + \frac{(y_{t\Sigma} - 2y_0)^2}{2\sigma_\Sigma^2} \\ F_\delta &= 1/2\sin(\delta\pi/\bar{\delta}) + 1/2 \text{ if } |\delta| \leq \bar{\delta}/2 \\ &= 0 \text{ if } \delta < -\bar{\delta}/2 \\ &= 1 \text{ if } \delta < \bar{\delta}/2 \\ \delta &= \tan^{-1}\left(\frac{y_{t\Sigma} - 2y_0}{|y_{t\Delta}|}\right), \delta \in [-\pi/2, \pi/2]. \end{aligned} \quad (5.2)$$

The model fits and residuals for three centralities are shown in Fig. 5.6. The residuals show a significant amount of structure, suggesting that this model fit is not adequate. In an attempt to improve the fits, the 2D Gaussian was replaced with a hybrid peak model that consisted of a Gaussian along the  $y_{t\Delta}$  axis and a Landau distribution along the  $y_{t\Sigma}$  axis, which has a longer

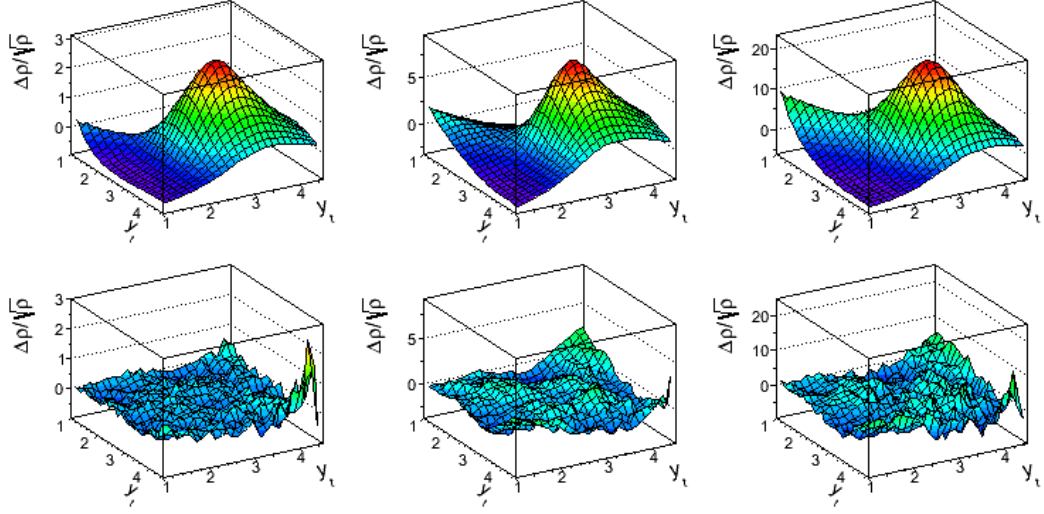


Figure 5.6: The upper panels show the inclusive model fits and the lower panels show residuals for Au+Au CI  $\Delta\rho/\sqrt{\rho_{soft}}$  data in three centralities. The centralities from left-to-right are 64-74%, 28-38%, and 0-5%.

tail than a Gaussian. A Landau distribution is a probability density function that can be expressed as a function of a location parameter  $\mu$  and a scale parameter  $\sigma$  as  $\exp[iy'_t\mu - |\sigma y'_t|(1 + \frac{2i}{\pi}\log(|y'_t|))]$ . However, this adjustment did not significantly improve the residuals.

### 5.3.2 Cut Window Method

Primarily the goal is not to describe the complete  $(y_{t1}, y_{t2})$  correlation space but just the 2D peak. Defining a region around the 2D peak with a  $y_{t\Sigma}$  and  $y_{t\Delta}$  cut can remove all the complicated structure at the lower momentum corner and along the edges. Now, only a 2D Gaussian is required to accurately fit the data contained in this cut window. The cut window ranges are specified in the captions of the figures displaying the fit models and residuals.

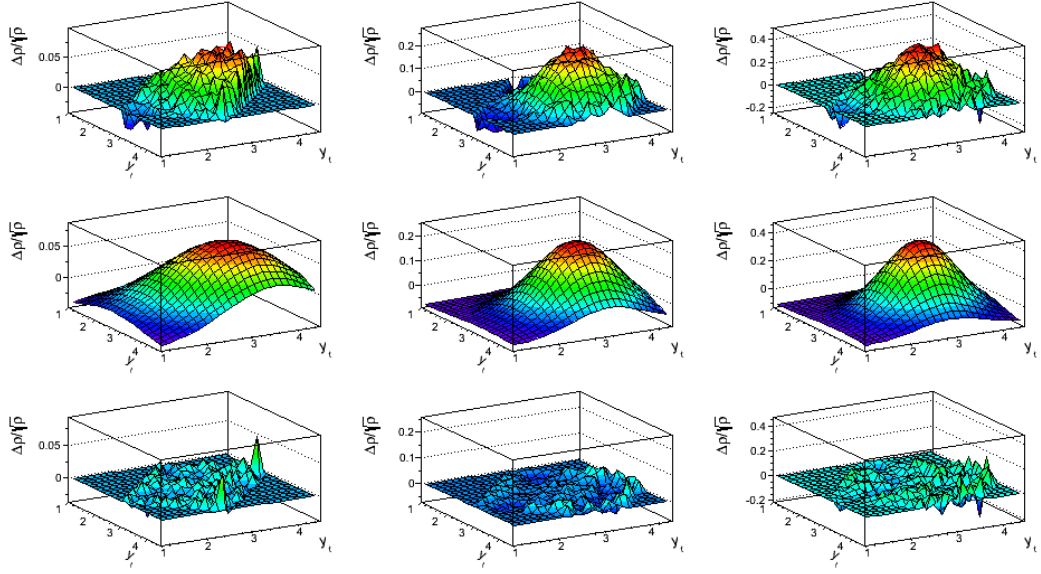


Figure 5.7: Au+Au US AS  $\Delta\rho/\sqrt{\rho_{soft}}$  data (upper), cut window model fits (middle), and residuals (lower). The centralities from left-to-right are 74-84%, 38-46%, and 0-5%. The cut window is approximately  $|y_{t\Delta}| < 2.0$  and  $4 < y_{t\Sigma} < 8$ .

Figure 5.7 shows the US AS data in the cut window as well as the fit models and residuals. The residuals contain very little structure. The LS AS fit results in Fig. 5.8 have similar properties.

The US SS data had an unusual double peak feature. This feature was easily modeled with the addition of a second 2D Gaussian. The fit results can be seen in Fig. 5.9.

The cut window for the LS SS data is positioned higher in  $y_t$  to describe the relatively higher location of the peak in the data and also to avoid the HBT correlation at lower momentum. The fit results can be seen in Fig. 5.10.

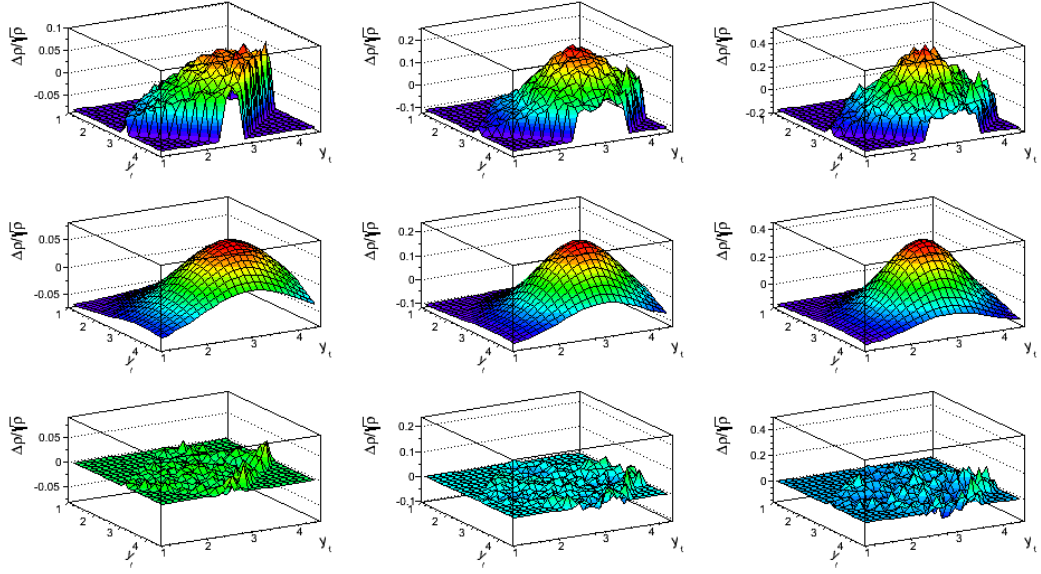


Figure 5.8: Au+Au LS AS  $\Delta\rho/\sqrt{\rho_{soft}}$  data (upper), cut window model fits (middle), and residuals (lower). The centralities from left-to-right are 74-84%, 38-46%, and 0-5%. The cut window is approximately  $|y_{t\Delta}| < 2.0$  and  $4 < y_{t\Sigma} < 8$ .

The fit parameters for all charge and angle combinations in all centralities are presented in Fig. 5.11. The amplitude of the 2D Gaussian rises monotonically in all cases. The Gaussian widths remain relatively constant for the AS LS, AS US, and US SS data. Due to the weaker correlation signal in the LS SS data, the trend of the fit parameters is more varied. The position of the 2D Gaussian is surprisingly constant as a function of centrality. It remains between  $y_t$  values of 3 and 3.5 for all charge combinations. The lower momentum peak that appears in the US SS data is centered around  $y_t=1.5$ .

While the cut window method vastly simplifies the fitting problem, it lacks any correspondence to a theoretical model. Therefore, the search



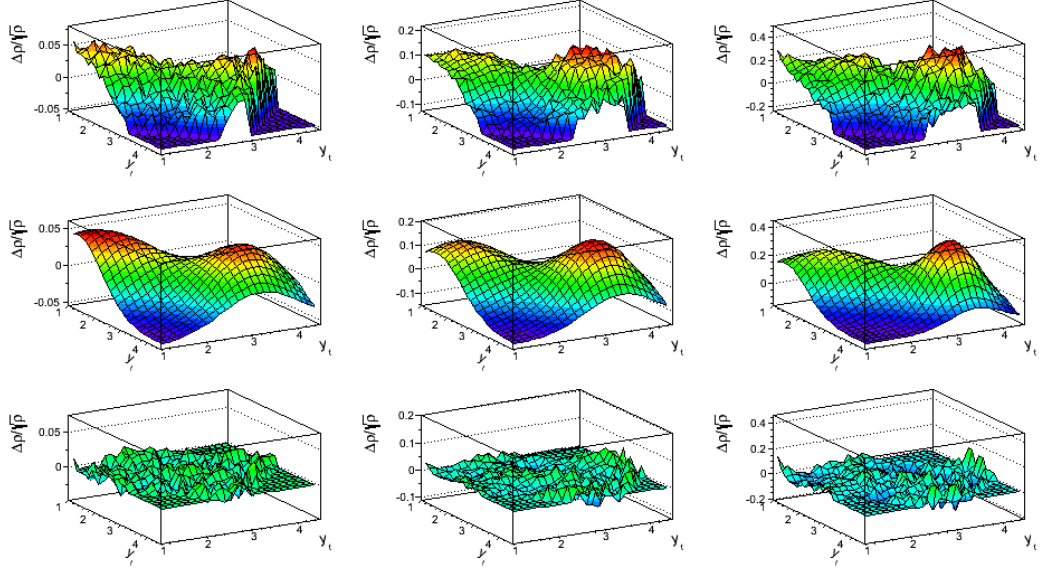


Figure 5.9: Au+Au US SS  $\Delta\rho/\sqrt{\rho_{soft}}$  data (upper), cut window model fits (middle), and residuals (lower) . The centralities from left-to-right are 74-84%, 38-46%, and 0-5%. The cut window is approximately  $|y_{t\Delta}| < 2.0$  and  $y_{t\Sigma} < 8$ .

continued to find a model that not only describes the transverse momentum correlation data but also gives insights into the correlation mechanisms.

### 5.3.3 2D Levy Model

An analysis of 130 GeV Au+Au data in Ref. [57] inspired the following fit model. That paper presents two-particle correlations on transverse momentum variable  $X(p_t) \equiv 1 - \exp\{-(m_t - m_0)/0.4 \text{ GeV}\}$  and compared it to theoretical predictions. The extent to which pQCD could match the data was tested with events generated from HIJING. HIJING matched the high momentum region of the data but failed to predict the lower momentum region,

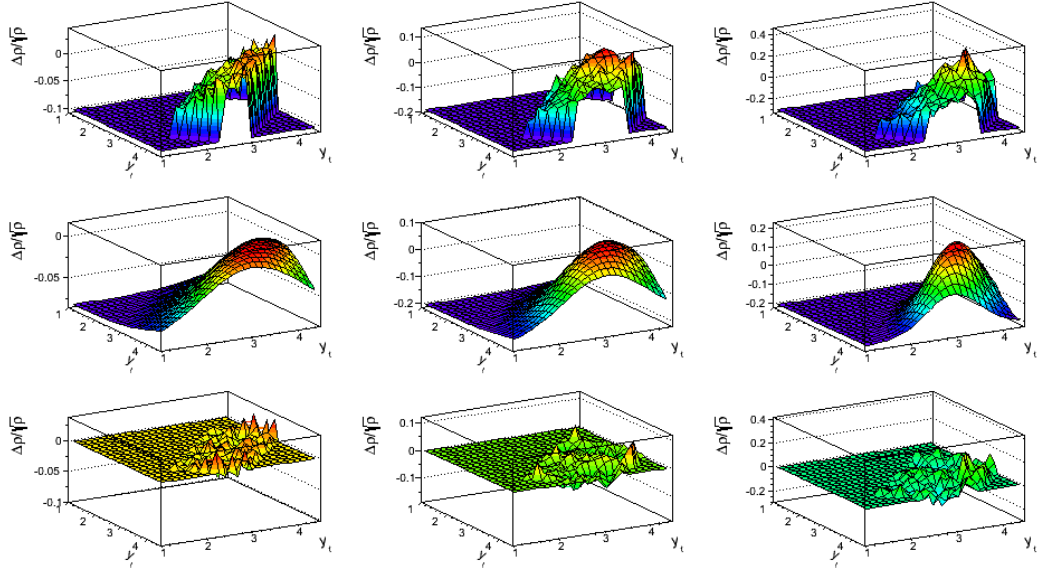


Figure 5.10: Au+Au LS SS  $\Delta\rho/\sqrt{\rho_{soft}}$  data (upper), model fits (middle), and residuals (lower). The centralities from left-to-right are 74-84%, 38-46%, and 0-5%. The cut window is approximately  $|y_{t\Delta}| < 2.0$  and  $5.5 < y_{t\Sigma} < 8$ .

which had a distinct saddle shape.

That paper investigated the possibility that the saddle shape may be due to fluctuations in the lower momentum single particle distribution. The spectrum in the lower momentum region ( $0.15 \leq p_t \leq 2$  GeV/c) can be described with a  $\exp(-m_t/T) = \exp(-m_t\beta)$  function. The inverse slope parameter  $T$  is conventionally referred to as “temperature” and  $\beta = 1/T$ . The terminology is unfortunate because there are other possible, non-thermal sources of this trend, e.g. longitudinal string fragmentation, recombination, or any source giving rise to the soft component.

A model was then developed to predict correlations due to fluctuations

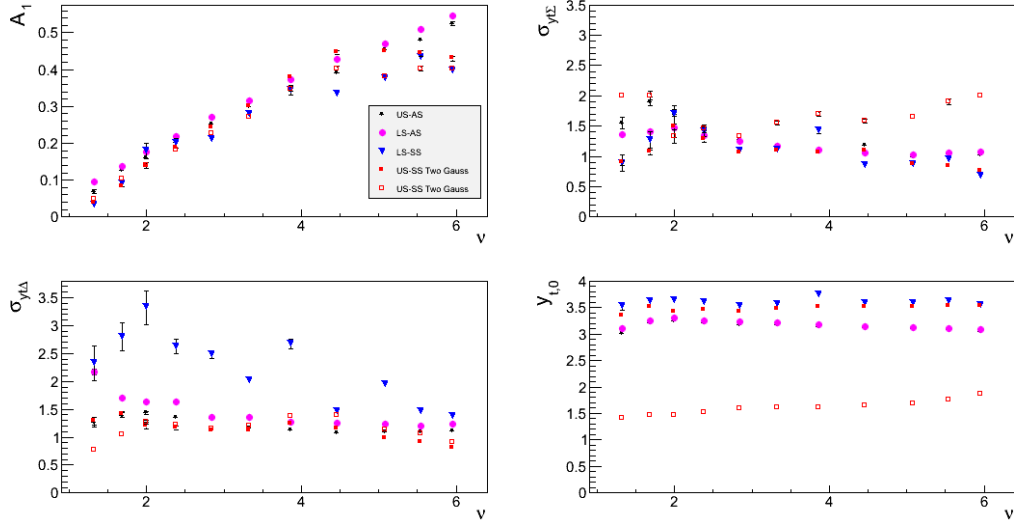


Figure 5.11: Fit parameters for  $(y_t, y_t)$  correlation data versus centrality measure  $\nu$ . The parameters in the upper row are the 2D Gaussian amplitude (left) and the  $y_{t\Sigma}$  width (right). The lower row contains the  $y_{t\Delta}$  width (left) and the center location along the diagonal ( $y_{t1} = y_{t2}$ ) (right). The error bars represent fitting errors derived from the statistical error of the data.

in the lower momentum single particle distribution. The  $m_t$  distribution in Eq. 5.3 was calculated from the convolution of two distributions:  $\exp(-\beta(m_t - m_0))$ , which is the momentum distribution of an ensemble of events for a given  $\beta$ ; and  $g_1(\beta - \beta_0)$ , which represents the distribution of  $\beta$  from event to event as well as within an event.  $g_1(\beta - \beta_0)$  is any general peaked distribution that is peaked at  $\beta_0$ .

$$\frac{dN}{m_t dm_t} = A \int_0^\infty d\beta g_1(\beta - \beta_0) e^{-\beta(m_t - m_0)} \quad (5.3)$$

If  $g_1(\beta - \beta_0)$  is modeled as a Gamma distribution then the expression

above can be expressed as a Levy distribution

$$\frac{dN}{m_t dm_t} = A / [1 + \beta_0(m_t - m_0)/n_{fluct}]^{n_{fluct}}, \quad (5.4)$$

where  $1/n_{fluct} = \sigma_\beta^2/\beta_0^2$  is the relative variance of  $g_1(\beta)$ .

In that paper the *two-particle* momentum distribution of pairs was determined by convoluting the two-particle distribution function  $\exp[-\beta_1(m_{t1} - m_0)]\exp[-\beta_2(m_{t2} - m_0)]$  with the 2D distribution  $g_2(\beta_1, \beta_2)$ . The particles were sampled from local  $m_t$  distributions determined by  $\beta(\eta, \phi)$ . The shape of the 2D distribution  $g_2(\beta_1, \beta_2)$  has two limiting cases worth mentioning: the particles in an event are not point-to-point correlated; or the event is equilibrated at a value of  $\beta$ , but  $\beta$  can fluctuate from event to event. In Ref. [57] it was found that the model which matched the data best had an intermediate description such that there are some point-to-point correlations and  $\beta$  fluctuates from event to event.

The two-particle sibling density is given by

$$\begin{aligned} \frac{d^4 N}{m_{t1} dm_{t,1} d\eta m_{t,2} dm_{t,2} d\eta} &= A \int \int d\beta_1 d\beta_2 g_2(\beta_1, \beta_2) e^{-\beta_1(m_{t1} - m_0)} e^{-\beta_2(m_{t2} - m_0)} \\ &= \left(1 + \frac{\beta_0 m_{t\Sigma}}{2\eta_\Sigma}\right)^{-2\eta_\Sigma} \left[1 - \left(\frac{\beta_0 m_{t\Delta}}{2\eta_\Delta + \beta_0 m_{t\Sigma}}\right)^2\right]^{-\eta_\Delta} \end{aligned} \quad (5.5)$$

where  $1/\eta_\Sigma$  and  $1/\eta_\Delta$  are the relative variances of  $g_2(\beta_1, \beta_2)$ ,  $\Delta(1/n)_\Sigma \equiv \frac{1}{\eta_\Sigma} - \frac{1}{n_{fluct}}$ , and  $\Delta(1/n)_\Delta \equiv \frac{1}{\eta_\Delta} - \frac{1}{n_{fluct}}$ . The relative covariance of  $g_2$  is  $(1/n)_{tot} \equiv 1/\eta_\Sigma - 1/\eta_\Delta$ .

The complete model function that was compared to data in the present analysis was  $\sqrt{\rho_{soft} \frac{\hat{n}_{sib} - \hat{n}_{mix}}{\hat{n}_{soft}}}$ , where  $\hat{n}_{sib}$  is the normalized quantity in Eq. 5.5,

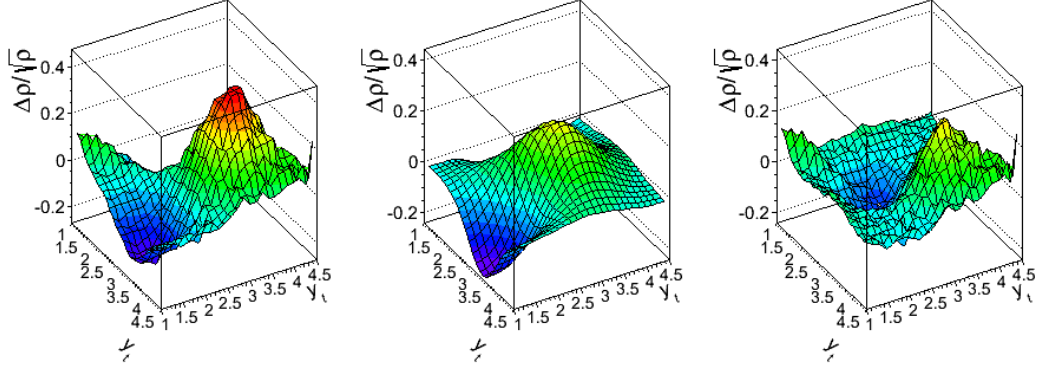


Figure 5.12: Data (left), Levy fit model (middle) and residual (right) for CI 200 GeV 28-38% central Au+Au collisions.

$\hat{n}_{mix}$  is the normalized product of two single particle spectra, and  $\hat{n}_{soft}$  is the normalized soft particle spectra. The three parameters contained in  $\hat{n}_{sib}$  that were allowed to vary were  $n_{fluct}$ ,  $\Delta(1/n)_{\Sigma}$ , and  $\Delta(1/n)_{\Delta}$ .

Figure 5.12 contains a fit with this model to CI data in centrality bin 28-38%. The 2D Levy fit model can describe the saddle shape seen in the data but the residual contains a significant amount of structure. Since some of the residual is from background contamination like HBT or electrons, further fits were made to away-side CI data in which these contributions are not found. Also, a 2D Gaussian was added to help reduce the residuals. The fit results for this new configuration are shown in Fig. 5.13.

The parameters of the fit to AS CI data in all 11 centralities are shown in Fig. 5.14. This fit method's ability to fit the majority of the structure in  $(y_t, y_t)$  correlations is promising. Also, the concept of a fluctuating “soft” component and a 2D Gaussian “hard” component is meaningful and important

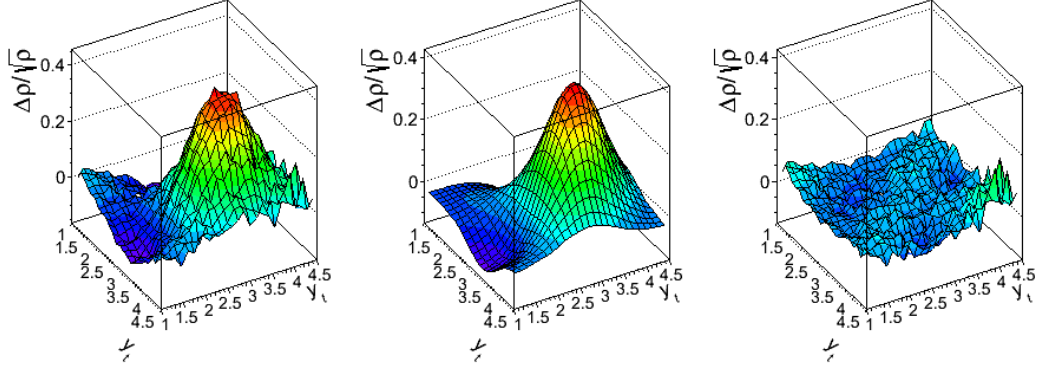


Figure 5.13: Data (left), 2D Levy fit plus Gaussian model (middle) and residual (right) for AS CI 200 GeV 28-38% central Au+Au collisions.

in the development of a complete view of the heavy ion system.

## 5.4 Model Comparisons

Momentum correlations, specifically the peak observed around  $(y_{t1}, y_{t2}) = (3, 3)$  ( $p_t=1.4$  GeV/ $c$ ), reveal an important new feature of the data in which theoretical models can be compared. The three models presented in this section include a variety of possible dynamics in heavy ion collisions. HIJING predicts pQCD minijets with no collective behavior. AMPT, which includes jets, predicts a quadrupole in angular correlations using a hybrid transport model that includes a period of parton-parton re-scattering. NexSphERIO is a hydrodynamical model with fluctuating initial conditions that also predicts a ridge-like structure in angular correlations as well as a quadrupole.

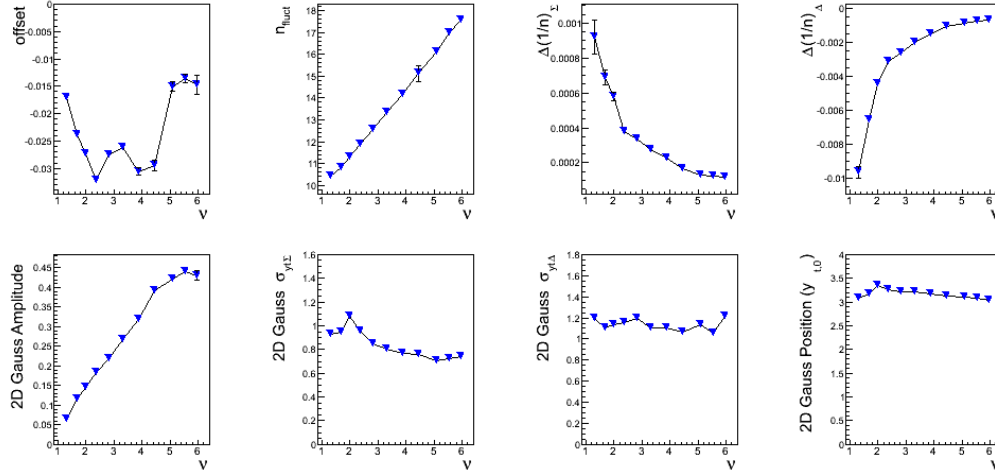


Figure 5.14: Fit parameters for AS CI ( $y_{t1}, y_{t2}$ ) data versus centrality measure  $\nu$ . The parameters in the upper panels corresponds to the 2D Levy component. The parameters in the lower panels correspond to the 2D Gaussian. The two most peripheral centralities had a reduced ( $y_{t1}, y_{t2}$ ) range ( $y_{t\Sigma} < 4.0$ ). The error bars represent fitting errors derived from the statistical error of the data.

#### 5.4.1 HIJING

HIJING is a Monte-Carlo event generator that is based on the LUND string model and pQCD semi-hard jet fragmentation [53]. These components originated in PYTHIA, which models a single binary (nucleon-nucleon) collision [49]. Heavy ion collisions in HIJING are described as a superposition of nucleon-nucleon collisions. The number of binary collisions is estimated with a Glauber simulation where the distribution of nucleons in a heavy ion nucleus is described with a Wood-Saxon profile. HIJING can also include jet quenching which helps reproduce the observations of missing transverse energy for jets in data. For this study, jet quenching was turned off in order to maximize jet

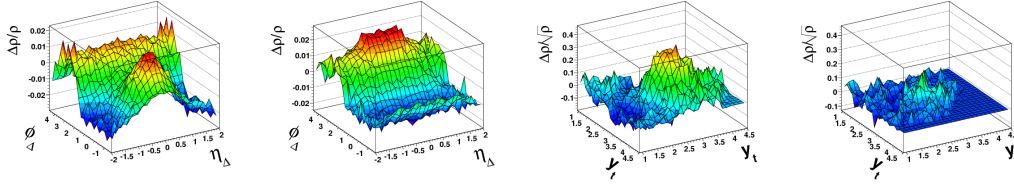


Figure 5.15: Two-particle correlations from HIJING for 75-85% central events. The first and third panel show results with jets on; the second and fourth are with jets off.

correlations.

In HIJING, high- $p_t$  transfer processes (i.e. jets) can also be simply turned on or off. Therefore, the jet contribution to angular and momentum correlations can be observed by comparing the two settings. Approximately 600,000 HIJING events were generated via the AMPT model code (v1.21-v2.21). AMPT reduces to HIJING when the parton-parton interaction cross section is set to zero. All charged particles were analyzed with the  $p_t > 0.15$  GeV/c,  $|\eta| < 1$ , and full azimuth.

The results in Fig. 5.15 show that HIJING with jets turned on reproduces the data well in angular space in peripheral collisions [11]. A peak is also observed in the  $(y_t, y_t)$  correlations that is similar to data. When jets are turned off the same-side peak in angular space disappears, which is expected from a minijet hypothesis. Interestingly the peak in the momentum correlations disappears as well. This study suggests that most of the pairs in the  $(y_t, y_t) = (3, 3)$  peak are from jet fragmentation.



### 5.4.2 AMPT

AMPT (A Multi-Phase Transport Model) consists of four main components; initial conditions, partonic interaction, hadronization, and hadronic interaction [59]. With increasing partonic interaction, AMPT can generate a quadrupole component, which motivates the investigation of the corresponding momentum correlations.

AMPT's initial conditions are obtained from HIJING and include spatial and momentum information of minijets and soft strings (i.e. the color flux tubes in the Lund fragmentation model). Next, the ZPC (Zhang's Parton Cascade) models a phase of partonic-partonic interactions. The partons which are included in this interaction depends on which of two running modes is chosen. The first and default option allows only minijet partons to interact. The second options is called "string melting" and allows interactions of both minijet partons and soft strings (after being converted to partons). Without string melting it can be argued that the partonic interaction effects will be underestimated. The study presented here used the "string melting" mode in order to maximize the effects of parton-parton scattering.

The hadronization procedure in the third phase is dependent on the running mode as well. In the default AMPT mode, minijet partons will recombine with the remaining strings in their parent nucleons after they stop interacting. The new excited strings then hadronize using the Lund string fragmentation model. In string melting mode, the partons are hadronized using a simple quark coalescence model. The model combines the two nearest par-

tons (in space-time) into mesons and the three nearest quarks into baryons. A source of concern is that this coalescence model considers only the coordinate space location, not the relative momentum value of the partons. While total energy is not conserved, the three-momentum is conserved and the species is assigned to whichever hadron is closest in mass.

The last phase involves a period of hadronic re-scattering using the ART (A Relativistic Transport) model. For the purposes of this study the hadron re-scattering was turned off. The effects of this phase were examined and believed to be small but will be studied in the future.

The two body scattering cross section in the second phase is approximately  $\frac{9\pi\alpha_s^2}{2\mu^2}$  [59] and in the default setting equals 3 mb. The strength of the interaction can be adjusted with a change to either the screening mass  $\mu$  or the strong coupling constant  $\alpha_s$ . This study looked at a range of cross sections from zero (HIJING-like) to a value that produces a quadrupole amplitude that matches the data.

The hadron-hadron correlations, however, produced some suspicious results. The increase from 0 mb to 3 mb created a dramatic increases in the size of the same-side peak (amplitude and  $\eta$  width) but the  $\phi$  width surprisingly decreases. Intuitively one would assume that as the scattering amongst particles increases, the  $\phi$  width of a jet would increase as well. Also, the peak in  $(y_t, y_t)$  space was surprisingly unaffected

Some of the non-intuitive behavior might be due to the coalescence

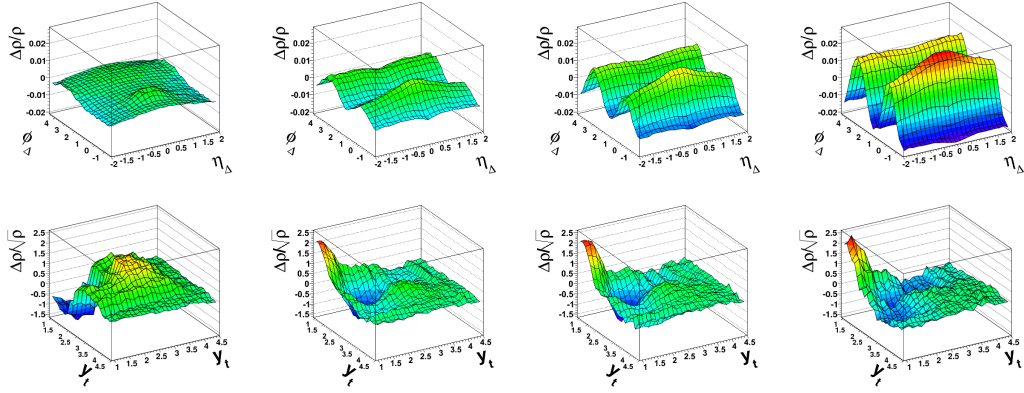


Figure 5.16: Two-parton correlations from AMPT for collisions in the 45-55% centrality bin. The upper row contain angular space correlations and the bottom row contain momentum space correlations. The partonic cross section values are (left to right) 0 mb, 1.5 mb, 3 mb, and 6 mb.

hadronization model. Forming correlations on the parton instead of hadron level will eliminate the effects of the assumed hadronization model. Figure 5.16 contains parton-parton correlations for four values of partonic cross section in angular space (upper) and momentum space (lower). For this preliminary survey, the correlations were formed with a mixed pair reference and pair normalization. In any case, final comparison between model and data should be with the same reference distribution and normalization to allow for direct comparisons.

Fits to the data were made with the standard 11 parameter fit function [11]. The trend of the fit parameters made somewhat more sense on the parton level than the hadron level. With the initial increase in partonic interaction the  $\phi$  width of the same-side peak increases (but then decreases). As a point of reference, the amplitude of the quadrupole in data in this centrality

is 0.136. The amplitude of the AMPT model at 6 mb is 0.115 and at 12 mb is 0.153. Therefore a partonic cross section somewhere between 6 and 12 mb was needed to produce a quadrupole amplitude that matched the data.

The momentum correlations in the bottom row of Fig. 5.16 show, for 0 mb, a higher momentum peak similar to what is observed in data. With a slight increase in cross section, however, this peak quickly dissipates. The peak gradually re-appears with higher values of partonic cross section. This study suggests that, while AMPT can describe some features of heavy ion data in angular space, it fails to reproduce the observed correlation structure in momentum space.

### 5.4.3 NexSpheRIO

The proclaimed successes of hydrodynamics motivates the attempt to compare its predictions to  $(y_t, y_t)$  data. Hydrodynamics describes strong collective flow assuming local thermal equilibrium. This model reproduces many aspects of the data but cannot describe the entire lifetime of the medium without using adjustable parameters for the initial conditions, equation of state, hadronization and freeze-out transitions.

NexSpheRIO is a hybrid of the Spherio and Nexus models [60]. Spherio is based on the Smoothed Particle Hydrodynamics (SPH) method which originated in the field of astrophysics [61]. The initial conditions in Spherio are expressed in terms of distributions of fluid velocity and generally averaged over small variations in local features. However, recent developments in the

field have identified the importance of small fluctuations in the density profiles of the colliding nuclei. These fluctuations are proposed to generate many correlation structures including the same-side ridge [62]. Nexus is the component of NexSpheRIO which provides fluctuating initial conditions.

Reference [63] contains an analysis of 200 GeV Au+Au NexSpheRIO events in angular space. While the model was successful in predicting a same-side ridge, predictions of the correlations in momentum space need to be also compared to data.

A public copy of the Spherio code is available online and a copy of Nexus was obtained through personal communications. Many attempts were made to produce events but at the time of this dissertation none were successful in producing a reliable, trustworthy sample. However, the events used in the publication of Ref. [63] were made available. The two-particle correlation results from these events are shown in Fig. 5.17.

The figures in the upper panel of Fig. 5.17 approximately match the results reported in Ref. [63]. The momentum correlations in the lower row are formed with a mixed pair reference and pair normalization. A higher momentum peak can be seen in all the centralities except the 0-10% bin. However, the inability to reproduce these NexSpheRIO events directly prevents any confident conclusion of the physical implications of this analysis at this time.

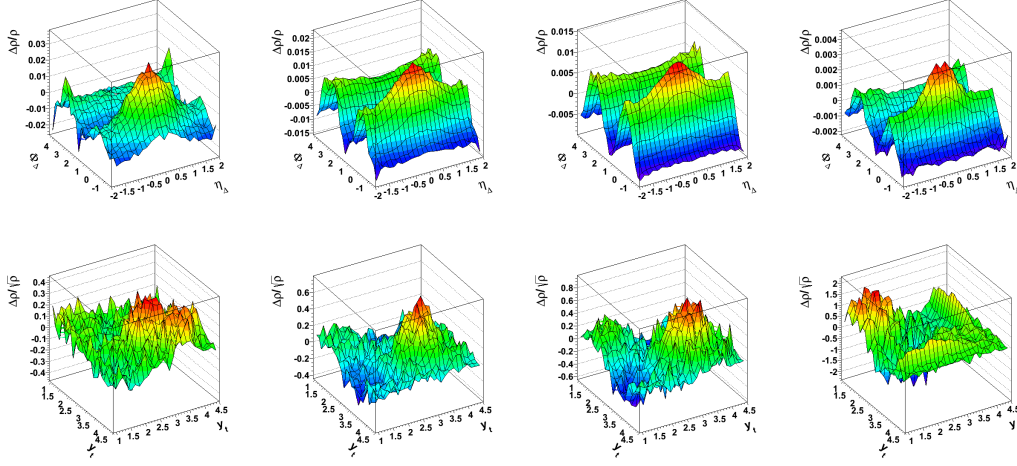


Figure 5.17: Correlations from NexSphRIO events in angular (upper) and momentum (lower) space for Au+Au 200 GeV collisions in four centralities. The centralities, from left-to-right, are 60-80%, 40-60%, 20-30%, and 0-10%.

## 5.5 Errors and Reference Distributions Choices

The statistical errors on the quantities  $n_{sib}$  and  $n_{mix}$  are equal to the square root of the number of pairs. These errors are then propagated through the calculation of the quantity  $\Delta\rho/\sqrt{\rho_{mix}}$ . The errors on the final quantity  $\Delta\rho/\sqrt{\rho_{soft}}$  assume proportional errors as demonstrated in Eq. 5.6.

$$\text{Error} \left( \frac{\Delta\rho}{\sqrt{\rho_{soft}}} \right) = \frac{\text{Error} \left( \frac{\Delta\rho}{\sqrt{\rho_{mix}}} \right)}{\frac{\Delta\rho}{\sqrt{\rho_{mix}}}} \frac{\Delta\rho}{\sqrt{\rho_{soft}}} \quad (5.6)$$

The statistical errors of the correlation data in  $(y_t, y_t)$  space are shown in Fig. 5.18. Since it is proportional to the number of pairs in the bin, the largest errors are found in the higher momentum region where statistics are poor.

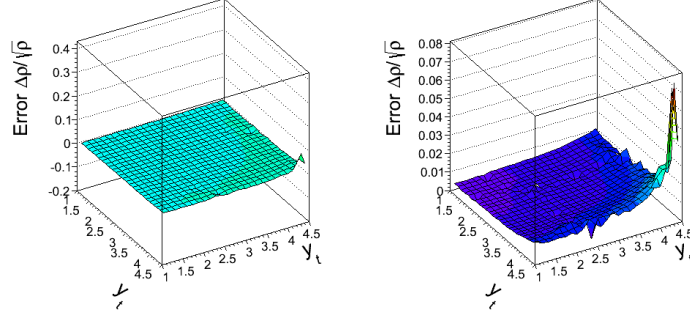


Figure 5.18: The statistical error on the final  $\Delta\rho/\sqrt{\rho_{soft}}(y_{t1}, y_{t2})$  data for 38-46% central collisions. The z-axis scale on the left panel is equal to the data. The z-axis scale on the right panel is zoomed in for better visual access.

The amplitudes of the errors fluctuate and increase slightly from peripheral to central collisions. The maximum error for most of the centralities is between 0.1 and 0.15. However, in the 28-38% centrality there is a large spike in the error that is due to a small value of  $\Delta\rho/\sqrt{\rho_{mix}}$ . This effect is observed in only this bin.

### 5.5.1 Systematic Errors

Any potential biases in the  $(y_{t1}, y_{t2})$  correlation data due to track or event selection criteria, or experimental inefficiencies qualify as systematic errors. This section will describe the types of systematic errors investigated thus far. There are remaining issues to investigate including systematic errors due to the choice of fitting model. The sources of systematic errors which were found to be insignificant (i.e. less than statistical noise) will be described first.

Events are grouped in multiplicity ranges that are typically no wider

than  $\Delta N_{ch} = 50$ . This ensures the ratio  $\Delta\rho/\rho$  is formed from events with similar multiplicities. Any dependence on this multiplicity bin width was investigated by reducing the width in half, to approximately  $\Delta N_{ch} = 25$ . The difference in the correlation data between the two configurations was found to not exceed statistical noise.

When STAR collected Au+Au data in 2004 the detector operated for a period of time in each of the two magnetic field orientations. The correlation data should, in principle, not depend on the magnetic field orientation but any charge-dependent effects could be identified by analyzing events taken in both orientations separately. The difference in the data was observed to be smaller than statistical noise. It should also be noted that the ratios  $\Delta\rho/\rho$  are always formed from events with the same magnetic field orientation.

The effects of the transverse momentum resolution, which is on average a few percent [64], were examined by convoluting a 2D Gaussian smearing function, whose widths depend on the  $y_t$ -dependent resolution, with the data:

$$F(y_{t1}, y_{t2}) = \int dy'_{t1} \int dy'_{t2} \frac{\Delta\rho}{\sqrt{\rho}}(y'_{t1}, y'_{t2}) \frac{1}{2\pi\sigma_1\sigma_2} e^{-1/2 \left[ \frac{(y_{t1}-y'_{t1})^2}{\sigma_1^2} + \frac{(y_{t2}-y'_{t2})^2}{\sigma_2^2} \right]}, \quad (5.7)$$

where  $\sigma$  is the  $p_t$  resolution obtained from [64]. The effect of this smearing was less than statistical noise.

The sources of systematic error which were larger than statistical noise include two-track inefficiencies, primary vertex finding inefficiencies, secondary particle contamination, and conversion electrons. These errors will ultimately



be reported with the 2D  $(y_{t1}, y_{t2})$  fitting parameters.

Two-track inefficiencies from track merging or crossing are reduced by removing pairs that satisfy a group of conditions described in Sec. 3.3.1. One of the requirements in the track merging cut is that the separation distance in both the longitudinal and transverse direction are less than 5 cm at any of three radial points. The tracking crossing cut had a similar separation distance requirement. An alternative method used in previous analyses would reject pairs based on the *average* of the separation distances at a few points along the track. A difference in the data between these two methods was found in the  $y_t = [1.5, 3]$  region in mid-central events and can be approximately modeled by a Gaussian. The systematic error on the fit parameters from this effect is approximately one-third of the difference between the two configurations.

In the three most central bins (0-5%, 5-9%, 9-18%), events are binned according to their z-vertex positions with a bin-size of 5 cm. This ensures the events in a bin have similar effective experimental acceptances that cancel in the ratio  $\Delta\rho/\rho$ . Reducing the bin size from 5 cm to 2 cm was found to not have an effect on the data. Events in the eight most peripheral centralities are typically not grouped by z-vertex position so, for this study, a 5 cm range was introduced. The result was a net increase in the data at higher  $y_t$  that can be modeled as a constant offset. The offset component of the fit should be adjusted by half the difference between the two configurations (no binning and 5 cm binning). The systematic error on the offset due to this effect is also half the difference.

Contamination of particles that did not originate from the primary vertex, known as secondary particles, is reduced by requiring the distance of closest approach (DCA) of a track to the primary vertex to be less than 3 cm. Reducing the DCA cut to 1 cm measures any remaining contamination from secondary particles. A direct comparison between a 1 cm and 3 cm analysis is complicated because the standard centrality definitions are given as ranges in  $N_{ch}$  with a 3 cm DCA cut. Therefore the same event could be classified in two different centralities if the DCA cut is reduced. In order to properly classify events, new centrality definitions need to be made for the distribution of events on multiplicity with a 1 cm DCA cut. While the analysis of the data with new centrality definitions was not finished at the time of this dissertation, preliminary findings show the effect occurs in the lower momentum regions of the more central bins.

Systematic error due to any remaining pileup contamination after applying the pileup removal procedure was also investigated. Pileup is most easily identified in angular data and primarily affects the 1D Gaussian component in mid-centralities. Comparing the centrality dependence of the amplitude of the 1D Gaussian in angular space before and after the pileup removal procedure suggests that approximately 10% of the pileup still remains. The systematic error on the fit parameters due to this effect is 10% of the difference between the data with and without the pileup removal procedure in centralities 2 through 7 (18-74%).

Lastly, photon interaction with detector material produces pairs of elec-

trons and positrons. This is a well-known background that will be described in more detail in Sec. 5.5.3. The distribution of electron pairs is located at low  $y_t$  and can be modeled with an exponential. The systematic error is 1/3 the difference between the final fit parameters and those obtained by fitting the data minus the electron component.

### 5.5.2 Reference Distribution

The soft distribution  $\rho_{soft}$  used in the final results is described in Sec. 3.4.2 but there are other approaches to estimating the soft reference distribution. While the effects of choosing other values of  $\rho_{soft}$  should be discussed, they do not qualify as true systematic errors on the correlation measurements. Three of the five options for estimating the soft reference, described below, incorporate particle identified data from the analysis in Ref. [7]. The other two utilize STAR and PHENIX unidentified spectra data that was not available at the time [7] was published. Figure 5.19 contains a 1D distribution of five options for the soft reference.

In Ref. [7] the soft component is reported for identified pions and protons only. To form a reference for an inclusive analysis it was therefore necessary to add the kaon component. However, there is ambiguity in the kaon component due to an observed enhancement of the kaon to proton yield in heavy ion collisions. Should this enhancement be attributed to the soft or hard component?

One option is to assume the entire enhancement is associated with the

hard component  $x_K$ . The value of  $x_K$  was estimated from the slope parameter of a linear fit to  $\frac{dN}{d\eta} \frac{1}{\langle N_{part} \rangle / 2}$  versus  $\nu$ . The integrated yields,  $dN/d\eta$ , were obtained with Maxwell-Boltzmann fits to kaon spectrum data from STAR [44]. The relative yield  $f_K(\nu)$  should not change for the soft component in this scenario. This option is labeled in Fig. 5.19 as “All Hard Component”.

Alternatively, some of the enhancement could be present in the soft component and the enhancement in the yield of the kaons in the soft component  $f_K(\nu)$  will vary with centrality. The value of  $x_K$  can be estimated from pion data in the p-p limit. In the present analysis this would correspond to no enhancement over binary scaling in heavy ion collisions. This option is labeled in Fig. 5.19 as “Some Soft - fixed x”. The other option, used in the final results, calculates  $x_K$  from pion data over the entire range of  $\nu$  and more accurately represents the increase over binary scaling. This option is labeled in Fig. 5.19 as “Some Soft - fixed H”.

The last two options were obtained from STAR [41] and PHENIX [42] unidentified spectra separately. In this method the particle densities were extrapolated to the  $\nu=0$  limit for each  $p_t$  value. There were several instances of incomplete centrality and momentum information so extrapolations had to be taken carefully or not at all. The soft components were then described with Levy distributions like in Eq. 3.20. The parameters of the distribution from STAR were  $A=4.32$ ,  $T=0.1342$  GeV,  $n=9.67$  and the parameters from PHENIX were  $A=11.94$ ,  $T=0.0955$  GeV, and  $n=8.22$ .

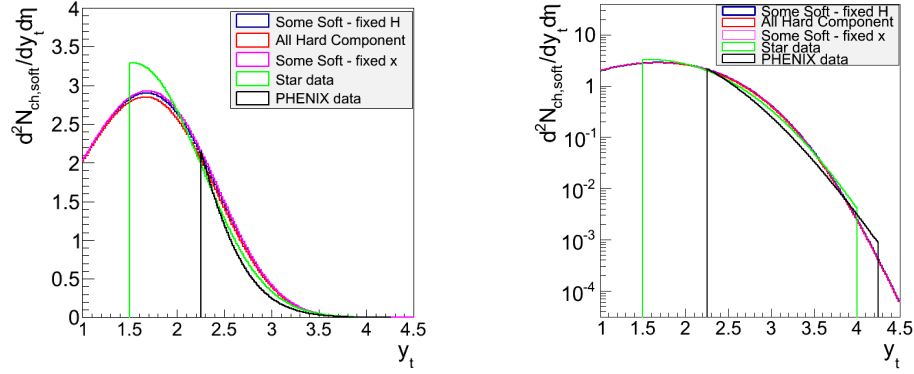


Figure 5.19: A distribution of  $\rho_{soft}$  on  $y_t$  for five different configurations on a linear (left) and log (right) scale.

### 5.5.3 Electron Contamination Simulation

Electrons are considered background for this correlation analysis, as the majority of them are produced from photons interacting with detector material. In angular space, the correlated electrons form a distinct 2D exponential shape near the origin. A simulation study was performed to see how the electrons are distributed in momentum space.

The simulation studied photons that originated from the decay of neutral pions ( $\pi^0$ ). First, a candidate  $\pi^0$  was created by sampling a  $\pi^0$  momentum distribution, obtained from Ref. [65, 44]. The  $\pi^0$  then decays into two back-to-back photons with a random orientation in the pion's center of mass frame.

The Bethe-Heitler differential cross-section for photons to produce a  $e^+e^-$  pair is found in the GEANT manual [66]. The cross section depends on the atomic number of the material, which was assumed to be mostly Silicon

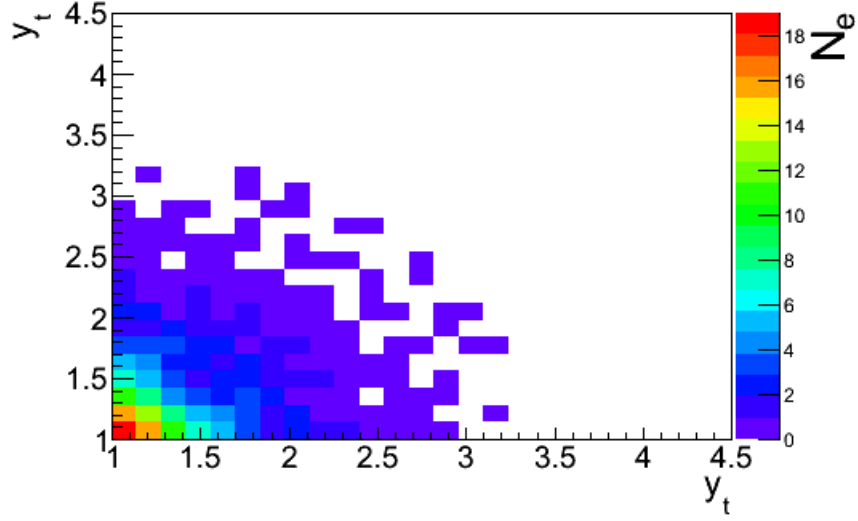


Figure 5.20: The simulated momentum distribution of electrons from photon conversion.

from the Silicon Vertex Tracker [67], the total energy of the photon in the lab frame, and the fraction of the photon energy  $\epsilon$  carried by one of the electrons. The distribution of the cross-section, integrated over all values of  $\epsilon$ , as a function of the total photon energy was used to either accept or reject potential  $\gamma \rightarrow e^+e^-$  decays. If the  $\gamma$  was accepted, then a value of  $\epsilon$  was determined from sampling a distribution of  $\epsilon$  for that particular total photon energy. The momentum distribution of 1150 correlated electron pairs is in Fig. 5.20.

The distribution should be normalized to the total number of correlated electron pairs in an event. This can be estimated from the 2D exponential component of the fit to US angular correlation data. This makes the assumption that the 2D exponential is only from pairs correlated from photon conversion

and therefore is most likely an overestimation.

The 2D exponential ( $F_{2D \text{ Exp}}$ ) is a function of  $\Delta\rho/\sqrt{\rho}$ . The number of correlated pairs ( $N_{e^+e^-}$ ) due to photon conversion equals  $\Delta\rho \times \Delta\eta\Delta\phi$ . The density of correlated particles ( $\Delta\rho$ ) is related to the 2D exponential fit function in the following expression:

$$F_{2D \text{ Exp}} = \sqrt{\rho_{ref,US}} \frac{\Delta\rho}{\rho_{ref,US}} (\eta_\Delta, \phi_\Delta) = A e^{-[\eta_\Delta^2/\sigma_{\eta_\Delta}^2 + \phi_\Delta^2/\sigma_{\phi_\Delta}^2]^{1/2}}. \quad (5.8)$$

The total number of correlated pairs is the 2D integral of Eq. 5.8

$$\int_0^{\Delta\eta} \int_{-\pi}^{\pi} d\eta_\Delta d\phi_\Delta \sqrt{\rho_{ref}} \frac{\Delta\rho}{\rho_{ref}} (\eta_\Delta, \phi_\Delta) = \frac{1}{2} \int_0^{\Delta\eta} \int_{-\pi}^{\pi} d\eta_\Delta d\phi_\Delta A e^{-[\eta_\Delta^2/\sigma_{\eta_\Delta}^2 + \phi_\Delta^2/\sigma_{\phi_\Delta}^2]^{1/2}}, \quad (5.9)$$

where the  $\frac{1}{2}$  on the right-hand-side is needed to compensate for the fact that both permutations of particles in a pair are taken in the analysis (i.e.  $\rho(\eta_\Delta, \phi_\Delta) = \rho(-\eta_\Delta, -\phi_\Delta)$ ). The limits of integration also take into account the specific permutations and reflections done in the analysis code.

The integral of a 2D exponential is calculated from the Gaussian integral and shown below.

$$\frac{1}{2} \int_0^{\Delta\eta} \int_{-\pi}^{\pi} d\eta_\Delta d\phi_\Delta A e^{-[\eta_\Delta^2/\sigma_{\eta_\Delta}^2 + \phi_\Delta^2/\sigma_{\phi_\Delta}^2]^{1/2}} = \frac{\pi}{2} A \sigma_{\eta_\Delta} \sigma_{\phi_\Delta} \quad (5.10)$$

Next,  $\Delta\rho$  needs to be extracted from the left-hand-side of Eq. 5.9. The integral of a ratio can be shown to equal approximately the ratio of integrals multiplied by the area of integration,  $\int \frac{x}{y} \approx \Omega \frac{\int x}{\int y}$ , if y is approximately constant. This relation is used in Eq. 5.11.

$$\begin{aligned}
\int \int d\eta_{\Delta} d\phi_{\Delta} \sqrt{\rho_{ref,US}} \frac{\Delta\rho}{\rho_{ref,US}} (\eta_{\Delta}, \phi_{\Delta}) &= \sqrt{\rho_{ref,US}} 2\pi \Delta\eta \frac{\int_0^{\Delta\eta} \int_{-\pi}^{\pi} d\eta_{\Delta} d\phi_{\Delta} \Delta\rho}{\int_0^{\Delta\eta} \int_{-\pi}^{\pi} d\eta_{\Delta} d\phi_{\Delta} \rho_{ref,US}} \\
&= \sqrt{\rho_{ref,US}} 2\pi \Delta\eta \frac{\int_0^{\Delta\eta} \int_{-\pi}^{\pi} d\eta_{\Delta} d\phi_{\Delta} \Delta N}{\int_0^{\Delta\eta} \int_{-\pi}^{\pi} d\eta_{\Delta} d\phi_{\Delta} N_{ref,US}} \quad (5.11)
\end{aligned}$$

The single particle density  $\sqrt{\rho_{ref}}$  is approximately  $\frac{d^2 N_{ch}}{d\eta d\phi}$ . One can assume that  $\sqrt{\rho_{ref,US}} = \frac{1}{\sqrt{2}} \left( \frac{d^2 N_{ch}}{d\eta d\phi} \right) = \frac{1}{\sqrt{2}} \frac{N_{ch}}{2\pi \Delta\eta}$  and the expression above can be further simplified.

$$\sqrt{\rho_{ref}} 2\pi \Delta\eta \frac{\int_0^{\Delta\eta} \int_{-\pi}^{\pi} d\eta_{\Delta} d\phi_{\Delta} \Delta N}{\int_0^{\Delta\eta} \int_{-\pi}^{\pi} d\eta_{\Delta} d\phi_{\Delta} N_{ref}} = \frac{N_{ch}}{\sqrt{2} 2\pi \Delta\eta} 2\pi \Delta\eta \frac{N}{\frac{1}{2} N_{ch}^2} = \frac{2N_e}{\sqrt{2} N_{ch}} \quad (5.12)$$

Equating the results of Eq. 5.10 and Eq. 5.12 per Eq. 5.9 leads to an expression for the total number of correlated electrons,  $N_e$ .

$$N_e = \frac{\pi}{2\sqrt{2}} N_{ch} A \sigma_{\eta_{\Delta}} \sigma_{\phi_{\Delta}} \quad (5.13)$$

In reality, the default prefactor for LS and US correlation measures is  $\sqrt{\rho_{ref,CI}}$ . Also, the  $\Delta\rho/\rho$  ratios for US charge combinations  $(+-, -+)$  are multiplied by a factor of  $\frac{1}{2}$  to transform the measure from a sum-of-ratios to a ratio-of-sums. So the US correlation measure is actually  $\sqrt{\rho_{ref,CI}} \frac{\Delta\rho}{2\rho_{ref,US}}$  and the number of electrons equals  $\frac{\pi}{2} N_{ch} A \sigma_{\eta_{\Delta}} \sigma_{\phi_{\Delta}}$ .

In the 18-28% centrality bin, the amplitude of the US 2D exponential is  $0.2698 \pm 0.0015$  with  $\sigma_{\eta_{\Delta}} = 0.1184 \pm 0.0011$  and  $\sigma_{\phi_{\Delta}} = 0.1304 \pm 0.0015$ . With



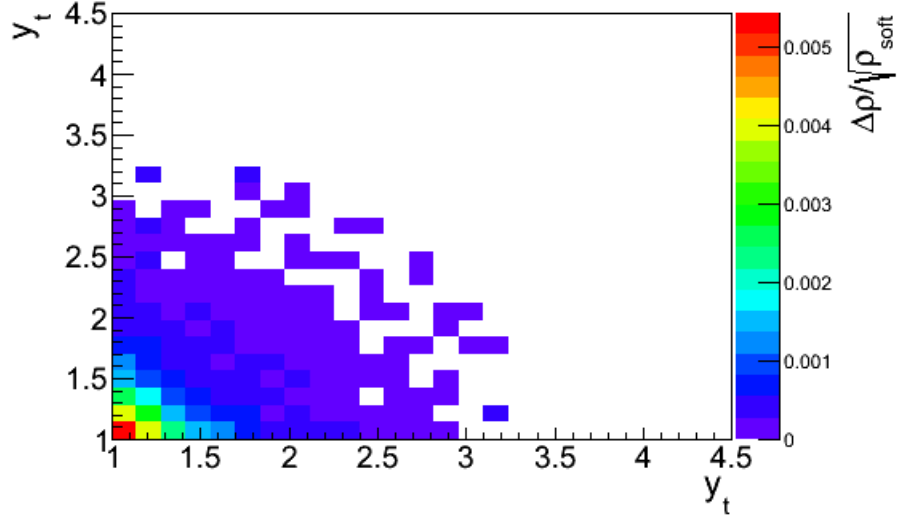


Figure 5.21:  $\Delta\rho/\sqrt{\rho_{soft}}$  for correlated electron pairs in the 18-28% centrality bin.

$N_{ch}=475.13$ , the number of unique pairs of correlated electrons is estimated to be  $3.11\pm0.05$ .

To match the data both permutations of a pairs  $(y_{t1}, y_{t2}) = (y_{t2}, y_{t1})$  should be taken. So the total number of electrons shown in Fig. 5.20 was scaled to 6.22 and expressed as the quantity  $\Delta\rho/\sqrt{\rho_{soft}}$ . This study demonstrated that correlated electrons from pair production are distributed primarily in the lower momentum region.

## 5.6 Discussion

This chapter presented comprehensive results of transverse momentum correlations for Au+Au 200 GeV collisions. The main feature observed in the

correlations is a broad peak extending from 0.5-4.0 GeV/ $c$ . This broad peak is observed in not only charge independent pairs but also both like- and unlike-sign charge combinations and same- and away-side relative azimuth angles.

Interestingly, this peak in the data for AS or “back-to-back” pairs persists in higher centralities, increases in amplitude, and remains at approximately the same transverse momentum. If this peak is related to jet physics then this observation does not support an opaque medium hypothesis. If an opaque, thermalized core is generated in central heavy ion collisions then one side of a di-jet should undergo significant energy loss known as “quenching” [19]. However, neither the position of the peak nor the amplitude in Fig. 5.3 decreases with an increase in centrality.

Two peaks are observed in the same-side unlike-sign data. These two peaks may correspond to a shift in the momentum distribution of pions and protons and be related to the observed increase of the proton-to-pion ratio in heavy ion collisions. The recombination model is one of the explanations of this enhancement and it assumes a formation of a partonic medium [68, 69]. Reference [7] claims, however, that the observed increase in the ratio of protons to pions in intermediate momentum ( $2 < p_t < 6$ ) in heavy ion collisions is due to a change in the jet fragmentation distribution.

The observations in all centralities and charge and angle combinations are quantified through fit models. The final fit model is based on a fluctuating soft component characterized by a 2D Levy distribution and higher momentum peak characterized by a 2D Gaussian. It is successful in describing most of

the features of the data.

The momentum correlation results also provide definitive tests for theoretical models. HIJING predicts a broad peak similar to data when jets are turned on, which suggests the peak is associated with semi-hard jet fragmentation. Partons in AMPT do not follow the observed trends when sufficient interaction strength is included to reproduce  $v_2$ . AMPT results also show a strong dissipation of the peak with a small increase in the parton-parton interaction strength. Comparisons to the NexSpheRIO model, which is based on hydrodynamics with fluctuating initial conditions, are also underway.

## Chapter 6

# The Momentum Dependence of Angular Correlations

All of the information contained in the available six-dimensional correlation space can be completely described in four dimensions  $(\eta_\Delta, \phi_\Delta, y_{t1}, y_{t2})$ , given the two-particle distribution is stationary on  $\eta_\Sigma$  and  $\phi_\Sigma$ . This chapter presents measurements binned on these four variables by forming angular correlations as a function of  $(y_{t1}, y_{t2})$ . This will determine how pairs correlated in a specific angular structure are distributed in momentum. The momentum distribution of pairs in the same-side peak, for example, has the potential to support or falsify the idea that the “ridge” and “jet” are two separate processes.

### 6.1 Analysis Setup

A comprehensive study of the momentum dependence of angular correlations began by dividing pairs into unique regions in momentum space, known as “cut bins”, according to their  $(y_{t1}, y_{t2})$  values. The correlations of the pairs from each cut bin were then formed in angular space and analyzed.

The size of a cut bin was made large enough to provide ample statistics

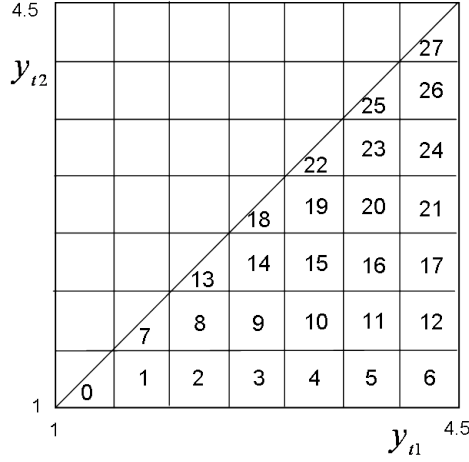


Figure 6.1: The locations of the 28 unique cut bins in  $(y_{t1}, y_{t2})$  space for the present study. Both permutations of a pair were taken but only one half of the  $(y_{t1}, y_{t2})$  space was filled due to an inherent symmetry.

but small enough to provide an adequate resolution of the resulting structures. The final design consisted of 28 distinct cut bins in the range of  $(y_{t1}, y_{t2}) = ([1, 4.5], [1, 4.5])$  for each of the eleven centralities. The bins were square with sides of length 0.5 as seen in Fig. 6.1. Both permutations of particles in a pair were counted and therefore the  $(y_{t1}, y_{t2})$  space is symmetric by construction along the diagonal ( $y_{t1} = y_{t2}$ ). This symmetry permitted filling only one half of the  $(y_{t1}, y_{t2})$  space and therefore the bins located along the diagonal are only half the nominal bin size.

## 6.2 Weighting

The goal of this study is to determine how the relative number of *pairs* correlated in a specific angular structure are distributed in momentum space.

However, the correlation signal,  $\Delta\rho/\sqrt{\rho_{ref}}$ , measures the number of correlated pairs *per particle*. The denominator introduces a dependence on the number of particles in each cut bin. This dependence will be removed in order to measure a quantity which can be directly compared between momentum regions.

An effective weighting factor  $w_i$  can be constructed that effectively creates a common denominator. The common denominator,  $\rho_{ref,tot}$ , is the  $p_t$  integral density of pairs. With this weighting, the sum of the angular bin content from each of the 28  $(y_{t1}, y_{t2})$  bins would be equal to the angular bin content from a  $p_t$  integral analysis as in the following expression

$$\left[ \frac{\Delta\rho}{\sqrt{\rho_{ref}}} \right]_{\text{All } y_t} \approx \sum_i w_i \left[ \frac{\Delta\rho}{\sqrt{\rho_{ref}}} \right]_i, \quad (6.1)$$

where  $i$  denotes a 2D bin in  $(y_{t1}, y_{t2})$  space.

However, a more precise relationship between the  $i = 28$  bins and the  $p_t$  integrated value is expressed in Eq. 6.2 and uses the definitions  $n_{sib} \equiv \sum_i n_{sib,i}$  and  $n_{ref} \equiv \sum_i n_{ref,i}$ .

$$\begin{aligned} \left[ \frac{\Delta\rho}{\rho} \right]_{total} &= \frac{n_{sib}(\eta_\Delta, \phi_\Delta) - \frac{N_{sib}}{N_{ref}} n_{ref}(\eta_\Delta, \phi_\Delta)}{\frac{N_{sib}}{N_{ref}} n_{ref}(\eta_\Delta, \phi_\Delta)} \\ &= \frac{\sum_i n_{sib,i}(\eta_\Delta, \phi_\Delta) - \frac{N_{sib}}{N_{ref}} \sum_i n_{ref,i}(\eta_\Delta, \phi_\Delta)}{\frac{N_{sib}}{N_{ref}} \sum_i n_{ref,i}(\eta_\Delta, \phi_\Delta)} \end{aligned} \quad (6.2)$$

$N$  is the total number of pairs in the full  $(\eta, \phi)$  acceptance and  $n$  is the number of pairs in one  $(\eta_\Delta, \phi_\Delta)$  bin for sibling or reference pairs. The factor  $\frac{N_{sib}}{N_{ref}}$  normalizes the number of mixed pairs via pair weighting.

First, the three summations over  $i$  in Eq. 6.2 are combined into one sum over the ratio  $\Delta\rho/\rho$ .

$$\begin{aligned}
\left[\frac{\Delta\rho}{\rho}\right]_{total} &= \frac{\sum_i \frac{N_{sib}}{N_{sib}} \frac{N_{ref}}{N_{ref}} \frac{n_{ref,i}}{n_{ref,i}} n_{sib,i} - \frac{N_{sib}}{N_{ref}} \sum_i n_{ref,i}}{\frac{N_{sib}}{N_{ref}} n_{ref}} \\
&= \frac{\frac{N_{sib}}{N_{ref}} \sum_i n_{ref,i} \left( \frac{N_{ref}}{N_{sib}} \frac{n_{sib,i}}{n_{ref,i}} - 1 \right)}{\frac{N_{sib}}{N_{ref}} n_{ref}} \\
&= \sum_i \frac{n_{ref,i}}{n_{ref}} \left( \frac{N_{ref}}{N_{sib}} \frac{n_{sib,i}}{n_{ref,i}} - 1 \right) \tag{6.3}
\end{aligned}$$

Ultimately, the expression above will need to contain the quantity actually measured in the analysis code, which is

$$\left[\frac{\Delta\rho}{\rho}\right]_i = \frac{n_{sib,i} - \frac{N_{sib,i}}{N_{ref,i}} n_{ref,i}}{\frac{N_{sib,i}}{N_{ref,i}} n_{ref,i}}. \tag{6.4}$$

The normalization factor used in each cut bin,  $\frac{N_{sib,i}}{N_{ref,i}}$ , needs to be replaced with the normalization factor for the entire  $p_t$  integrated data sample. The expanded expression is

$$\begin{aligned}
\left[\frac{\Delta\rho}{\rho}\right]_{total} &= \sum_i \frac{n_{ref,i}}{n_{ref}} \left[ \frac{N_{ref}}{N_{sib}} \frac{N_{sib,i}}{N_{ref,i}} \left( \frac{N_{ref,i}}{N_{sib,i}} \frac{n_{sib,i}}{n_{ref,i}} \right) - 1 \right] \\
&= \sum_i \frac{n_{ref,i}}{n_{ref}} \left[ \frac{N_{ref}}{N_{sib}} \frac{N_{sib,i}}{N_{ref,i}} \left( \left[\frac{\Delta\rho}{\rho}\right]_i + 1 \right) - 1 \right] \\
&\equiv \sum_i \frac{\Delta\rho_i}{\rho_{ref,tot}}, \tag{6.5}
\end{aligned}$$

where  $\left[\frac{\Delta\rho}{\rho}\right]_i$  is defined in Eq. 6.4. The relationship between the correlation measure in each cut bin and the correlation measure of a  $p_t$  integrated analysis is now given in Eq. 6.5.

### 6.3 Fitting Procedure

Information contained in the 28 weighted  $(y_{t1}, y_{t2})$  bins in 11 centralities can be extracted and quantified via fitting. The six model components used in  $p_t$  integrated analyses [11] are defined in Eq. 6.6. As a first step, this fitting model was applied to each of the cut bins, with the expectation that some adjustments would be required due to the momentum restrictions.

$$\begin{aligned}
F = & A_1 \exp \left\{ -\frac{1}{2} \left[ \left( \frac{\phi_\Delta}{\sigma_{\phi_\Delta}} \right)^2 + \left( \frac{\eta_\Delta}{\sigma_{\eta_\Delta}} \right)^2 \right] \right\} \\
& + A_D \cos(\phi_\Delta - \pi) \\
& + A_Q \cos(2\phi_\Delta) + A_0 \exp \left\{ -\frac{1}{2} \left( \frac{\eta_\Delta}{\sigma_0} \right)^2 \right\} \\
& + A_2 \exp \left\{ - \left[ \left( \frac{\phi_\Delta}{w_{\phi_\Delta}} \right)^2 + \left( \frac{\eta_\Delta}{w_{\eta_\Delta}} \right)^2 \right]^{1/2} \right\} + A_3 \quad (6.6)
\end{aligned}$$

The correlation data were fit with ROOT's software package, Minuit. Minuit's default fitting algorithm, MIGRAD, uses information about the first derivatives of  $\chi^2$  with respect to the fitting parameters to find the minimum  $\chi^2$  value [70]. The user is also able to start MIGRAD at a specific location in the N-dimensional parameter space and impose limits on each of the parameters.

MIGRAD calculates a  $1\sigma$  error on each parameter by varying each parameter independently until the  $\chi^2$  value increases by one. It likely underestimates the error because it assumes there is no covariance between parameters. A better error estimation is done with the processor MINOS. MINOS will vary each parameter simultaneously and refit until the  $\chi^2$  value increases by one.



The first step in the fitting procedure for the present analysis was to fit the data using MIGRAD. This is a quick way to locate the  $\chi^2$  minimum. The data are then re-fit with MINOS, starting at the location given by MIGRAD, to get a better estimation of the errors. The ranges in which the parameters were allowed to vary were kept as wide as possible to help the fitting algorithms (i.e. calculation of the first derivative) and error calculations. There were instances in which limitations to the parameter ranges were required. This was most often needed when structures in the data vanished and the corresponding fitting components tried to model other features of the data.

Another fitting algorithm called Downhill Simplex [71] was used to evaluate the validity of the MIGRAD fit results. The Simplex algorithm, while slower than MIGRAD, is more robust due to the fact that it does not rely on first derivatives [70]. The Simplex method is also advantageous for its ability to identify local minima in the  $\chi^2$  contour map, due to its frequent inability to locate the global minimum. Often the Simplex fitter ends at a local minimum or some other intermediate stage. The fitting results are highly dependent on the location in parameter space in which the fitting begins. Therefore if one takes a large sample of random starting values, the  $\chi^2$  distribution of the final fit parameters will contain a detailed map of local and global minima. The results from ROOT's fit to the data were compared to these  $\chi^2$  distributions and any inconsistencies were marked for further examination. The following subsections will detail situations in which the standard fitting model defined in Eq. 6.6 was not adequate.

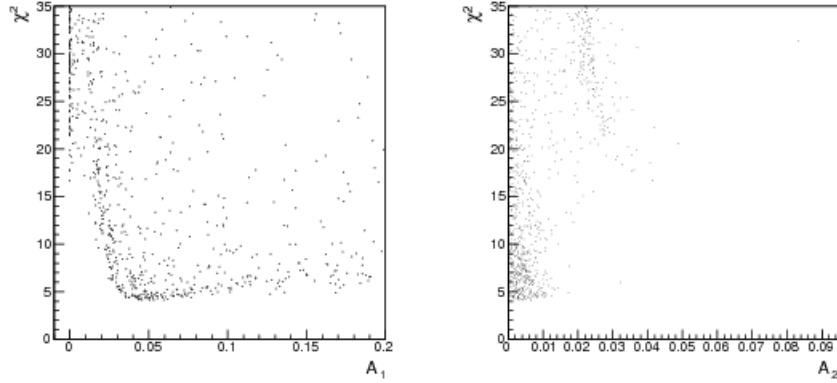


Figure 6.2: Scatter plot of 500 Simplex fit results for centrality 5-9% in the range  $y_{t1} = [3, 3.5]$  and  $y_{t2} = [2, 2.5]$  (cut bin 15). Each fit was started at a random location in the 11-dimensional parameter space. Left Panel:  $\chi^2$  versus 2D Gaussian amplitude. Right Panel:  $\chi^2$  versus 2D exponential amplitude.

### 6.3.1 2D Exponential

The  $\chi^2$  map in Fig. 6.2, generated by the Simplex algorithm, shows evidence of two parameters covarying due to an unsuitable fitting model. The left panel shows a scatter plot containing values of  $\chi^2$  versus the 2D Gaussian amplitude for 500 fits and the right panel shows the  $\chi^2$  values versus the 2D exponential amplitudes.

In this momentum range,  $y_{t1} = [3, 3.5]$  and  $y_{t2} = [2, 2.5]$ , there is no observed 2D exponential component in the angular correlation data. Therefore, the standard fit model is now overdetermined and the 2D Gaussian and 2D exponential compete to fit one same-side peak. The two bands of points at amplitude values of 0 and 0.04 in Fig. 6.2 correspond to the two situations in which either the exponential or the Gaussian fit the same-side peak. The

solution to this fitting ambiguity is to remove the 2D exponential in the cut bins in which a sharp peak is not directly observed in the data.

The 2D exponential component was removed from the fit in 14 cut bins (6, 10-12, 16, 17 and 19-26). These cut bins are located in the higher momentum region where there is a large relative difference in the momentum of the particles in a pair. The 2D exponential contains correlated particles from photon conversion in detector material as well as HBT, Coulomb repulsion, or other short range momentum correlations. Studies have shown the electron pairs from photon conversion are distributed in mostly the lower momentum region along the diagonal ( $y_{t1} \approx y_{t2}$ ) (see Sec. 5.5.3). Therefore the disappearance of this structure in these cut bins is not surprising.

### 6.3.2 Quadrupole

Due to these simplex results, peculiarities with the quadrupole component in some of the cut bins were identified. Figure 6.3 contains a plot of  $\chi^2$  values versus quadrupole amplitudes for 10,000 starting values. A reasonable judgment of the  $\chi^2$  minimum would be at a quadrupole amplitude of approximately 0.0085. However MIGRAD returns a value of 0.0015.

The residual from the MIGRAD fit is small, however, so the observed discrepancy in the quadrupole amplitude must be compensated by other fit components. Perhaps the dipole, quadrupole, and/or 2D Gaussian were conspiring to fit the structures in the data. This discrepancy between the simplex and MIGRAD fit results appeared in the higher centrality fractions of cut bins

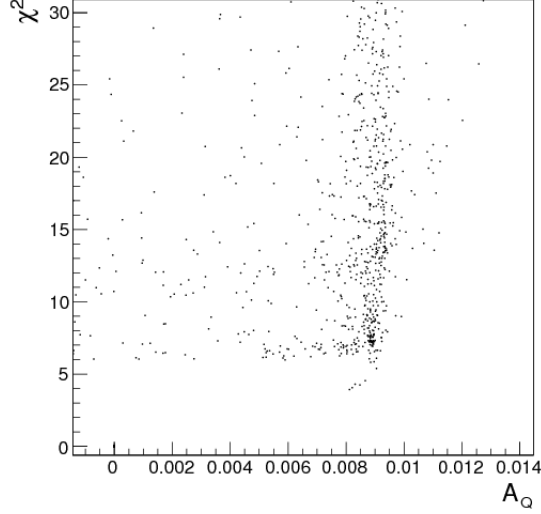


Figure 6.3: Scatter plot of the  $\chi^2$  versus quadrupole amplitude for 10,000 Simplex fits with random starting locations for 10-18% central events in the range  $y_{t1} = y_{t2} = [1.5, 2]$  (cut bin 7).

1, 2, 5, 7-9, and 13.

Interestingly, adding the quadrupole amplitudes from fits to LS and US data separately matched the CI quadrupole amplitude determined from the Simplex results. This resolved the fitting ambiguity and the CI data were then fit with a fixed quadrupole amplitude.

### 6.3.3 Negative Like-sign Dip

Correlations in some cut bins developed a negative dip at the origin which does not appear in  $p_t$  integrated results. Also, this negative dip was present in only LS pairs as seen in Fig. 6.4. In some cut bins this LS negative dip was hidden by a larger, positive structure in US pairs and therefore did

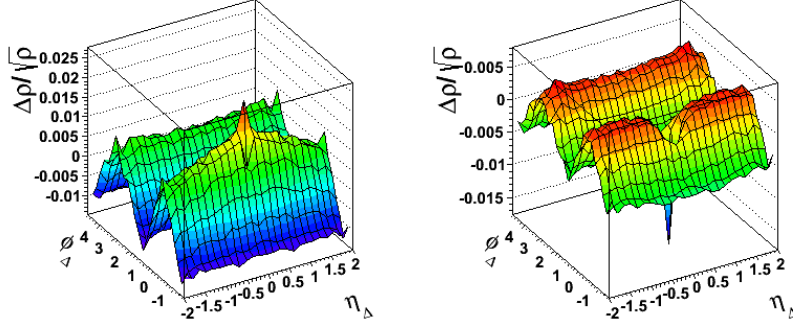


Figure 6.4: Charge independent (left) and like-sign (right) angular correlations in the range  $y_{t1} = [2, 2.5]$  and  $y_{t2} = [1, 1.5]$  (cut bin 2) and centrality fraction 9-18%

not appear in CI correlations. In any case, this new correlation feature needed to be properly addressed with the fit model.

The negative dip in LS pairs was identified in cut bins 1-4, 8-10, 14-16, 18, 19, 22 and 23 and fit with a negative 2D exponential. The negative 2D exponential was then subtracted from the CI data before proceeding with the standard fitting routine.

Generally LS pairs contain positive correlations from HBT near the origin. HBT occurs between identical particles with similar relative velocity so it is observed mainly along the  $y_{t1} \approx y_{t2}$  diagonal. This negative dip appeared in pairs with a larger difference in momentum and therefore the HBT signal is too small to conceal a negative dip. The negative correlation may be due to Coulomb repulsion between like-sign charged particles or a result of hadronization.

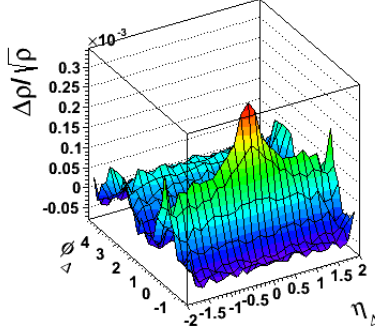


Figure 6.5: CI angular correlations in the range  $y_{t1} = y_{t2} = [3.5, 4.0]$  (cut bin 25) and centrality fraction 9-18%.

#### 6.3.4 Same-side Peak Gaussian(s)

The 2D Gaussian fitting component, which describes the same-side peak, required adjustments in the higher  $(y_{t1}, y_{t2})$  bins. In these cut bins there is no significant 2D exponential component due to the small contributions from electrons, HBT, or other possible small range correlations.

The same-side peak in cut bins 23-25 deviated from a single Gaussian shape as seen in Fig. 6.5. This new structure was found to be described well by two 2D Gaussian functions, one wide in  $\eta_\Delta$  and the other narrow. The same-side peak was then represented by the sum of these two components.

#### 6.3.5 Higher Order Fourier Components

The fitting function defined for this analysis contains only the required components to produce a statistically negligible residual. However, higher order harmonics such as  $v_n = \langle \cos(n[\phi - \psi_n]) \rangle$  ( $n=3,4,\dots$ ) have been claimed

to be significant [72]. The amplitudes of these proposed higher order harmonics can, in fact, be directly obtained from the 11 parameter 2D fit results in Eq. 6.6. This is due to the fact that the only available structure for higher order Fourier components to describe is that which has already been described to the statistical limits of the data with one of the six original components. For more detail on this refer to Appendix B of Ref. [11].

## 6.4 Results

The fitting results in 28 cut bins and 11 centralities need to now be meaningfully displayed. For a  $p_t$  integral analysis, if the fit model completely describes the features in the data (i.e. there is no structure in the residual) then the approximation

$$\sqrt{\rho'_{ref}} \frac{\Delta\rho}{\rho_{ref}}(\eta_{\Delta}, \phi_{\Delta})_{all,y_t} \approx \sum_k f_k(\eta_{\Delta}, \phi_{\Delta}) \quad (6.7)$$

is valid, where  $f_k$  represent the six fitting components: offset, dipole, quadrupole, 2D Gaussian, 2D exponential, and 1D Gaussian.

The weighting procedure described in Sec. 6.2 ensured the sum of the bin content from each of the 28 bins added up to the bin content in the  $p_t$  integral result. Similarly the summation of the fitting components in each of the 28 bins should equal the  $p_t$  integral data

$$\sqrt{\rho'_{ref}} \frac{\Delta\rho}{\rho_{ref}}(\eta_{\Delta}, \phi_{\Delta})_{all,y_t} \approx \sum_i \sum_k f_{k,i}(\eta_{\Delta}, \phi_{\Delta}), \quad (6.8)$$

where subscript  $i$  denotes a 2D bin in  $(y_{t1}, y_{t2})$  space.

The magnitudes of the fit components,  $f_{k,i}$ , represent the number of correlated pairs ( $\Delta\rho$ ) in an angular correlation feature per final state particle ( $\sqrt{\rho_{ref,tot}} = d^2N/d\eta d\phi$ ). However, the number of correlated pairs in each bin  $i$  is dependent on the number of available particles in that  $(y_{t1}, y_{t2})$  range. To remove this dependency the denominator is replaced with a measure of the number of final state particles on  $y_t$  and the expression becomes

$$\frac{d^2N/d\eta d\phi}{\sqrt{\rho'_{ref,i}(y_{t1}, y_{t2})}} f_{k,i}(\eta_\Delta, \phi_\Delta), \quad (6.9)$$

where  $d^2N/d\eta d\phi$  is the  $p_t$  integrated value and  $\sqrt{\rho'_{ref,i}(y_{t1}, y_{t2})} = \sqrt{\frac{d^2N_{tot}}{dy_{t1} dy_{t2}}}$  or  $\sqrt{\frac{d^2N_{soft}}{dy_{t1} dy_{t2}}}$ . The quantity in Eq. 6.9 is now the number of correlated pairs in  $k^{th}$  angular correlation feature, for pairs in  $(y_{t1}, y_{t2})$  bin  $i$ , per final state particle on  $y_t$ .

For the offset, dipole, and quadrupole the amplitude is the relevant quantity for  $f_k$ . For the 1D and 2D Gaussian and the 2D exponential the volumes are more appropriate measures because the widths also change as a function of momentum. This chapter will present the measure in Eq. 6.9 using a soft reference  $\left(\sqrt{\rho'_{ref}} = \frac{d^2N_{soft}}{dy_{t1} dy_{t2}}\right)$ . The amplitudes or volumes will be mapped onto a 2D  $(y_{t1}, y_{t2})$  distribution that corresponds to the momentum range of the original pair sample.

### 6.4.1 Dipole

The momentum distributions of the dipole amplitude are displayed in Fig. 6.6 for 11 centralities with a common z-axis scale. The peak of the dis-



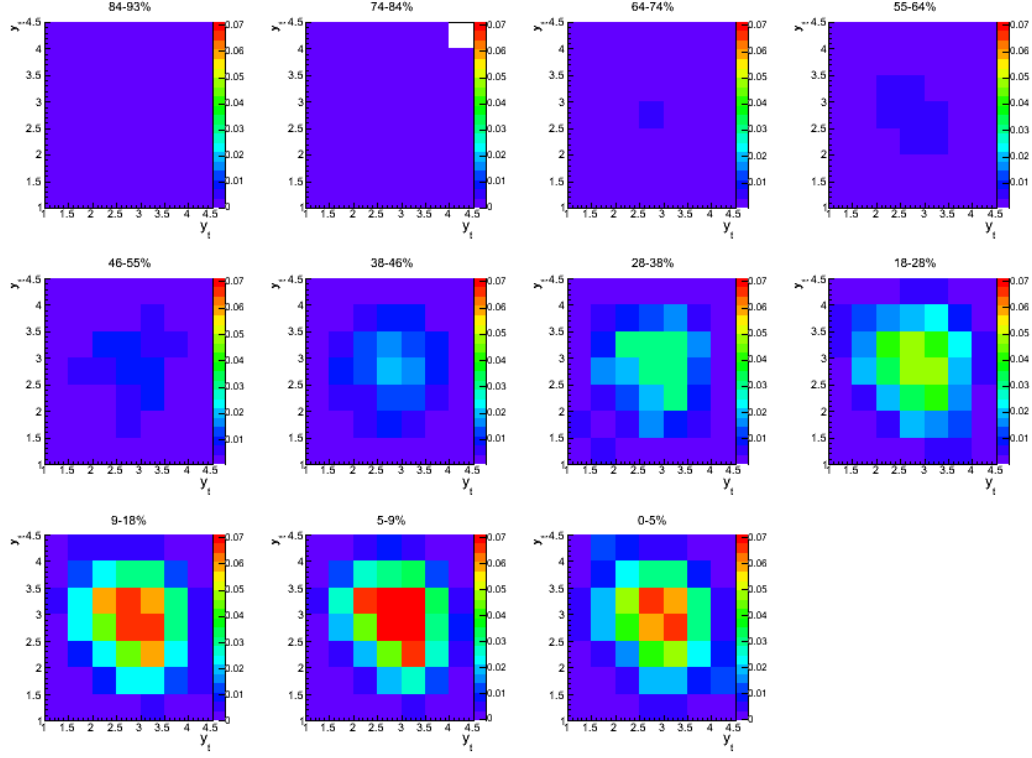


Figure 6.6: The amplitude of the dipole component on  $(y_{t1}, y_{t2})$  in 11 centralities for Au+Au 200 GeV collisions.

tribution is around  $(y_{t1}, y_{t2}) = (3, 3)$ , similar to the two-particle momentum correlations  $\frac{\Delta\rho}{\sqrt{\rho}}(y_t, y_t)$  in Chap. 5. The amplitude of the peak increases with centrality but the position remains constant.

### 6.4.2 Quadrupole

The momentum distributions of the quadrupole amplitude are displayed in Fig. 6.7. Most of the pairs are distributed also near  $(y_{t1}, y_{t2}) = (3, 3)$ . The amplitude of the distribution peaks in the mid-central collisions and then

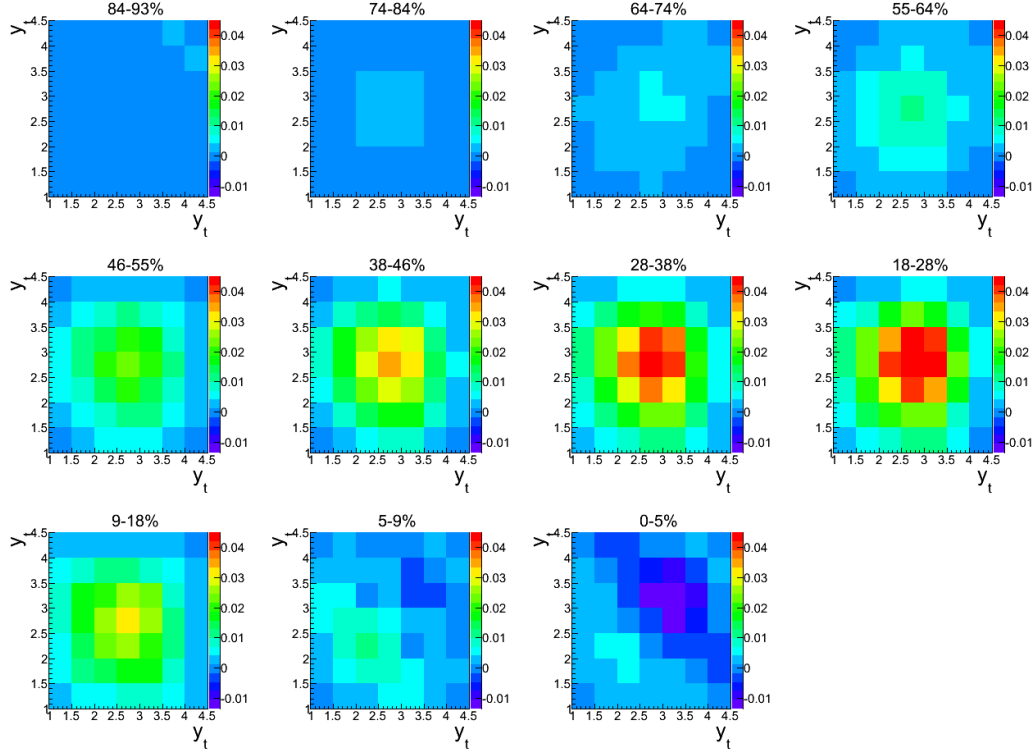


Figure 6.7: The amplitude of the quadrupole component on  $(y_{t1}, y_{t2})$  in 11 centralities for Au+Au 200 GeV collisions.

decreases to approximately zero at the most central collisions. The position of the peak, however, appears to remain constant.

### 6.4.3 1D Gaussian

The momentum distributions of the 1D Gaussian volume on  $\eta_\Delta$  are displayed in Fig. 6.8. Only the four most peripheral centralities are presented because a 1D Gaussian structure is not observed in more central data. The distribution is peaked in the lowest  $(y_t, y_t)$  bin and the amplitude of the peak

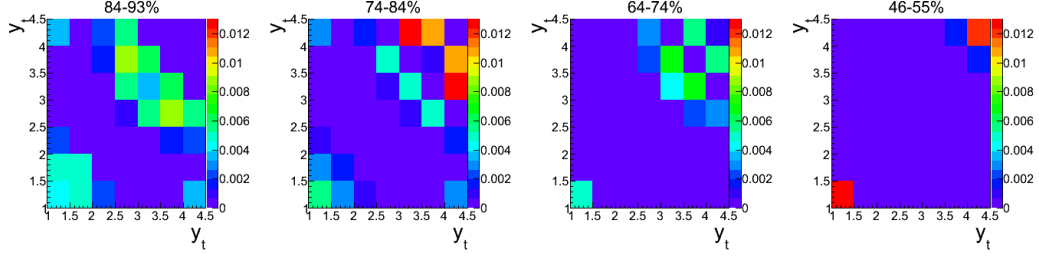


Figure 6.8: The volume of the 1D Gaussian on  $\eta_{\Delta}$  on  $(y_{t1}, y_{t2})$  in 4 centralities, increasing left-to-right, for Au+Au 200 GeV collisions.

decreases with centrality. A large 1D Gaussian volume is reported in the higher momentum region due to a fitting ambiguity in which the 1D Gaussian width increases significantly and the entire structure becomes equivalent to an offset.

#### 6.4.4 2D Exponential

The momentum distributions of pairs correlated in the 2D exponential component are displayed in Fig. 6.9. The empty  $(y_t, y_t)$  bins correspond to momentum regions in which the 2D exponential was removed from the fitting function. Pairs correlated in the 2D exponential are distributed in the low momentum region and at  $y_{t1} \approx y_{t2}$ . The 2D exponential in some of the higher momentum cut bins is very narrow which causes fit instabilities that result in a large reported volume.

#### 6.4.5 2D Gaussian(s)

The same-side peak is described with either one or two 2D Gaussian functions. The momentum distributions of pairs correlated in the Gaussian(s)

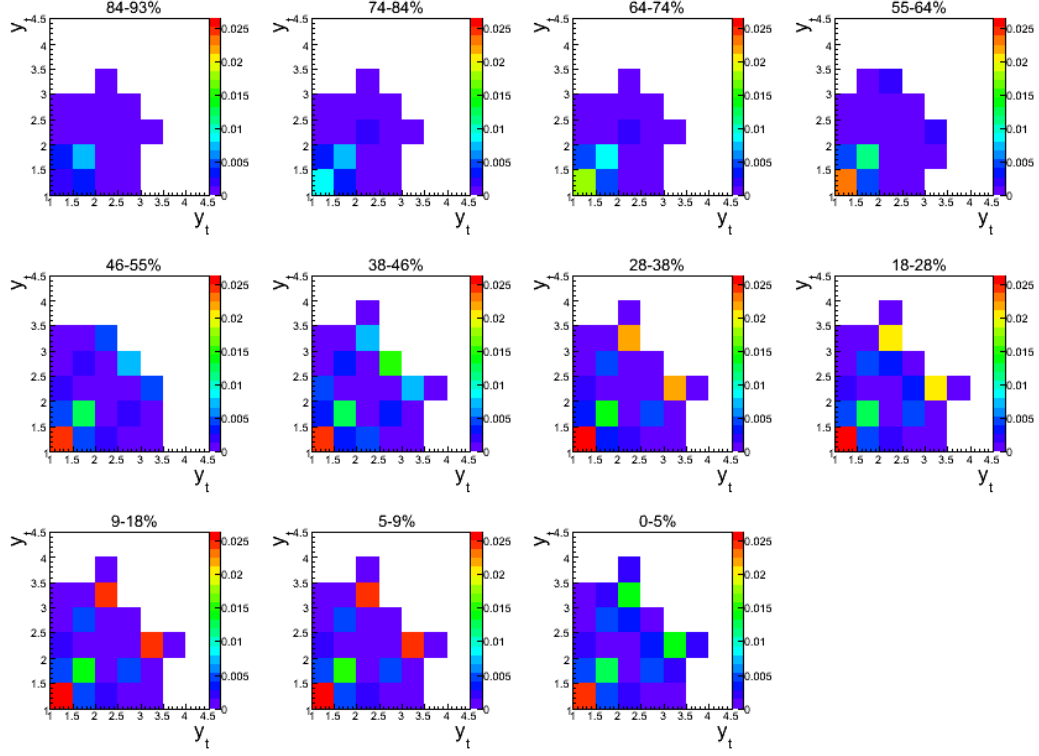


Figure 6.9: The volume of the 2D exponential on  $(y_{t1}, y_{t2})$  in 11 centralities for Au+Au 200 GeV collisions.

are displayed in Fig. 6.10. The distributions are peaked around  $(y_{t1}, y_{t2}) = (3, 3)$  in all centralities and the amplitude increases with centrality.

More detailed information about the peak position and widths were obtained by projecting the data onto the  $y_{t\Sigma}$  and  $y_{t\Delta}$  axes and then fitting with a 1D Gaussian. An alternative method to obtaining the peak position and widths would be to calculate the mean and variance of the distribution directly. However, there are data points at the tail (large  $y_t$ ) with large error bars due to poor statistics. The size of the error bars are not taken into account

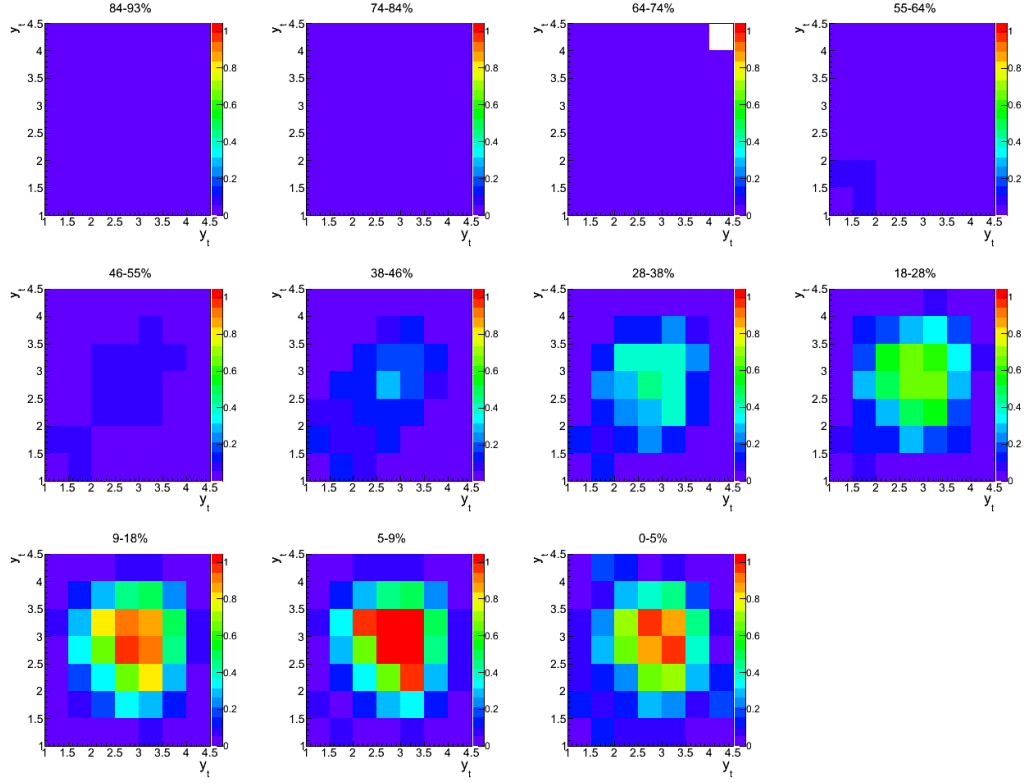


Figure 6.10: The volume of the 2D Gaussian(s) on  $(y_{t1}, y_{t2})$  in 11 centralities for Au+Au 200 GeV collisions.

when calculating the mean and variance directly, unlike in a fit.

The fits along the  $y_{t\Sigma}$  axis are displayed with the data in the upper panels of Fig. 6.11. The error bars represent the MINOS fitting errors which are dependent on the statistical error of the data. The amplitudes of the Gaussians in the left-lower panel appear to increase with centrality above binary scaling. The widths in the middle-lower panel generally vary between 0.5 and 1. The right-lower panel shows the position of the peak stabilizes around  $y_t=3$  in the six most central bins. Interestingly, the position and width of the 1D

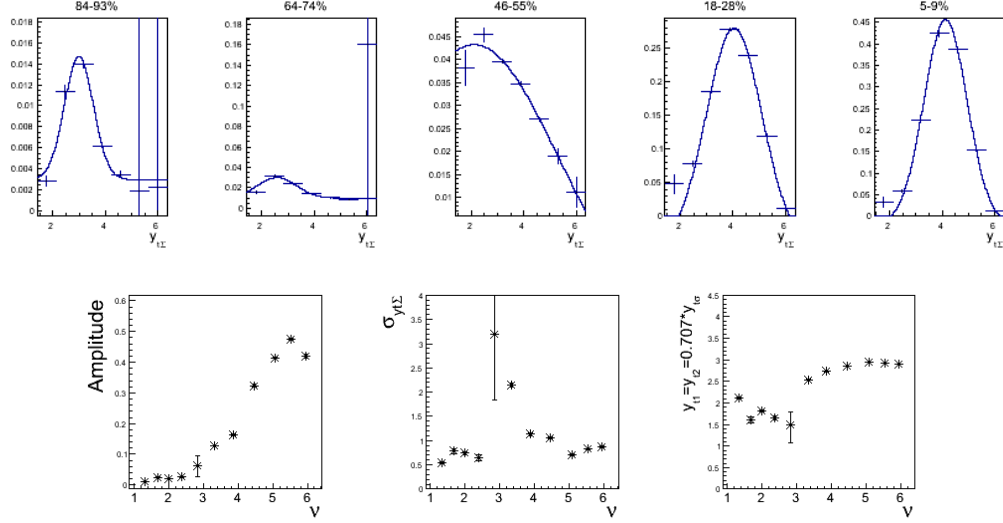


Figure 6.11: Upper panels: Projections of the momentum distribution of the 2D Gaussian(s) on the  $y_{t\Sigma}$  axis for five centralities with a 1D fit in blue. Lower panels: The 1D Gaussian amplitude (left), width (center) and position (right) of the fit to the projections as a function of  $\nu$  for 11 centralities.

Gaussian deviates from the general trends in the 46-55% centrality, where a sharp transition is observed to occur in  $p_t$ -integral angular correlations.

The fits along the  $y_{t\Delta}$  axis are displayed with the data in the upper panels of Fig. 6.12. The amplitudes of the Gaussians in the left-lower panel appear to increase with centrality above binary scaling like in Fig. 6.11. The widths in the middle-lower panel vary between 1 and 1.5. In the right-lower panel the position of the peak as a function of centrality is shown to be consistently 0, which is purely a consequence of the data being symmetric about the  $y_{t\Sigma}$  axis by construction.

Some analyses define  $\eta_\Delta$  cuts to form two regions, a “jet-like” region

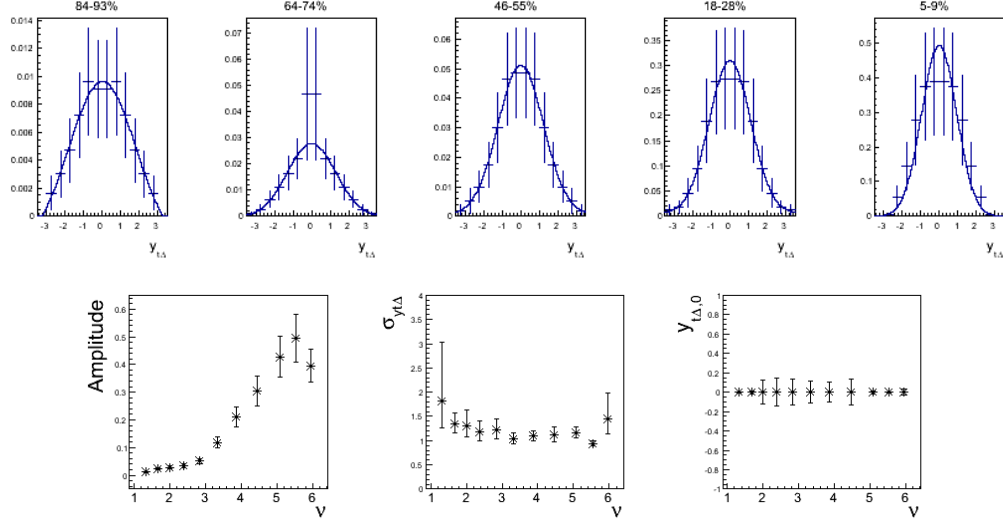


Figure 6.12: Upper panels: Projections of the momentum distribution of the 2D Gaussian(s) on the  $y_{t\Delta}$  axis for five centralities. Lower panels: The 1D Gaussian amplitude (left), width (center), and position (right) of the fit to the projections as a function of  $\nu$  for 11 centralities.

close to the origin and a “bulk-like” region at larger values of  $\eta_{\Delta}$ . The properties of the pairs in the two regions are often interpreted as originating from two separate processes [20]. The present analysis is useful in its ability to measure the momentum distribution of pairs which *only* contribute to the “ridge” or “jet” structures.

The same-side 2D Gaussian(s) were divided into three sections along  $\eta_{\Delta}$  of equal length. The momentum distributions of the pairs in each of these three ranges are displayed in Fig. 6.13.

Since the  $\eta$  elongation of the same-side peak only appears in mid- to most-central events, Fig. 6.13 contains only the five most-central centralities.

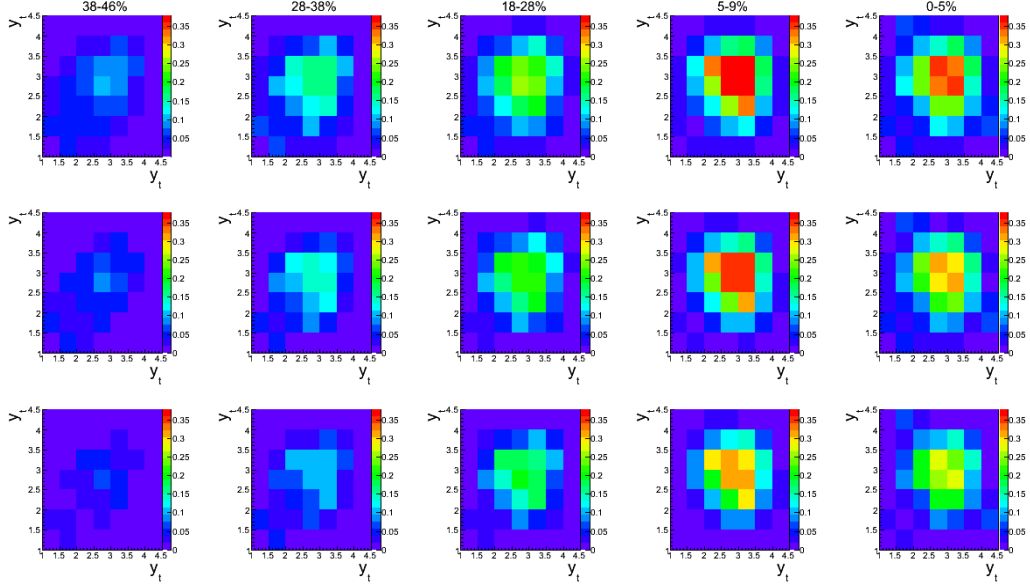


Figure 6.13: The volume of the 2D Gaussian(s) on  $(y_{t1}, y_{t2})$  in three  $\eta_\Delta$  regions (rows) in five centralities (columns). The  $\eta_\Delta$  regions from top to bottom are  $|\eta_\Delta| < 2/3$ ,  $2/3 < |\eta_\Delta| < 4/3$  and  $4/3 < |\eta_\Delta| < 2$ .

The pairs correlated near the origin in the upper panels are distributed in momentum around  $(y_{t1}, y_{t2}) = (3, 3)$ . As the integration region moves to larger values of  $\eta_\Delta$  (middle and bottom row) the peak position of this distribution does not change.

## 6.5 Discussion

This study's ability to measure the momentum distribution of pairs which contribute only to specific angular correlation features is very informative. It contrasts with other analyses that impose  $\eta_\Delta$  cuts,  $p_t$  triggering requirements or ZYAM [73] background subtraction techniques in order to



measure momentum information about angular correlation features, such as the ridge [74].

The momentum distribution of the correlated pairs in the same-side structure is peaked around  $(y_{t1}, y_{t2}) = (3, 3)$  in peripheral collisions. HIJING predictions support the hypothesis that this same-side peak structure, especially near the angular origin, is due to jet fragmentation. As centrality increases the peak amplitude increases and the position remains relatively constant. Surprisingly, the dipole component, which is hypothesized to be the di-jet away-side follows the same trends as the same-side peak. These findings do not support an opaque core hypothesis in which di-jet correlations are strongly suppressed from interactions with the medium and dissipation is expected on the away-side.

Also, the correlated pairs in the  $\eta$  elongated portion of the same-side peak structure appear to come from roughly the same distribution as pairs in the center near  $\eta_{\Delta} = 0$ . This does not support the claim in the literature that the “ridge” is coming from “bulk” correlations which are expected to have a lower average momentum than pairs coming from “jet” correlations [74].

The momentum distribution of pairs correlated in the quadrupole, 1D Gaussian, and 2D exponential were also measured. The pairs correlated in the quadrupole component are distributed around  $(y_{t1}, y_{t2}) = (3, 3)$  in all centralities. The pairs correlated in the 1D Gaussian structure are distributed in the lower momentum region and the amplitude of the distribution decreases with centrality. This follows the expectations from PYTHIA which suggests

that the 1D Gaussian is due to soft longitudinal fragmentation as described in Sec. 4.2. The momentum distribution of pairs correlated in the 2D exponential are also distributed at low momentum which agrees with simulation studies of photon conversion electrons presented in Sec. 5.5.3.

### 6.5.1 Comparison to a Similar Analysis

The results from the present analysis can compare directly to those reported in Ref. [13]. In [13], a marginal distribution of two-particle correlations ( $\Delta\rho/\rho$ ) were formed from Au+Au 200 GeV data by restricting the  $p_t$  of one of the particles, similar to “triggered” analyses. These data were then fit with the standard fit function, excluding the 2D exponential.

The first  $y_t$  bin was defined as  $y_t=[1,1.4]$  and the seven subsequent bins were 0.4 units of  $y_t$  wide. The last bin contained particles with a  $y_t$  greater than 4.2. This distribution is similar to summing square  $(y_{t1}, y_{t2})$  bins along the 7 columns and rows with a common  $y_t$  value as seen in Fig. 6.14.

The process of relating the two measurements will be made easier by defining a ratio  $\hat{r}$ , which is the normalized ratio of sibling to reference pairs. The measurement,  $\hat{r}_j$ , in Ref. [13] is

$$\left[ \frac{\Delta\rho}{\rho_{ref}} \right]_j = \hat{r}_j - 1 = \frac{N_{ref,j}}{N_{sib,j}} \frac{n_{sib,j}}{n_{ref,j}} - 1, \quad (6.10)$$

where upper case  $N$  is the total number of pairs in the full  $(\eta, \phi)$  acceptance, lower case  $n$  indicates the number of pairs in one  $(\eta_\Delta, \phi_\Delta)$  bin for sibling or reference pairs, and  $j$  indicates the column in  $(y_{t1}, y_{t2})$  space. The sum of the

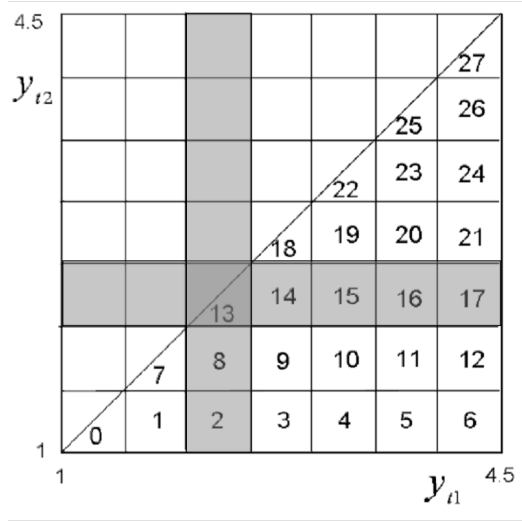


Figure 6.14: The analysis in Ref. [13] forms a marginal distribution equivalent to symmetric stripes in the present 2D  $(y_{t1}, y_{t2})$  analysis.

five fitting components used in Ref. [13] also completely describes the features in the correlation data.

$$\left[ \frac{\Delta\rho}{\rho_{ref}} \right]_j \approx \sum_{k=1}^5 g_{k,j} \quad (6.11)$$

In the present analysis a column  $j$  will be formed from the sum of seven square bins along a column or row. Equation 6.11 can be re-written with the notation “ $i:j$ ” which indicates a sum over the seven bins  $i$  in column  $j$ .

$$\sum_{k=1}^5 g_{k,j} = \frac{N_{ref,j}}{N_{sib,j}} \frac{\sum_{i:j} n_{sib,i}}{\sum_{i:j} n_{ref,i}} - 1 \quad (6.12)$$

Next, the equation above is expanded to include the normalized ratio

relevant to the present 28 bins analysis is  $\hat{r}_i = \frac{N_{ref,i} n_{sib,i}}{N_{sib,i} n_{ref,i}}$ .

$$\sum_{k=1}^5 g_{k,j} = \frac{N_{ref,j}}{N_{sib,j}} \frac{\sum_{i:j} n_{ref,i} \frac{N_{sib,i}}{N_{ref,i}} \hat{r}_i}{\sum_{i:j} n_{ref,i}} - 1 \quad (6.13)$$

The relationship between  $\hat{r}_i$  and  $\Delta\rho_i/\rho_{ref}$  in the 28 cut bin analysis is given in Eq. 6.5 and results in the following expression,

$$\hat{r}_i = \frac{N_{sib}}{N_{ref}} \frac{N_{ref,i}}{N_{sib,i}} \left[ \frac{n_{ref}}{n_{ref,i}} \frac{\Delta\rho_i}{\rho_{ref}} + 1 \right]. \quad (6.14)$$

Equation 6.7 is used again to relate  $\Delta\rho_i/\rho_{ref}$  to  $\frac{1}{\sqrt{\rho'_{ref}}} \sum_{k=1}^6 f_{k,i}$ .

$$\hat{r}_i = \frac{N_{sib}}{N_{ref}} \frac{N_{ref,i}}{N_{sib,i}} \left[ \frac{n_{ref}}{n_{ref,i}} \frac{1}{\sqrt{\rho'_{ref}}} \sum_{k=1}^6 f_{k,i} + 1 \right] \quad (6.15)$$

This value for  $\hat{r}_i$  is inserted into Eq. 6.13 and, after making the approximations that  $\frac{N_{sib}}{N_{ref}} \approx \frac{n_{sib,j}}{n_{ref,j}}$ , the following relation between the fitting model components in Ref. [13] and the present analysis is made.

$$g_{k,j} \approx \frac{1}{\sqrt{\rho'_{ref}}} \frac{n_{ref}}{n_{ref,j}} \sum_{i:j} f_{k,i} \approx \frac{1}{\sqrt{\rho'_{ref}}} \frac{N_{ref}}{N_{ref,j}} \sum_{i:j} f_{k,i} \quad (6.16)$$

The last step in the equation above neglects the  $y_t$  variation of the reference pair density in angular space.

The upper panels in Fig. 6.15 contain the results reported in Ref. [13] while the lower panels contain similar measurements based on the present analysis. The left panels show the 2D Gaussian amplitude as a function of

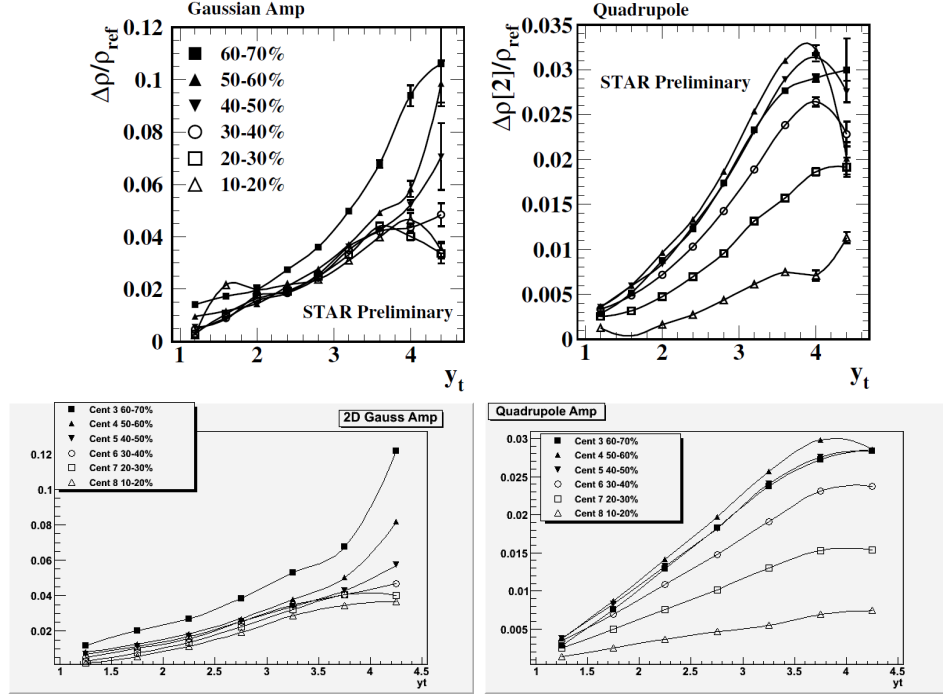


Figure 6.15: The amplitude of the same-side Gaussian (right) and quadrupole (left) from Ref. [13] (upper) and the present analysis (lower) in six centralities of Au+Au 200 GeV data. The points in the upper (lower) panels represent the mean  $y_t$  in each of the 9 (7)  $y_t$  bins. Error bars in the upper panels are fit errors only.

centrality and mean  $p_t$ . The amplitudes and overall trend agree between the two analyses. The same is true for the quadrupole amplitude in the right panels. The agreement between these two independent analyses supports the validity of the results in the present analysis.

### 6.5.2 Future Work

The analysis of the  $(y_{t1}, y_{t2})$  dependence of 2D angular correlations can be improved in the future with finer momentum binning, particle identification information, and other beam energies and species. However, these preliminary results are a rich source of information that completes the experimental determination of the six-dimensional two-particle correlation space.

## Chapter 7

### Conclusion

Since the 1960s, when structure was discovered inside a proton, the study of the strong interaction between quarks and gluons has been an active area of research. It is hoped that through current nuclear experiments physicists will test predictions of the Standard Model in dense, energetic nuclear collisions systems, specifically those involving the strong interaction which is described by Quantum Chromodynamics (QCD). It is also hoped that these experiments will test the hypothesis that a quark gluon plasma can be created in a laboratory setting.

The length scales in which quarks and gluons interact are generally restricted to the size of a hadron due to confinement. However, after the discovery of asymptotic freedom in the 1970s scientists hypothesized that in extremely dense nuclear environments quarks and gluons would become deconfined into a soup called the quark gluon plasma. The Relativistic Heavy Ion Collider (RHIC) has collided two beams of heavy ions at relativistic speeds in an effort to create this unique phase of matter since 2000.

Since direct observation of this short-lived phase is impossible, many analysis techniques attempt to study the early interactions via the final state

particles. What has emerged from analyses of the data from STAR and the other RHIC experiments are two, contradictory paradigms for understanding the results. On the one hand the colliding particles (quarks and gluons within the colliding nuclei) are thought to strongly interact and quickly reach thermal equilibrium, leading to hydrodynamic behavior which is described with an equation of state. The resulting hydrodynamic pressure produces collective, flowing matter. The strong interactions among the partons also imply suppression of hard scattering phenomenon such as jets.

The other view is that primary parton-parton scattering leads directly to jet fragmentation with little effect from parton re-scattering following the initial nucleus-nucleus impact. Superposition of independent nucleon-nucleon collisions provides a good starting point for describing the nucleus-nucleus collisions. Significant deviations from superposition occur but these are viewed as being due to strong modifications of the fragmentation processes.

The challenge is to distinguish and perhaps falsify one or both of these models of relativistic heavy ion collisions via analysis methods. Complicated analysis methods are often required to extract information from millions of events that can consist of over 1000 particles. Therefore it is very important to identify the assumptions of each analysis method before forming definitive conclusions.

In my research I used a two-particle correlation measure of Au+Au collisions at  $\sqrt{s_{NN}}=200$  GeV at STAR. This analysis was able to enhance small signals in the data with few to no assumptions about the underlying



physics mechanisms. Correlations can be constructed from several projections of the available six-dimensional space  $(\eta_1, \phi_1, p_{t1}, \eta_2, \phi_2, p_{t2})$ .

Two-particle correlations in momentum  $(p_{t1}, p_{t2})$  space display a rich structure and evolution with centrality. The main feature in charge independent correlations is a broad peak extending from  $p_t = 0.5 - 4.0$  GeV/ $c$  that evolves smoothly with centrality. Results from particle pairs distinguished by charge and relative azimuthal angles were also presented. Surprisingly, the peak for away-side or “back-to-back” pairs did not dissipate or soften with centrality. The same-side unlike-sign pairs exhibited an unusual double peak feature that might be related to a change in the momentum distribution of pions versus protons.

The parametrization of the correlation structures was done via fitting functions. The leading model is based on a fluctuating soft component and a 2D Gaussian located at intermediate  $p_t$ . The parameters for the peak evolve smoothly with centrality, contrary to the structures associated with jets in angular space. The overall findings are that the amplitude of the peak structure evolves smoothly with an increase in centrality and the location remains approximately at the same  $p_t$ .

These results were also compared to theoretical models. The event generator, HIJING, often used to model peripheral heavy ion interactions, predicts a similar peak in intermediate  $p_t$  but only when jets are included. AMPT, which models some characteristics of central Au+Au data successfully does not follow the general trends in  $(p_{t1}, p_{t2})$  correlations. When sufficient

parton-parton interaction strength is included in AMPT to reproduce  $v_2$  the  $(p_{t1}, p_{t2})$  peak for partons is strongly dissipated.

This dissertation also answers the question, how are pairs correlated in specific angular features distributed in momentum? The results show that pairs correlated in the same-side peak and the dipole (dijet away-side) are distributed around  $(y_{t1}, y_{t2}) = (3, 3)$  and the distribution does not soften with an increase in centrality. Furthermore, the momentum distribution of pairs in different  $\eta_\Delta$  regions of the same-side peak were presented. The study found the extended correlation on  $\eta_\Delta$ , commonly referred to as the “ridge”, was not comprised of softer pairs relative to the center of the same-side peak. This challenges the notion that the same-side angular structure can be classified into a “ridge” and “jet” region with different physical mechanisms.

This dissertation presented new correlation measurements of 200 GeV Au+Au collisions in important aspects of the six dimensional correlation space. These measurements can be used to distinguish competing hypotheses. The observation of back-to-back jet fragments in the  $p_t$  range 0.5-4.0 GeV/ $c$  with no suppression does not appear to support the hypothesis of a strongly interacting QGP.

The scope of this analysis can be broadened in the future to include identified particle correlations, now possible with the new Time-Of-Flight detector subsystem installed in 2010. Comparing correlations in momentum and angular space of pions, kaons, and protons could lead to a better understanding of the underlying physics mechanisms such as jets with medium modification

or collective flows. Furthermore, momentum correlations from collisions with varying beam energies and species, which have already been collected, could help piece together a comprehensive model of the heavy ion collision dynamics.

## Bibliography

- [1] X. Dong, arXiv:1210.6677 [nucl-ex], (2012).
- [2] K. H. Ackermann *et al.*, Nucl. Instrum. Meth. A **499**, 624 (2003).
- [3] M. Daugherty, Ph.D. Thesis, University of Texas at Austin (2008).
- [4] D. J. Prindle, <http://www.star.bnl.gov/protected/estruct/prindle/pileup/index.html> (2012), [Online; accessed 25-July-2012].
- [5] D. J. Prindle and T. A. Trainor, J. Phys.: Conf. Ser. **27**, 118 (2005).
- [6] T. A. Trainor and D. J. Prindle, J. Phys.: Conf. Ser. **27**, 134 (2005).
- [7] T. A. Trainor, Int. J. Mod. Phys. E **17**, 1499 (2008).
- [8] Brookhaven National Laboratory, <http://www.bnl.gov/newsroom/news.php?a=21870> (2010), [Online; accessed 11-Jan-2013].
- [9] T. A. Trainor, R. J. Porter, and D. J. Prindle, J. Phys. G **31**, 809 (2005).
- [10] R. J. Porter and T. A. Trainor, J. Phys.: Conf. Ser. **27**, 98 (2005).
- [11] G. Agakishiev *et al.*, (STAR Collaboration), Phys. Rev. C **86**, 064902 (2012).

- [12] K. H. Ackermann *et al.*, (STAR Collaboration), Phys. Rev. Lett. **86**, 402 (2001).
- [13] D. Kettler, (STAR Collaboration), J. Phys.: Conf. Ser. **270**, 012058 (2011).
- [14] D. J. Gross and F. Wilczek, Phys. Rev. Lett. **30**, 1343 (1973).
- [15] H. D. Politzer, Phys. Rev. Lett. **30**, 1346 (1973).
- [16] G. Arnison *et al.*, (UA1 Collaboration), Phys. Lett. B **172**, 461 (1986).
- [17] B. I. Abelev *et al.*, (STAR Collaboration), Phys. Rev. Lett. **97**, 252001 (2006).
- [18] J. Adams *et al.*, (STAR Collaboration), Phys. Rev. Lett. **95**, 152301 (2005).
- [19] J. Adams *et al.*, (STAR Collaboration), Nucl. Phys. A **757**, 102 (2005).
- [20] J. Putschke, (STAR Collaboration), J. Phys. G **34**, S679 (2007).
- [21] Brookhaven National Laboratory, [http://www.bnl.gov/bnlweb/about\\_BNL.asp](http://www.bnl.gov/bnlweb/about_BNL.asp) (2012), [Online; accessed 16-July-2012].
- [22] Brookhaven National Laboratory, [http://www.bnl.gov/bnlweb/history/RHIC\\_history.asp](http://www.bnl.gov/bnlweb/history/RHIC_history.asp) (2012), [Online; accessed 16-July-2012].
- [23] M. Harrison, T. Ludlam, and S. Ozaki, Nucl. Instrum. Meth. A **499**, 235 (2003).

- [24] D. B. Steski *et al.*, Rev. Sci. Instrum. **73**, 797 (2002).
- [25] J. G. Alessi *et al.*, Rev. Sci. Instrum. **81**, 02A509 (2010).
- [26] J. Benjamin *et al.*, in *Proceedings of the 1999 Particle Accelerator Conference* 2277 (1999).
- [27] K. Adcox *et al.*, Nuc. Instrum. Meth. A **499**, 469 (2003).
- [28] M. Anderson *et al.*, Nucl. Instrum. Meth. A **499**, 659 (2003).
- [29] F. Bergsma *et al.*, Nucl. Instrum. Meth. A **499**, 633 (2003).
- [30] K. Nakamura *et al.*, J. Phys. G **37**, 075021 (2010).
- [31] M. Beddo *et al.*, Nucl. Instrum. Meth. A **499**, 725 (2003).
- [32] K. Kajimoto, Ph.D. Thesis, University of Texas at Austin (2009).
- [33] C-Y. Wong, *Introduction to High-Energy Heavy-Ion Collisions*, World Scientific (1994).
- [34] F. S. Bieser *et al.*, Nucl. Instrum. Meth. A **499**, 766 (2003).
- [35] D. J. Prindle, <http://www.star.bnl.gov/protected/estruct/prindle/pileupFinder/index.html> (2012), [Online; accessed 25-July-2012].
- [36] T. A. Trainor and D. J. Prindle, hep-ph/0411217 (2007).
- [37] R. L. Ray and M. Daugherty, J. Phys. G **35**, 125106 (2008).
- [38] J. G. Reid and T. A. Trainor, Nucl. Instrum. Meth. A **457**, 378 (2001).

- [39] D. Kharzeev and M. Nardi, Phys. Lett. B **507**, 121 (2001).
- [40] J. Adams *et al.*, (STAR Collaboration), Phys. Rev. D **74**, 032006 (2006).
- [41] J. Adams *et al.*, (STAR Collaboration), Phys. Rev. Lett. **91**, 172302 (2003).
- [42] S. S. Adler *et al.*, (PHENIX Collaboration), Phys. Rev. C **69**, 034910 (2004).
- [43] K. Adcox *et al.*, (PHENIX Collaboration), Phys. Rev. Lett. **88**, 242301 (2002).
- [44] B. I. Abelev *et al.*, (STAR Collaboration), Phys. Rev. C **79**, 034909 (2009).
- [45] S. S. Adler *et al.*, (PHENIX Collaboration), Phys. Rev. C **69**, 034909 (2004).
- [46] J. Adams *et al.*, (STAR Collaboration), Phys. Rev. C **71**, 064906 (2005).
- [47] S. M. Stigler, Statist. Sci. **4**(2), 73 (1989).
- [48] J. L. Rodgers and W. A. Nicewander, Am. Stat. **42**(1), 59 (1988).
- [49] T. Sjostrand, S. Mrenna, and P. Skands, J. High Energ. Phys. **0605**, 26 (2006).
- [50] B. Andersson *et al.*, Phys Rep **97**, 31 (1983).

- [51] R. Hanbury Brown and R. Q. Twiss, *Nature* **178**, 1046 (1956).
- [52] M. E. Peskin and D. V. Schroeder, *An Introduction to Quantum Field Theory*, Perseus Books (1995).
- [53] X-N. Wang and M. Gyulassy, *Phys. Rev. D* **44**, 3501 (1991).
- [54] D. W. Duke and J. F. Owens, *Phys. Rev. D* **30**, 49 (1984).
- [55] I. Sarcevic, S. D. Ellis, and P. Carruthers, *Phys. Rev. D* **40**, 1446 (1989).
- [56] B. Schenke, S. Jeon, and C. Gale, *Phys. Rev. C* **85**, 024901 (2012).
- [57] J. Adams *et al.*, (STAR Collaboration), *J. Phys. G* **34**, 799 (2007).
- [58] J. Adams *et al.*, (STAR Collaboration), *Phys. Lett. B* **634**, 347 (2006).
- [59] Z-W. Lin *et al.*, *Phys. Rev. C* **72**, 064901 (2005).
- [60] Y. Hama, T. Kodama, and O. Socolowski Jr., *Braz. J. Phys.* **35** (2005).
- [61] C. E. Aguiar, T. Kodama, T. Osada, and Y. Hama, *J. Phys. G* **27**, 75 (2001).
- [62] J. Takahashi *et al.*, *Phys. Rev. Lett.* **103**, 242301 (2009).
- [63] M. Sharma *et al.*, *Phys. Rev. C* **84**, 054915 (2011).
- [64] M. Calderon de la Barca Sanchez, Ph.D. Thesis, Yale University (2001).
- [65] A. Adare *et al.*, (PHENIX Collaboration), *Phys. Rev. Lett.* **101**, 232301 (2008).



- [66] CERN, <http://wwwasd.web.cern.ch/wwwasd/geant/> (2003), [Online; accessed 4-Feb-2013].
- [67] R. Bellwied *et al.*, Nucl. Instrum. Meth. A **499**, 640 (2003).
- [68] R. J. Fries, B. Muller, C. Nonaka, and S. A. Bass, Phys. Rev. C **68**, 044902 (2003).
- [69] R. C. Hwa and C. B. Yang, Phys. Rev. C **70**, 024905 (2004).
- [70] F. James, CERN Program Library Long Writeup D **506** (1994).
- [71] J. A. Nelder and R. Mead, Comput. J. **7**, 308 (1965).
- [72] A. Adare *et al.*, (PHENIX Collaboration), Phys. Rev. Lett. **107**, 252301 (2011).
- [73] S. S. Adler *et al.*, (PHENIX Collaboration), Phys. Rev. Lett. **97**, 052301 (2006).
- [74] B. I. Abelev *et al.*, (STAR Collaboration), Phys. Rev. C **80**, 064912 (2009).

## Vita

Elizabeth Wingfield Oldag was born in Manhattan, Kansas, the daughter of William Wingfield and Kristin Cunningham. She graduated from Sarasota High School in Sarasota, Florida in 2003. She then attended Florida State University in Tallahassee, Florida where she graduated with a Bachelor of Science in physics in 2007. In the fall of 2007 she entered the physics graduate program at the University of Texas at Austin and advanced to doctoral candidacy in August of 2009.

Permanent address: Department of Physics, The University of Texas  
at Austin, Austin, TX 78712, USA

This dissertation was typeset with L<sup>A</sup>T<sub>E</sub>X<sup>†</sup> by the author.

---

<sup>†</sup>L<sup>A</sup>T<sub>E</sub>X is a document preparation system developed by Leslie Lamport as a special version of Donald Knuth's T<sub>E</sub>X Program.